12-2022

Understanding Structure-Property Relationships in Deep Eutectic Solvents

Stephanie Spittle
University of Tennessee, Knoxville, sspittle@vols.utk.edu

Recommended Citation

Spittle, Stephanie, "Understanding Structure-Property Relationships in Deep Eutectic Solvents. " PhD diss., University of Tennessee, 2022.
https://trace.tennessee.edu/utk_graddiss/7584

To the Graduate Council:

I am submitting herewith a dissertation written by Stephanie Spittle entitled "Understanding Structure-Property Relationships in Deep Eutectic Solvents." I have examined the final electronic copy of this dissertation for form and content and recommend that it be accepted in partial fulfillment of the requirements for the degree of Doctor of Philosophy, with a major in Chemical Engineering.

Joshua R. Sangoro, Arthur J. Ragauskas, Major Professor

We have read this dissertation and recommend its acceptance:

Tessa R. Calhoun, Mark D. Dadmun

Accepted for the Council:

Dixie L. Thompson

Vice Provost and Dean of the Graduate School

(Original signatures are on file with official student records.)

To the Graduate Council:
I am submitting herewith a dissertation written by Stephanie Spittle entitled "Understanding Structure-Property Relationships in Deep Eutectic Solvents." I have examined the final electronic copy of this dissertation for form and content and recommend that it be accepted in partial fulfillment of the requirements for the degree of Doctor of Philosophy, with a major in Chemical Engineering.

Arthur Ragauskas, Major Professor

We have read this dissertation
and recommend its acceptance:

Joshua Sangoro

Tessa Calhoun

Mark Dadmun

Accepted for the Council:

Dixie L. Thompson

Vice Provost and Dean of the Graduate School

(Original signatures are on file with official student records.)

Understanding Structure-Property Relationships in Deep Eutectic Solvents

A Dissertation Presented for the
Doctor of Philosophy
Degree
The University of Tennessee, Knoxville

Stephanie Spittle
December 2022

Dedicated to my two dogs, Baker and Augie for providing unconditional love and support throughout my PhD pursuit.

In memory of my dear friend Miranda Eckard, who taught me to cherish everyday and inspired me to follow my heart.

I had a marvelous time ruining everything.
—Taylor Swift, The Last Great American Dynasty

Acknowledgements

First, I would like to thank my family and friends for sticking by me, even when it was not pleasant or easy. I give my utmost gratitude to my advisor, Dr. Joshua Sangoro, whose guidance meant so much to me. I owe many thanks to Dr. Art Ragauskus and Dr. Tessa Calhoun for stepping up to mentor me in the ninth hour, when I really needed support. I would also like to thank Dr. Mark Dadmun and Dr. Thomas Zawodzinski (honorable mention) for being willing to serve on my committee and collaborating with me on many projects. I owe so much to Dr. Tyler Cosby, who mentored me when I first joined the Sangoro lab, and really never stopped, even after he graduated. Additionally, many of these experiments were performed at Oak Ridge National Laboratory under the supervision of Dr. Yangyang Wang, who was always open to sharing his knowledge. I would like to thank my other fellow group members, both alumni and current, Dr. Thomas Kinsey, Dr. Emmanuel Mapesa, Jonathan Coote, Bryce Hansen, Kaylie Glynn, and Javad Jeddi. I also owe a special thank you to my incredible undergraduate student, Will Brackett.

Abstract

There is a vital need for sustainable solvents that can effectively replace conventional organic solvents which are toxic and hazardous. Deep eutectic solvents (DESs) are a mixture of a hydrogen bond donor (HBD) and hydrogen bond acceptor (HBA) which results in a depressed melting temperature significantly below the parent compounds. They can be made from cheap and renewable resources, and have advantageous properties, such as wide liquidus and electrochemical windows, nonflammibility, and nontoxicity. However, the current state of DESs has some general drawbacks including high viscosity and low ionic conductivity compared to conventional solvents which reduces their appeal for commercial use. However, there are an estimated 10^{19} possible DESs that have yet to be explored. In order to rationally investigate these options, a fundamental understanding of structure-property relationships should be established. Therefore, this dissertation seeks to understand how composition, local structure and dynamics, and interactions affect the macroscopic properties observed. Here, we study two DESs in unprecedented detail: Ethaline, a 33mol% choline chloride (ChCl) in ethylene glycol, and Glyceline, 33mol% ChCl to glycerol. We observed that for both DESs, ChCl weakens but does not fully disrupt the hydrogen bonded network of the neat HBD. This led to an increase in the rate of dynamics and therefore decrease in melting/glass temperature. The trends in other properties were somewhat different between the two DESs. In Glyceline, the fluidity, ionic conductivity, and dynamics were all enhanced at the eutectic point. In Ethaline, we found that the actual eutectic composition is in the 15-20mol% ChCl in ethylene glycol range. Additionally, the dynamics and ionic conductivity are enhanced in this range, but not the fluidity (previously reported).

Table of Contents

List of Tables

List of Figures

Chapter 1

Introduction

1.1 Motivation

Liquids are ubiquitous, and needed in numerous areas of life. Many chemical processes, emerging technologies, and products in everyday life rely on liquids for operation. Employing liquids as solvents is perhaps one of their most prevalent uses. For example, solvents are used in paints, inks, and personal care products to dissolve or disperse a solute of interest, create a desired consistency, and can also evaporate quickly so the solute is applied and can dry in an efficient manner specific to its use. However, many of the solvents used currently present a threat to human and environmental health.[12] Therefore, a significant push toward alternative solvents has been made to lighten the burden of these effects.

Classes of alternative solvents include but are not limited to renewable solvents (bio-derived), ionic liquids, supercritical fluids, liquids polymers, and deep eutectic solvents.[12] However, feasibility of these is contingent on their ability to be scaled up safely and cost effectively with performance similar to conventional solvents, which is not currently achievable for these mentioned materials. While many factors play a role in these materials not being commercially viable yet, one important issue is the lack of insight into these materials. A comprehensive understanding of these materials at a molecular level would allow them to be rationally manipulated and improved. If these materials could have their properties enhanced and be manufactured cheaper, they would be better prospects for industrial solvents.

One of the emerging classes of alternative solvents, deep eutectic solvents, are of specific interest as they are usually made from readily available, cheap components (that could be produced from renewable resources). They are considered to be highly tunable as their synthesis is merely mixing two or more compounds together until a uniform liquid is obtained. However, they have some outstanding issues that also prevent them from being viable large-scale. For example, typically, their viscosities are higher and ionic conductivities are lower than other solvents used industrially. As these are "designer solvents", these issues could be addressed if their chemistry was engineered using knowledge of structure-property relationships. To elucidate these relationships is to have predictive knowledge in tailoring DES for specific applications, which would be incredibly useful in advancing this class of alternative solvents.

This dissertation seeks to answer the following questions relating to this knowledge gap:

1. Is the eutectic composition the optimal point for most advantageous physicochemical properties?
2. Should the eutectic point be considered a single molar composition or a range of compositions?
3. How do the local structures and microscopic dynamics evolve with variation of composition of the mixtures approaching the eutectic concentration
4. How do spatial and temporal heterogeneities influence the macroscopic properties?

The research presented in this dissertation was carried out with a goal of unraveling fundamental, yet crucial, information about a class of non-aqueous solvents that could replace conventional organic solvents. DESs are studied in unprecedented detail to probe the relationship between composition, local structure and dynamics to the macroscopic properties observed. We demonstrate how the physicochemical properties are directly related to temporal and spatial heterogeneities which evolve with varying composition.

1.2 Outline

This dissertation consists of 6 total chapters. Chapter 2 is a scientific literature review of history, theory, and current progress in relevant liquids. Chapter 3 gives an overview of the experimental methods as well as theory and analytical techniques used to study and understand the proposed materials. Chapters 4 and 5 provide the results found concerning fundamental relationships in deep eutectic solvents. Finally, 6 summarizes the results and answers the questions asked in the above section with insight and context into how they fit into broader fields.

Chapter 2 first overviews what liquids and glasses are in Section 2.1, as well as the glass transition phenomena and available theories to understand it. Then, the application of liquids as solvents is discussed in Section 2.2 as well as the issues they present as toxic compounds. The need for “alternative solvents” is explained, where ionic liquids are introduced in Section 2.3. While ionic liquids have advanced the field of green chemistry, they present their own issues. Therefore, the incentive to study deep eutectic solvents as green solvents is clear. The history, properties, and state of literature regarding DESs is discussed in Section 2.4, ending with the current knowledge gap therefore motivating work for this dissertation.

Chapter 3 goes over the experimental techniques chosen to study DESs in this dissertation. The methods chosen were differential scanning calorimetry (Section 3.1), dynamical mechanical spectroscopy (Section 3.2), and broadband dielectric spectroscopy (Section 3.3). The theory and history behind these methods are discussed, as well as the methods of analyzing data obtained from these techniques. There is an emphasis specifically on how these methods are useful in shedding light into deep eutectic solvents.

Chapter 4 discusses the impact of composition on the properties in a prototypical DES. Results show that the actual eutectic composition of this mixture is different from what has been historically reported. We show that by operating at the newfound composition, the orientational and solvent dynamics as well as ionic conductivities are enhanced.

Chapter 5 uses a conglomerate of work among expert collaborators to create a full picture of how local structure and dynamics effect the macroscopic properties of two DESs. It is demonstrated that as salt is added to the hydrogen bond donor, the ions form hydrogen bonds with the donor, which decreases but does not fully disrupt the hydrogen bonded network of the system. This leads to the melting and glass transition temperature depression as well as enhanced physicochemical properties.

Lastly, Chapter 6 summarizes the results found in the previous two chapters and provides answers for the scientific questions asked. The broader implications of this work is discussed as well as the outlook and future work that should be considered.

Chapter 2

Literature Review

In this chapter, an overview of liquids and solvents will be given to provide context and motivation for the work completed in this dissertation contributing to the bigger picture being painted. First, liquids are generally defined. The glass transition will be explained and theory behind it will be discussed as well as the gap in knowledge that is still present. Second, conventional organic solvents and their outstanding issues will be discussed, providing the motivation for alternative, green solvents. Ionic liquids will be defined and discussed, touching on their appeal and efforts made to optimize them. Finally, deep eutectic solvents will be considered. The history and development of these materials is gone over. The properties which make them so significant are also discussed. Then, the work done to understand the phase behavior, structure, and dynamics of deep eutectic solvents is summarized.

2.1 Liquids

Liquids are present and essential in numerous applications. Therefore, the need to understand them on a fundamental and molecular level is extremely important so they can be improved, advanced, and developed in various scientific applications. Liquid is one of the three states of matter, between gas and solid. Changes between these states of matter are considered first-order phase transitions. Liquids and gases are both classified as a fluid state of matter, with the ability to conform or deform as a result of external forces. However, in contrast to gases, liquids are nearly incompressible, and while they will conform to the shape of a container or vessel, they will not expand to fill it like gases. At a fixed pressure, lowering the temperature of most liquids at a slow enough rate will allow the the molecules to rearrange into a crystal lattice structure, turning into a solid state of matter. However, crystallization can be suppressed if the material is cooled quick enough, where the liquid would then transition into a glassy state (amorphous).

Many materials studied in this dissertation are either naturally glass-forming or can be easily supercooled into a glass. A glass transition is considered a kinetic phenomenon, or second-order phase transition, where a liquid changes to a solid-like state on cooling.[13] This occurs at the calorimetric glass transition temperature, $\mathrm{T_g}$. As opposed to true crystallization, there is no structural change between a liquid and its glassy state.[14] Concerning experimentation, this allows liquid-like phenomena to be studied in experimentally attainable frequency ranges by cooling the material and slowing down the rates of dynamics. Detectable features of the glass transition include but are not limited to abrupt changes in heat capacity, thermal expansion, viscosity, and characteristic relaxation times.[15, 10] These changes can be observed using a wide variety of experimental methods such as light scattering, neutron scattering, differential scanning calorimetry, dynamic mechanical spectroscopy, NMR spectroscopy, and broadband dielectric spectroscopy.[10, 16] Despite available techniques and many efforts to study the glass transition, a physical understanding of the glassy state is still up for controversy and no theory is accepted by a majority.

The Vogel-Fulcher-Tamman (VFT) equation can be used to describe the temperature-dependent behavior of many quantities, such as viscosity (η) or conductivity (σ) in liquids, and especially in the supercooled or glassy state. For viscosity, the VFT function can be written as:

$$\eta(T) = \eta_\infty \exp\left(\frac{B}{T - T_0}\right) \tag{2.1}$$

where η_∞ is the viscosity at infinite temperature, B is a fitting parameter, and T_0 is the ideal glass transition temperature (obtained by an infinitely slow cooling rate, typically 50°C below $\mathrm{T_g}$).[17, 18, 19, 20, 21] As opposed to the Arrhenius equation which describes a system with a single activation energy over the temperature range, the VFT function describes a system where the activation energy changes at each temperature. Glass-forming liquids can be classified by how far they deviate from the Arrhenius model. Again, the theoretical meaning of this is not well-understood.

Even still, there are many useful relations that exist for liquids relating basic physicochemical properties to the glass transition. The dynamic glass transition, also known as the structural or α-relaxation, is a reflection of rotational diffusion or orientational dynamics in a material.[22] The temperature-dependence of the characteristic relaxation time of this phenomena can also be described by the VFT equation. The $\mathrm{T_g}$ can be estimated at the temperature for which the structural relaxation time $\tau_\alpha = 10^2 s$ (or the rate, $\omega_\alpha = 1/\tau_\alpha = 10^{-2} s$). This is the timescale where molecular motion is essentially frozen. The melting temperature, $\mathrm{T_m}$, can be estimated by Lindemann's criterion, $\mathrm{T_m}$=2/3$\mathrm{T_g}$.[23] This is a really useful estimation if held true, especially when liquids are almost exclusively glass-forming, such as glycerol.[24]

Additionally, the shear viscosity, η_0, can be estimated by τ_α (or vice versa) through Maxwell's identity: $\eta_0 \approx G_\infty \tau_\alpha$, where G_∞ is the high frequency shear modulus.[25, 26, 27] Rewriting this to relate fluidity, η^{-1}, to the structural relaxation rate gives us: $\eta^{-1} \approx G_\infty \omega_\alpha$. Classical electromagnetism or fundamental electrodynamics allow us to define ionic conductivity for monovalent ionic compounds as:

$$\sigma_0 = nq\mu \tag{2.2}$$

where n is the number density of charge carriers, q is the charge, and μ is the mobility. The Einstein-Smoluchowski equation for charged particles and Stokes-Einstein equation for diffusion of spherical particles can be written as $D = \mu k_B T/q$ and $D = k_B T/(6\pi\eta r)$ respectively, where D is the diffusion coefficient, k is the Boltzmann constant, and r is the radius. Additional assumptions to these relations are that the particles are undergoing Brownian motion at a constant temperature and that there is no net flow of particles at equilibrium. Now, ionic conductivity can be defined as:

$$\sigma = \frac{q^2 nr}{6\pi\eta} \tag{2.3}$$

showing that viscosity and ionic conductivity are inversely proportional to one another.[28, 29] Considering all of the relations in this section, we can conclude that ionic conductivity, fluidity, and the structural relation rate should all be directly proportional to each other. However, these relations do not always hold true,[30, 31, 32] which provides a problem in developing a universal, fundamental understanding of liquids.

2.2 Conventional Solvents

Solvents, essential in many areas of science, can be defined as a substance (usually a liquid) used to dissolve, dilute, or disperse a solute.[33, 34] Solvents are used in reactions, extractions, purifications, syntheses, and various other chemical processes. Water is a good solvent for many polar molecules and is easily accessible and renewable. However, it presents its own issues commercially. For example, redox flow batteries are desirable for storing energy on a large scale due to their ability to adjust power output and energy capacity independently, long cycle lifes, and low operating costs. However, their major drawback is low energy densities. To solve this, the field has opted for non-aqueous solvents to widen the potential window and therefore energy capacity of the battery over aqueous-based batteries.[35] Additionally, water and other water-miscible solvents are poor or unable to solvate many materials of interest such as oils and biomolecules. Therefore, to counter these issues, many industries have turned to non-aqueous, organic solvents, which are typically not "clean" or renewable.

It is estimated that the annual production of organic solvents is at roughly 20 million metric tons.[36] It is estimated that more than 40% of new chemical entities in the pharmaceutical industry are insoluble in water,[37] and this industry is considered to be a significant source of chemical waste from production.[12] Moreover, conventional organic solvents are often classified as volatile organic compounds (VOCs), which are defined as chemicals that evaporate easily at room temperature.[38] VOCs are usually hazardous and unsustainable, which presents a clear problem when inevitably entering the environment through evaporation or waste.[39] The emissions of VOCs are considered one of the biggest contributors to air pollution.[38] Therefore, this information combined has initiated a push toward replacing conventional organic solvents with more environmentally friendly solvents.[40]

2.3 Ionic Liquids

Ionic liquids (ILs), simply put, are materials consisting of ions only, free of any other solvent, that exist in the liquid phase at or around room temperature.[41, 42] First discovered by Paul Walden in 1914 was the IL ethylammonium nitrate, with a melting point (T_m) of 12°C.[43] While the known existence of these materials dates back to the early 1900s, they have only become of interest as alternative solvents within the last 40 or so years.[44] Typically, ILs consist of a bulky cation and/or anion (examples of typical molecular structures given in Figure 2.1), which delocalize the charges and lowers the lattice energy of the compound and therefore melting point[45] in comparison to other ionic compounds, such as sodium chloride (T_m=801°C).[46] "Ionic liquids" was a term previously used to also describe molten salts, which overtime, caused a bit of confusion and unclearness in literature.[47] Now, the specific distinction classifying ILs from molten salts is that ILs are liquid at or below 100°C.[48, 49, 47]

The resulting beneficial properties of ILs include low viscosity, low vapor pressure, wide range of thermal stability, high ionic conductivity, the ability to solvate many types of molecules, and are considered highly tunable because of the estimated 10^{18} possible combinations of cations and anions to be explored.[50] For these reasons, many advances have been made in various applications using ILs to replace current conventional solvents.[51] These areas include, but are not limited to, biomass processing,[52, 53, 54]

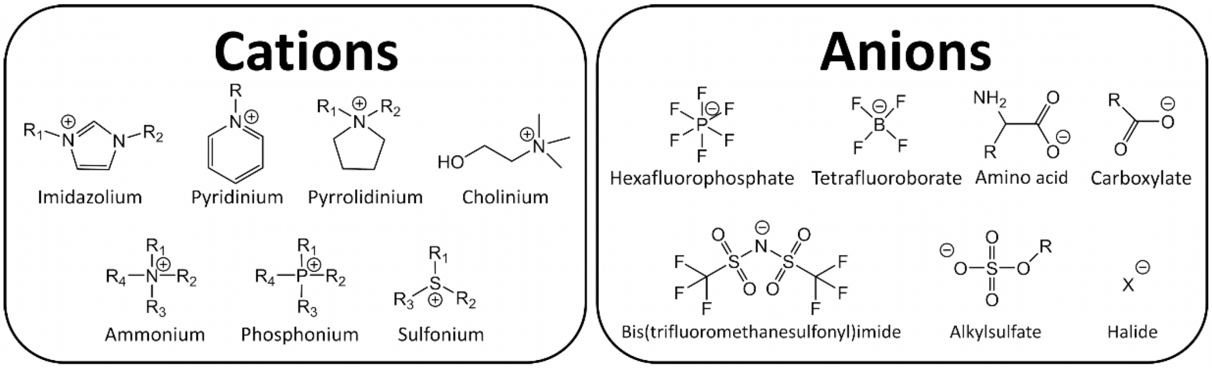

Figure 2.1: Examples of potential or typical-looking cations and anion combinations that would make an ILs. Reprinted with permissionfrom [1].

gas capture,[55, 56, 57] solar cells,[58, 59, 60, 61] catalysis,[62, 63, 64] and separation processes.[65, 66, 67]

However, many ILs are toxic and nonbiodegradable.[68, 69] While their low vapor pressures do reduce risk of air pollution compared to VOCs, their risks of harming the environment in other ways (synthesis from unsustainable precursors, water pollution, etc.) are not negligible.[70] Additionally, ILs are more expensive than conventional organic solvents to produce.[71] However, since they are considered "designer solvents", significant fundamental research concerning structure-property relationships[72, 41, 73] has been done to understand how to tune ILs so these issues can addressed. These efforts have been useful in setting a foundation for machine learning in this area as well.[74, 68] So, while the progress made using ILs to replace conventional organic solvents was impactful, substantial work is needed to bring ILs to commercialization safely and cost-effectively.

2.4 Deep Eutectic Solvents

Deep eutectic solvents (DESs) are another class of "designer solvents", often considered a subclass of ILs due to their similar properties.[75] In a basic sense, DESs are a mixture of a two or more species that at some composition between them, a depressed melting temperature significantly below any of the parent compounds is obtained. The first DESs were discovered by Abbott *et. al.* in 2003, where the name was first coined for these materials.[5] Most notably, they studied a wide range of compositions between urea (T_m=133°C) and choline chloride (ChCl, T_m=302°C), finding that at a 1:2 molar ratio of ChCl to urea the resulting T_m=12°C. Presently, this mixture is commonly known as "Reline". Figure 2.2 shows what various compositions of ChCl and urea look like, including the eutectic composition at 33mol% ChCl where a liquid is observed.

DESs can be classified into four different types. Type I is a mix of a quaternary ammonium salt and a metal chloride. Type II is a mixture of a quaternary ammonium salt and a metal chloride hydrate. Type III is quaternary ammonium salt and a hydrogen bond donor (HBD). Type IV is a mixture of a metal chloride hydrate and a hydrogen bond

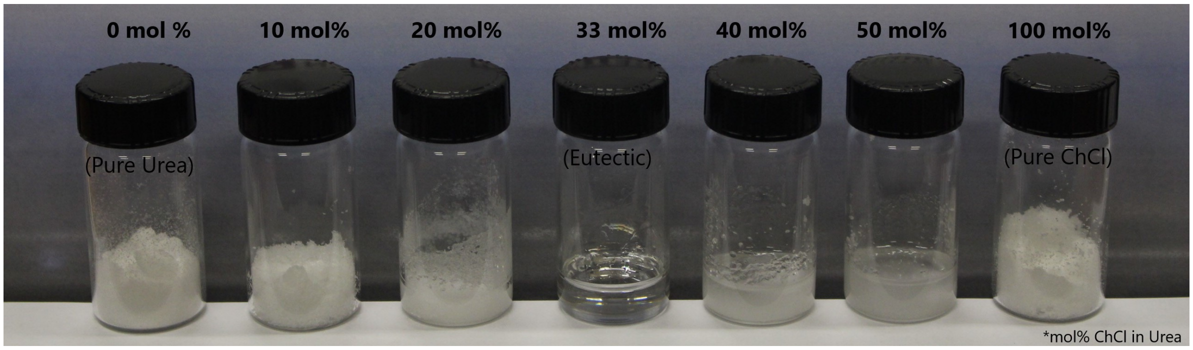

Figure 2.2: Samples of Reline from pure urea to pure ChCl. The eutectic composition is at 33mol% ChCl in urea, where a liquid is observed at room temperature. Reprinted with permissionfrom [2].

donor.[76] The salts are considered the hydrogen bond acceptors (HBAs). Lastly, Type V, the newest type, is a mixture of two non-ionic compounds.[77] Type III is currently the most widely studied in literature,[78] which is due to a number of reasons. For example, the materials used to make these are typically very cheap, nontoxic, biodegradable, and can be derived sustainably. Additionally, the materials are readily available and already being produced on a large scale level. Type III DESs also possess advantageous properties such as nonflammability, wide electrochemical stability windows, high thermal stability, and are great at solvating many types of species.[79, 80, 81, 82, 83, 84] For these reasons combined, this dissertation also focuses largely on Type III DESs. Examples of common HBAs (capable of accepting a proton) and HBDs (capable of donating a proton) that could be used to form Type III DESs are given in Figure 2.3.

The trademark feature of DESs is the large melting point depression, which can even reach upwards of $\Delta \mathrm{T_m} \geq 100$°C.[85] Though a stricter definition to distinguish DESs from regular eutectic mixtures has been called for,[86] it is still not fully established. A general phase diagram for eutectic mixtures is given in Figure 2.4. Many definitions in literature classify a DES as a eutectic mixture that deviates from the ideal solid-liquid phase model (solid line) creating a deeper, unexpected melting point depression. The model for ideal solid-liquid equilibria for a binary mixture based on compound i can be described as:

$$ln(\chi_i \gamma_i) = \frac{\Delta_m H}{R}\left(\frac{1}{T_m} - \frac{1}{T}\right) + \frac{\Delta_m C_p}{R}\left(\frac{T_m}{T} - ln\frac{T_m}{T} - 1\right) \tag{2.4}$$

where χ_i and γ_i are the mole fraction and the activity coefficient of compound i respectively, $\Delta_m H$ is the enthalpy, R is the universal gas constant, T_m is the melting temperature, T is the absolute temperature, and $\Delta_m C_p$ is the difference in heat capacity of the solid and liquid phases of compound i.[86] The unexpected large depression and deviation from ideality is typically attributed in literature to the complexation of the anion by the HBD,[87, 88, 89, 90, 21] although the structural formation of DESs has only been lightly explored.

Similar to ILs, DESs are highly tunable, but the synthesis of DESs is much simpler (mixing two or more components together). While this increases their potential ability to

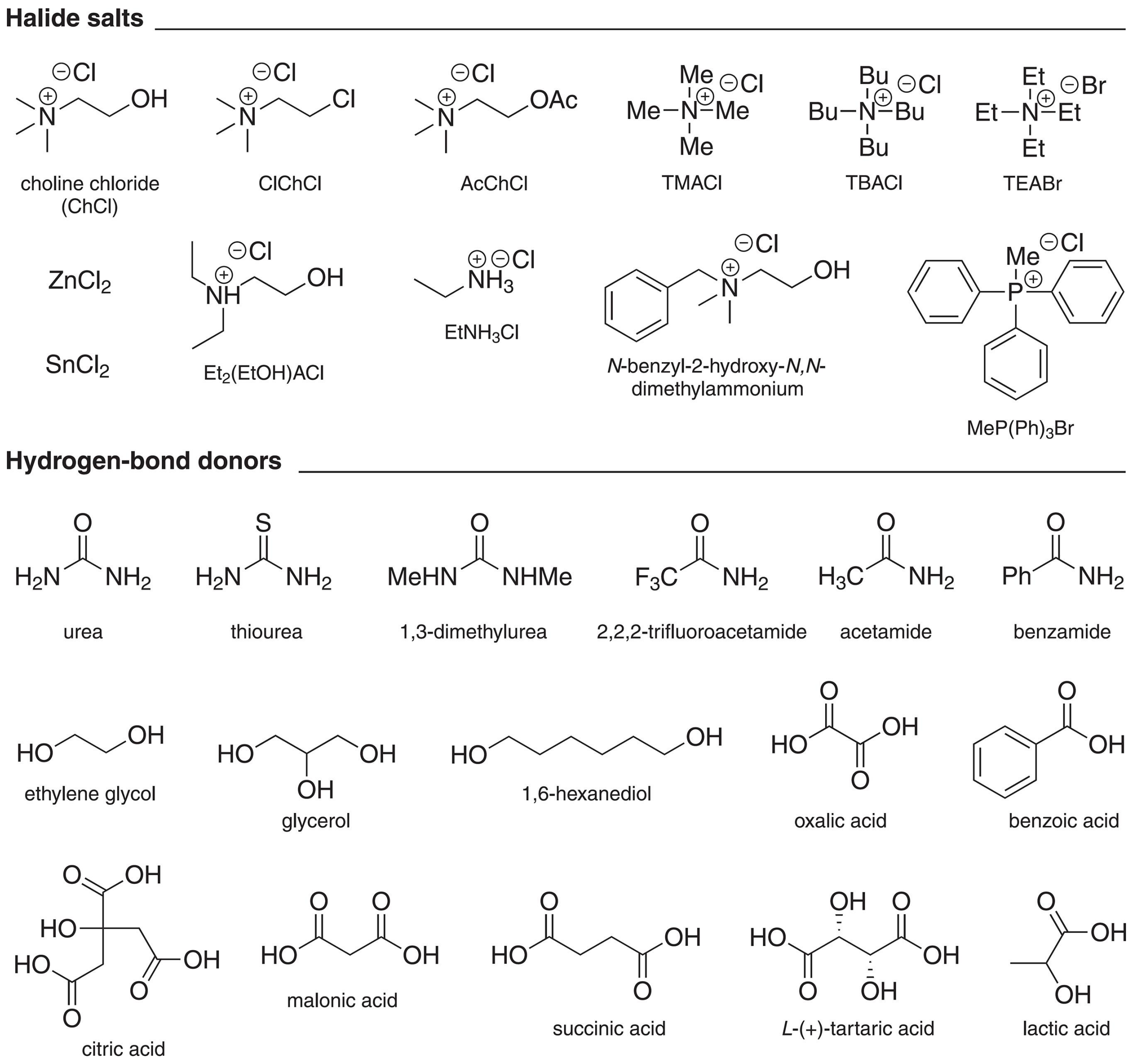

Figure 2.3: Examples of potential halide salts and hydrogen bond donors (HBDs) that could be used to form a Type III DES. Reprinted with permissionfrom [3].

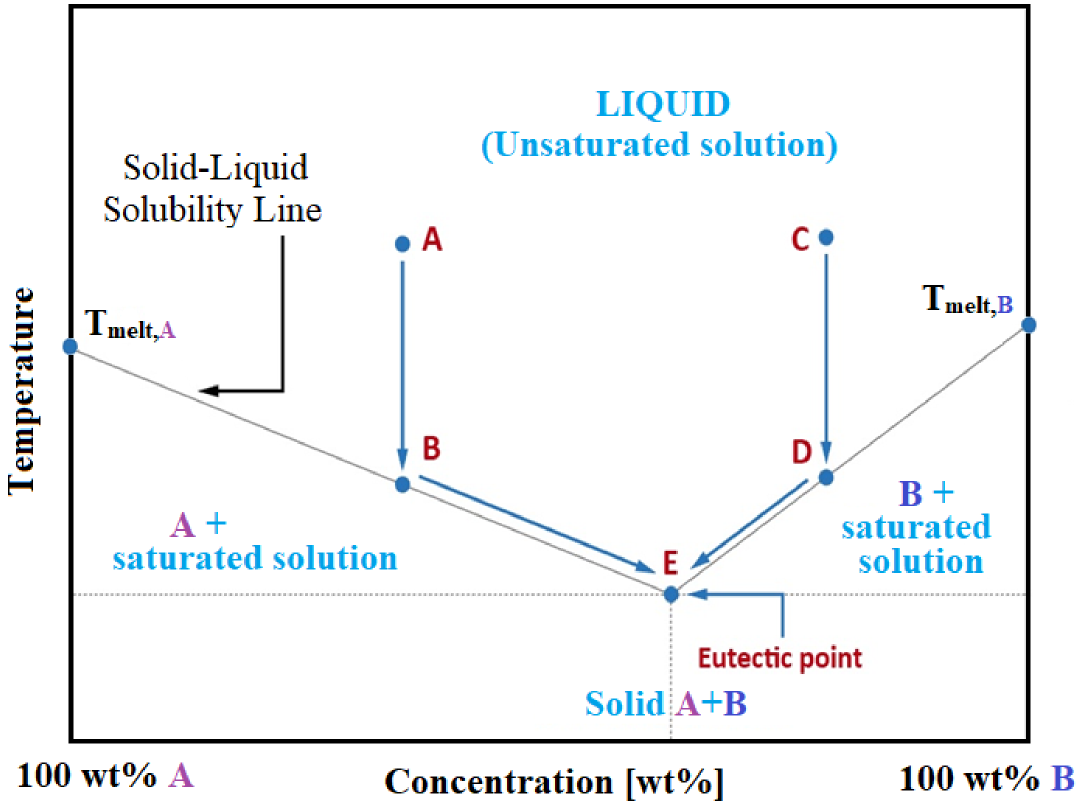

Figure 2.4: Solid-liquid phase diagram for a binary mixture of A and B. To the left of the eutectic point, E, is saturated solution and excess A. To the right of E is a saturated solution and excess B. It would be typical in these areas to see crystals suspended in solution. At temperatures below the eutectic compos is solid A+B. Reprinted with permissionfrom [2].

replace conventional organic solvents, it becomes difficult to fully or rationally investigate that without some fundamental understanding of these materials as there are so many unexplored possibilities. A predictive understanding of the relationship between the chemical structure and the physicochemical properties would be extremely useful. For example, knowing if you mix species A with species B at composition X, you can expect certain properties to be observed. However, most studies up until recently focused on how DESs perform in applications or reporting properties at just one or two compositions. The remaining two subsections in this chapter will focus on (i) properties of DESs already established/reported in literature and (ii) the status of fundamental work regarding DESs that could contribute to understanding structure-property relationships.

2.4.1 Properties of DESs

When selecting a DES for a specific application, it is important to look at the physicochemical properties that would play a factor in their performance. For example, high ionic conductivity would be important in electrochemical technology applications, but maybe less important for some separation applications. Generally, a problem with feasibility of DESs are their high viscosities relative to conventional organic solvents and even ILs, impairing transport properties and increasing pumping costs. Additionally, there are many discrepancies in literature when reporting values for physicochemical properties, which creates confusion and unreliability. In this dissertation, the properties focused on reporting and understanding are phase behavior, viscosity, and ionic conductivity, as they are arguably the most important to identify for most applications.

Phase Behavior

Phase behavior describes the state of matter that a material exists in under certain conditions. Understanding phase behavior in DESs is of great significance considering the melting point depression is the key feature of these materials. It is of clear importance to understand, not only the temperature range for which a DES would be liquid at for a specific composition, but also the composition range for which a DES would be liquid at the application temperature. Therefore, the most useful conditions to study phase behavior of DESs for are temperature and composition. Despite the need for this, very few full phase diagrams of DESs have been reported in literature.[83] It has also been observed that some DESs actually exhibit more than one eutectic composition.[2] However, like stated before, many studies of DESs focus on a single composition and report any properties or results observed at that composition. Furthermore, sometimes the eutectic composition is assumed, potentially from common ratios of other DESs reported in literature, however, this is unproductive because even if the chemical structures of the parent compounds are similar, it does not mean the eutectic composition can be "transferred" to another mixture. In fact, small changes in chemical structure can have high impacts on the resulting physicochemical properties.[4]

Viscosity

Viscosity can be defined as the resistance of flow by a fluid due to internal friction from molecular cohesion.[91, 92, 93] This translates to fluids with lower viscosities flowing easier, and fluids with higher viscosities flowing much slower. Like stated earlier, DESs have relatively high viscosities compared to other conventional solvents. Some DESs, such as a 1:1 molar ratio of ChCl to citric acid, can have viscosities approaching the order of 10^4 cP at room temperature.[2] One DES, Ethaline, historically reported as a 1:2 molar ratio of ChCl to ethylene glycol, has been employed in many application-based studies[94, 95, 96] likely because it has one of the lowest viscosities reported for DESs (48 cP at room temperature).[97] However, the viscosity of Ethaline is still high compared to water at 1 cP or methanol at 0.6 cP (at the same temperature).[98] On a commercial scale, this would increase pumping costs considerably, which lowers their appeal from an industrial aspect unless resolved. While hydrogen bonding is thought to be the key factor in the unexpected melting depression, it also likely plays a role in the high viscosities.

Ionic Conductivity

Ionic conductivity is the ability of a material to carry an electric current via flow of ions.[99] This is an important quantity for electrochemical applications such as redox flow batteries, which have been an area of interest for DESs.[100, 101] DESs generally have low conductivities (<2 mS/cm), which is largely related to their high viscosities,[102] as expected from the relations mentioned in Section 2.1. Other factors could include low ion mobility due to size of ions in the mixture or ion pairing/aggregation that results in a reduced amount of available charge carriers.[103, 99] While all interrelated, these factors should be better understood and studied on a molecular level so that the resulting properties can be improved.

2.4.2 Status of Fundamental Work in DESs

Here, I will discuss the status of fundamental work that has been done on DESs from first, reports of physicochemical properties, second, a structural analysis, and last, a dynamic aspect. For physicochemical properties, I will be focusing mostly on phase behavior. If the phase behavior is not studied in addition to the viscosity and ionic conductivity, the reports of these quantities can be misleading because the eutectic point is not confirmed. To date, very few studies have examined viscosity and conductivity as a function of composition.

Phase Behavior of DESs

Starting with the efforts made to increase the amount of available information concerning the non-ideal solid-liquid phase equilibria in DESs, a study by Zinov'eva *et. al.* reported the phase diagram of ChCl and sulfosalicylic acid (SSA) and determined the eutectic composition was at 70mol% ChCl in SSA.[85] The resulting T_m was -10.5°C, which is much lower than the parent compounds ($T_{m,\ ChCl}$= 302°C and $T_{m,\ SSA}$=120°C). It should also be emphasized that the liquidus range at room temperature spans from 40-80mol% ChCl in SSA. Abranches *et. al.* acknowledged the need for more phase diagrams of DESs and therefore studied a variety of betaine-based DESs.[104] It was shown that betaine with thymol, salicylic acid, menthol, coumarin, and camphor each exhibit negative deviations from the ideal solid-liquid phase equilibria, showing that each mixture exhibits true “deep” eutectic behavior. The magnitude of the deviations was attributed to the hydrogen donating ability of the HBD because betaine is a zwitterion and does not have strong self-interactions.

Silva *et. al.* reported in 2019 the phase diagrams ChCl with a series of urea-based HBDs with slightly different structural variations (urea, thiourea, methylurea, 1,3-dimethylurea, and 1,1 dimethylurea) to see how this affected the phase behavior.[4] These structural changes affected not only the eutectic composition, but also the magnitude of the negative deviations from ideality, shown in Figure 2.5. Some mixtures even experience positive deviations from ideality. These differences can be attributed to interaction centers blocked by replacing protons with methyl groups. As expected from current theories of DES formation, the more blocked interaction centers, the smaller deviation from ideality was. This supports the hypothesis that hydrogen bonding is the main factor in the formation of DESs.

There have also been computational efforts to predict eutectic compositions and melting temperatures. A 2018 study by Silva *et. al.* reported computational and experimental phase diagrams alongside other physicochemical property data for an array of ChCl and sugar mixtures.[1] The sugar+sugar mixtures did not strongly deviate from ideality. While most of the ChCl+sugar mixtures were not liquid at room temperature, the deviation from ideality was significant, and their phase behavior was able to be accurately described using the model they developed. In 2019, Abranches *et. al.* used conductor like screening model for real solvent model (COSMO-RS) to computationally calculate the T_m of ChCl and various pharmaceutical substances (acetylsalicylic acid, ibuprofen, ketoprofen, and paracetamol).[105] First, they used prototypical DESs to develop and validate their model, and then applied it to the new pharmaceutical based systems. Generally, they obtained reasonable results, aside from the ChCl/acetylsalicylic acid DES, which was expected because their model was poor in describing the non-ideal phase equilibria in the other prototypical ChCl/aromatic acids systems they studied to validate their model.

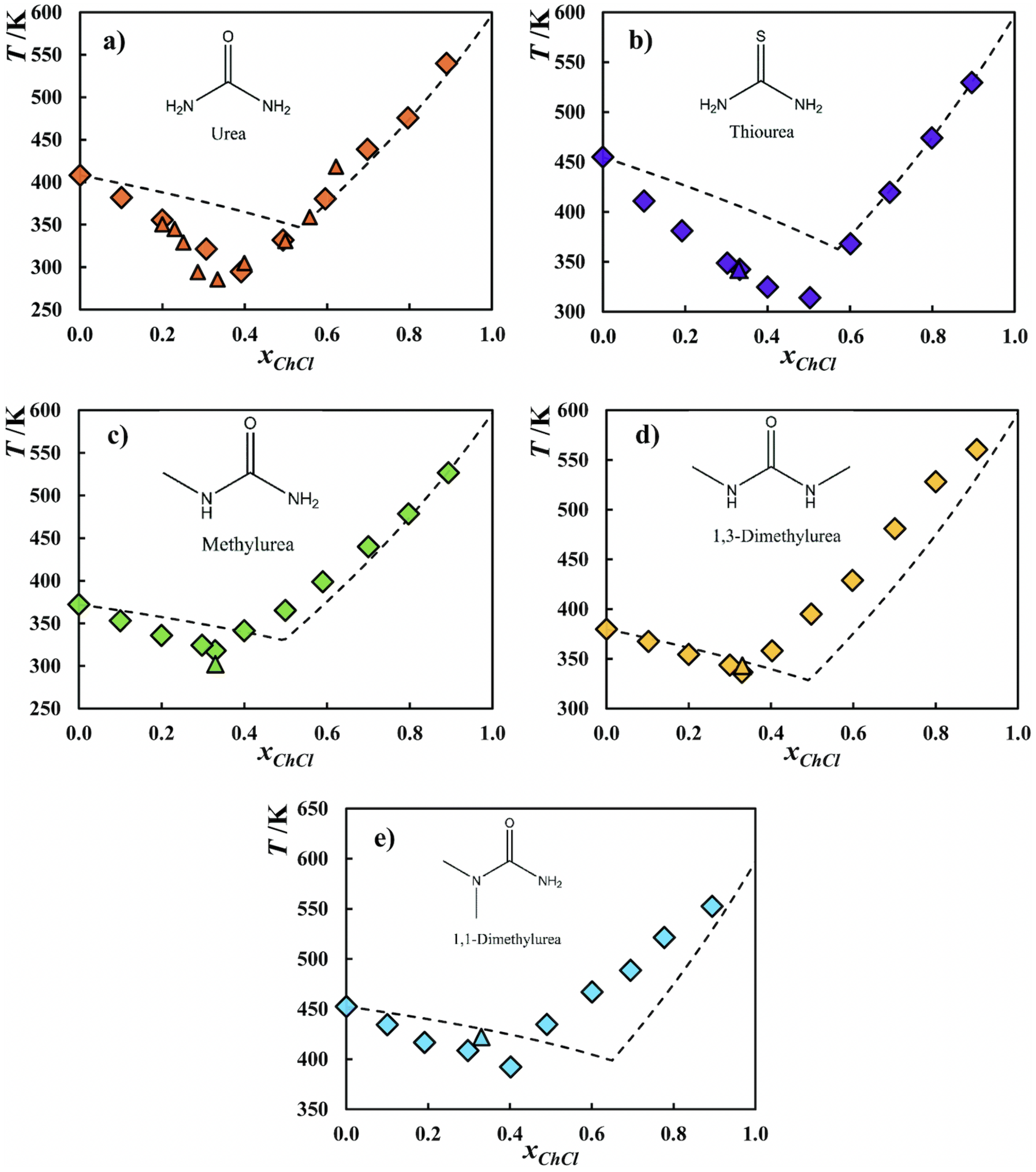

Figure 2.5: Phase diagrams of ChCl with (a) urea, (b) thiourea, (c) methylurea, (d) 1,3-dimethylurea, and (e) 1,1-methylurea. Diamonds are experimental points obtained by [4]. Triangles are experimental points obtained from [5]. The dashed line represents the solid-liquid equilibria for an ideal binary mixture. Reprinted with permission from [4].

Local Structure of DESs

Efforts to understand the liquid structure of DESs has increased rapidly recently,[106, 107, 108] so I will focus on the still semi-recent core work that was done. In 2016, Hammond *et. al.* published the first paper using an experimental technique, neutron diffraction, to examine the structuring and formation of a DES (not including indirect techniques such as nuclear magnetic resonance spectroscopy).[109] Studying Reline, they observed a significant correlation relating to the hydrogen bonding between urea and the chloride anion. This supports the general hypothesis that anion-HBD interactions are the driving force in DES formation. Later that year, Kaur *et. al.* reported nanoscale microheterogeneity in lithium perchlorate and alkylamide mixtures.[110] While these are not technically considered Type III DESs, their work using molecular dynamics (MD) simulations to examine spatial and dynamic heterogeneities previously reported for these DESs[111] was an important establishment in literature. Here, the heterogeneities were due to strong lithium and perchlorate ion interactions.

Stefanovic *et. al.* used quantum mechanical molecular dynamics (QM/MD) to probe the structure of 1:2 molar ratios of ChCl to urea (Reline), ethylene glycol (Ethaline), and glycerol (Glyceline) respectively.[112] While hydrogen bonding was a key factor observed in all systems, the structuring between each DES was fundamentally different. In Reline, urea maintained some self-interactions, but an equal balance of ChCl-urea interactions led to the strong melting point depression. Glyceline and Ethaline exhibited stronger HBD self-interactions, which caused a weaker intercalation of chloride anions and therefore a smaller melting point depression, ΔT_m, compared to Reline. The difference in HBD self-interactions between ethylene glycol (EG) and glycerol were attributed to the differences in acidity of the protons as well as the increased structural flexibility of alcohol HBDs versus urea. Generally, the value of properties including melting point depression and viscosity were determined to be a direct effect of the nature and strength of the HBN of the DESs.

Following this publication, Faraone *et. al.* published a study of Glyceline using neutron spin echo (NSE) experiments to further understand the structure of this DES.[113] They

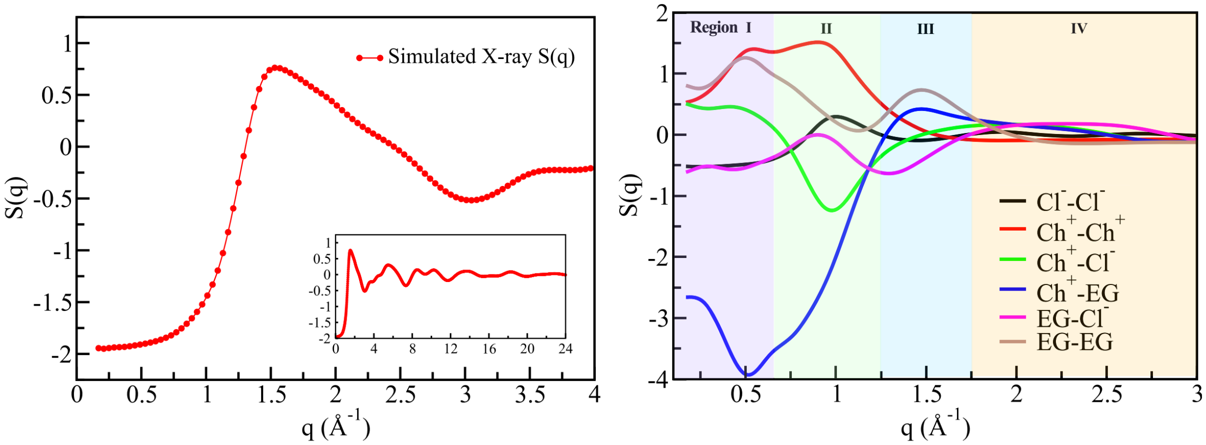

(a)

(b)

Figure 2.6: (a) Simulated x-ray scattering structure function (S(q)) for Ethaline at 303 K. (b) Species-wise deconvolution of total scattering profile. The corresponding q ranges for the regions I-IV are 0-0.67, 0.67-1.25, 1.25-1.75, and 1.75-3.0 Å^{-1}, respectively. Reprinted with permission from [6].

also observed that glycerol exhibits strong self-interactions. Furthermore, they reported that Glyceline is defined by the retained HBN of glycerol and that choline simply occupies the interstitial voids throughout the network. Additionally, Kaur *et. al.* took a deeper look at Ethaline using atomistic MD simulations.[6] The simulated x-ray scattering profile of Ethaline at 303 K is shown in Figure 2.6a. The main peak at 1.5 q arises mainly from EG-EG and choline-EG interactions, with some contribution from choline-chloride interactions, as shown in Figure 2.6b. Generally, they found that ethylene glycol (EG) and the choline cation compete for intermolecular bonding with the chloride anion. They also determined that EG intermolecular self-interactions (Region III of Figure 2.6) are actually not as prominent as EG intramolecular interactions (Region I in Figure 2.6) due to gauche isomers of EG present in the DES.

Dynamics in DESs

Finally, an overview of the transport properties will be summarized. In 2011, D'Agostino published the first article using pulsed field gradient nuclear magnetic resonance spectroscopy (PFG-NMR) to study molecular and ionic diffusion in Ethaline, Glyceline, Reline, and Maline (1:1 molar ratio of ChCl to malonic acid).[7] Self-diffusion coefficients shown in Figure 2.7 show that choline diffuses slower than all of the corresponding HBDs for each DES except for Maline, where choline diffuses faster than malonic acid. This was hypothesized to be due to the formation of dimer chains between malonic acid molecules, reducing their overall mobility. They also determined that the ionic diffusion occurred via hopping mechanism, similar to what has been demonstrated for ILs,[114] and different from conventional liquids, where the diffusion occurs via random walks of motion. Years later, Wagle *et. al.* studied Glyceline with quasi-elastic neutron scattering (QENS) and determined that choline actually diffuses faster than glycerol on the nanoscale level. As stated in the previous section, choline occupies the interstitial voids of cage-like glycerol molecules.[113] It was determined here that the localized diffusive motions, at much smaller timescales than the long range translational diffusion, are more constrained for glycerol than choline.

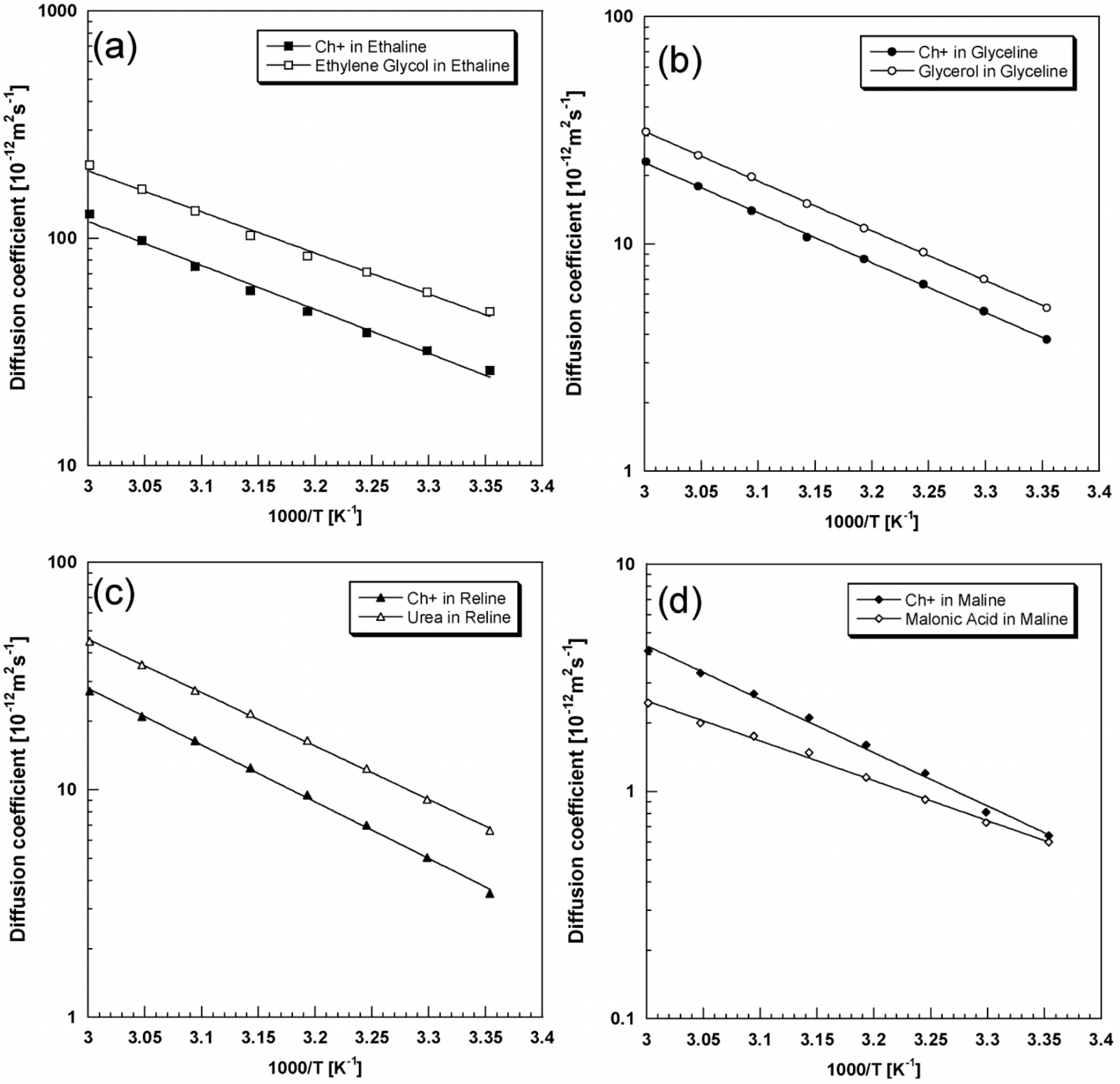

Figure 2.7: Arrhenius plots of the self-diffusion coefficients of choline and the corresponding HBD for (a) Ethaline, (b) Glyceline, (c) Reline, and (d) Maline. Reprinted with permissionfrom [7].

Reuter *et. al.* used broadband dielectric spectroscopy (BDS) to study orientational dynamics in Ethaline, Reline, and Glyceline.[115] They found that the Ethaline had the fastest rate of orientational dynamics, Reline had the slowest, and Glyceline was in between them. This could be expected when considering Lindemann's criterion ($\mathrm{T_g}$=2/3$\mathrm{T_m}$) and their reported $\mathrm{T_m}$s: $\mathrm{T_{m,Ethaline}} < \mathrm{T_{m,Glyceline}} < \mathrm{T_{m,Reline}}$. While at room temperature and above the rates get closer together, a separation of several orders of magnitude is noticed as temperature is lowered and the glass transition is approached. They also reported a strong coupling of the structural relaxation and the ionic conductivity. Other dielectric studies on DESs have been limited,[116, 117, 118] and remain to be scarce since this publication in 2018, despite the insight given using BDS. One stand-out paper though, however, from Rajbangshi *et. al.* concluded from MD simulations and dielectric relaxation measurements that there is a decoupling of translational and rotational diffusion in Reline,[119] which could mean that Stokes-Einstein equation is valid for Reline.

The effect of water has also been a topic of interest considering their hygroscopic nature. D'Agostino *et. al.* used PFG-NMR to study the self-diffusion of the molecular and anionic species in anhydrous and aqueous solutions of Glyceline, Ethaline, and Reline.[120] They determined that the addition of water caused an increase in the diffusion coefficient, D, of all species in all DESs measured. Subsequently, a decrease in viscosity was observed. They also confirmed that the choline cation does diffuse in a Stokesian manner. Alfurayj *et. al.* used femtosecond time-resolved absorption spectroscopy (fs-TA), BDS, NMR diffusometry and broadband relaxometry, and MD simulations to study anhydrous Ethaline and 0.1-28.5 wt% water in Ethaline. Interestingly, it was determined that concentrations below 1% water slow the solvation and rotational dynamics, but in the 1-28.5% water concentration range, the dynamics are enhanced.

Overall, several groups have started to build a solid foundation of understanding molecular structure and dynamics, and how that affects the macroscopic properties observed. However, substantial work is still needed to fill the gaps. Additionally, few groups have touched on the relations mentioned in Section 2.1, so it is unclear when and if those relations are valid or not. Having a better understanding of this would allow better predictions of properties to be observed without having to study in depth each DES of interest. Understanding the relationships between structure and properties as well as properties to other properties (*e.g.* viscosity to conductivity), if any exist, is essential to exploitation of these unique materials.

Chapter 3

Experimental Methods

In this chapter, the experimental techniques used for this dissertation are discussed: (i) differential scanning calorimetry, (ii) dynamic mechanical spectroscopy, and (iii) broadband dielectric spectroscopy. These will be divided into three sections (3.1-3.3), where the history, theory, and data analysis for each technique will be gone over. Data from additional techniques obtained from collaborators is included in the later chapters, and their experimental or computational details are given in Sections 4.3 and 5.3. This chapter is focused on the methods obtained in-house. Differential scanning calorimetry is used to study the phase behavior and obtain phase diagrams of DESs. Dynamic mechanical spectroscopy is used to study the viscoelastic behavior of DESs near the glass transition, also yielding information about viscosity. Finally, broadband dielectric spectroscopy is used to obtain information about rotational dynamic modes as well as quantities like dc ionic conductivity and the dielectric constants.

3.1 Differential Scanning Calorimetry

Differential scanning calorimetry (DSC) is a technique that measures the heat flow in and out of a material when subjected to a temperature profile. This was first patented in 1962 by Emmett Watson and Michael J. O'Neill.[121] There are several different types of DSC, including power scan, heat flux, and fast-scan, which all vary in how they fundamentally

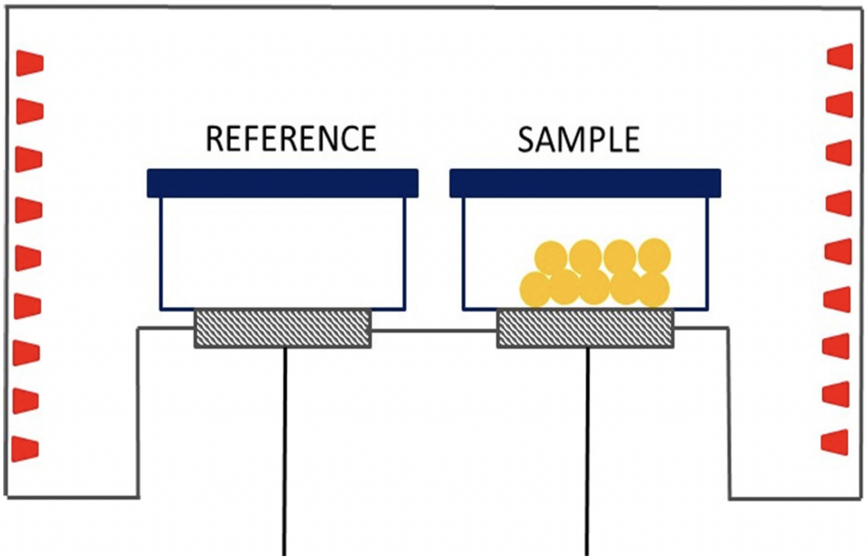

Figure 3.1: Schematic of heat-flux differential scanning calorimetry set up. Adapted from with permission from [8].

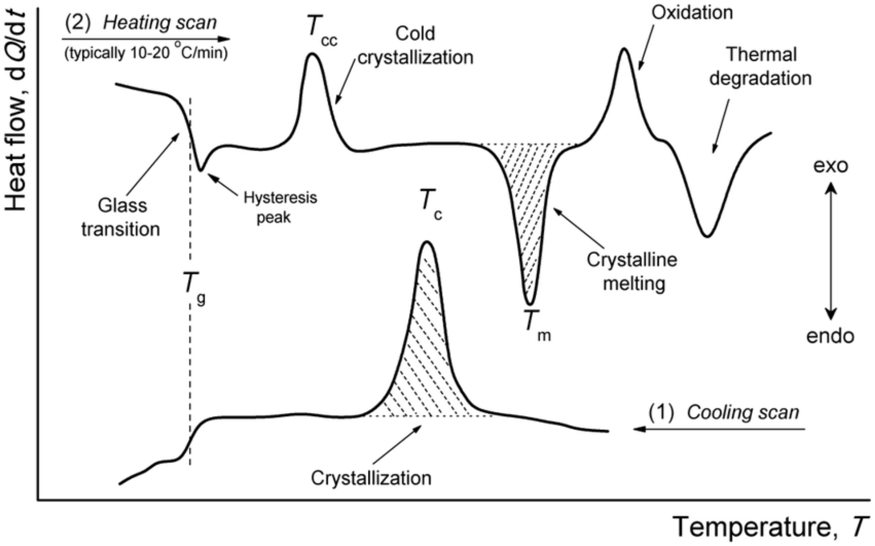

Figure 3.2: General thermogram, plotting heat flow versus temperature, showing different transitions that may occur during a measurement. Reproduced from [9].

operate. Heat flux DSC is the type used in this dissertation, and therefore is the focus of this section. DSC has become widely used as a thermal analysis technique due to its accurate measurements, small amount of sample needed, and the extensive amount of information obtained from it. Phase, physical, and chemical transitions such melting, crystallization, mixing, and chemical reactions can be observed using DSC.

The instruments used for these experiments were a TA Instruments Q2000 and a TA Instruments Discovery DSC 2500 (both heat flux) with a TA Instruments Discovery Finned Air Cooling System for temperature control. A simplified version of a heat flux DSC setup is depicted in Figure 3.1. There are two separate hermetically sealed aluminum pans used: a reference pan and a pan with typically 5-20 mg sample of interest. They sit on a thermoelectric disk which is surrounded by a furnace.[122] The furnace is heated electrically or cooled with a liquid nitrogen or a refrigerator cooling system at a linear heating or cooling rate. During heating cycles, the thermoelectric disk transfers the heat to both of the pans, which is measured by the thermocouple. There is a difference in heat absorbed and therefore temperature between the pans due to the heat capacity, C_p, of the sample. The temperature difference between the pans is determined by Ohm's Law:

$$\Delta T = qR \tag{3.1}$$

where q is the heat flow and R is the resistance of the thermoelectric disk.

A useful derivative of conventional DSC is modulated differential scanning calorimetry (MDSC). As opposed to a simple linear temperature profile, a low-frequency sinusoidal oscillating temperature profile is overlaid on the linear profile. With this, the average temperature changes continuously, but it is not linear. As a result, noise is reduced during measurements and the baseline flatness is improved as well as overall resolution. Additionally, quantities such as heat capacity can be obtained using MDSC, which are not obtainable using conventional DSC.

As temperature is varied in a sample, changes in heat flow will be observed, which correspond to some type of transition taking place. First focusing on the heating scan of

Figure 3.2, at the lower arbitrary temperatures, the glass transition is observed, and appears as step-like changes in the heat flow. This can sometimes be followed by a hysteresis peak, which would depend on the thermal history of the material. As temperature is increased, cold crystallization and oxidation would be observed as exothermic peaks. Melting and degradation are observed as endothermic peaks. Cold crystallization will only occur if the sample was first supercooled into its glassy state‘. Therefore, if the material has a strong tendency to crystallize over forming a glass, the cooling cycle can be examined to see the crystallization peak. The shape and intensity of these peaks depends on many things, such as heterogeneities and thermal history of the sample.

As previously stated in Chapter 2, the defining feature of DESs is the depressed melting temperature, T_m. However, features in the phase behavior can tell us a surplus of information. Figure 3.3 shows the thermograms for neat 1,4-butanediol (14BD), 15mol% ChCl in 14BD, and 33mol% ChCl in 14BD. Only a single melting event is observed in neat 14BD (top panel). However, as ChCl composition is increased, several cold crystallization (inside the red rectangles) and melting (inside the blue rectangles) events occur. This indicates that the addition of ChCl to 14BD makes the environment more amorphous, reducing its tendency to crystallize, since we observe cold crystallization. The different events of the same type of transition could indicate that there are dynamic or spatial heterogeneities present that crystallize and melt at different temperatures. While these cannot be confirmed or denied with DSC alone, it does generally illustrate a complex environment is present. Since there are sometimes several melting events that occur, we denote the liquidus temperature, (T_L), as the final melting temperature where the the last crystalline domain melts.

3.2 Dynamic Mechanical Spectroscopy

Generally, dynamic mechanical spectroscopy (DMS) measures the stress response of a material to an applied strain as a function of time and temperature. Oscillatory shear rheology, a main technique used in this dissertation, imposes a mechanical shear through sinusoidal oscillations on the material at various frequencies. [123] The response measured

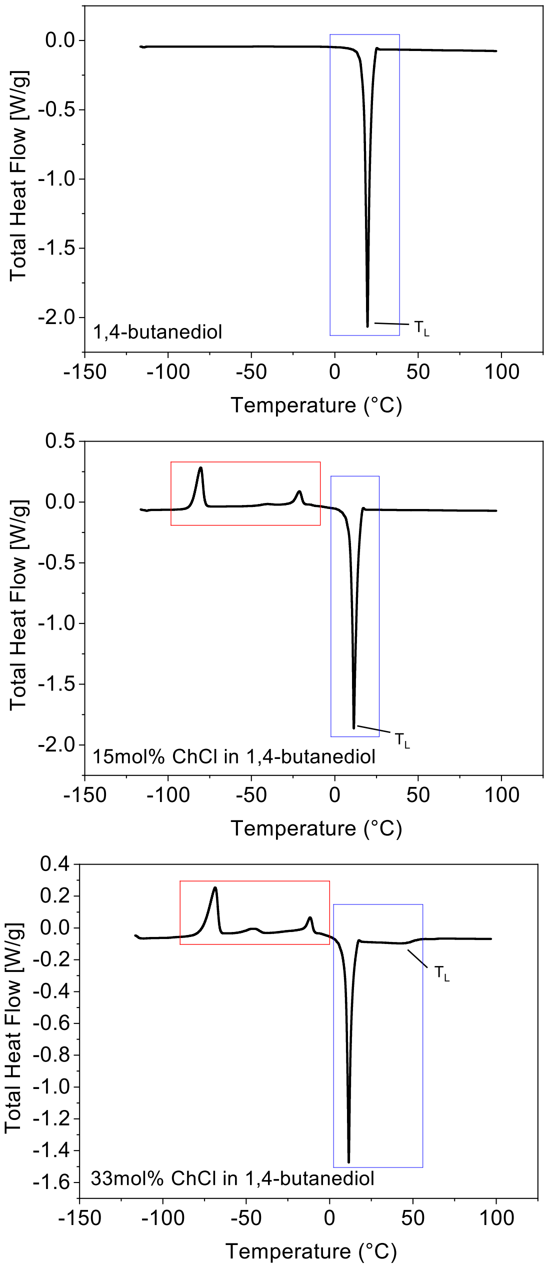

Figure 3.3: Thermograms for 1,4-butanediol (top), 15mol% ChCl in 1,4-butanediol (middle), and 33mol% ChCl in 1,4-butanediol (bottom). Blue and red rectangles indicate regions where melting and crystallization events occur, respectively.

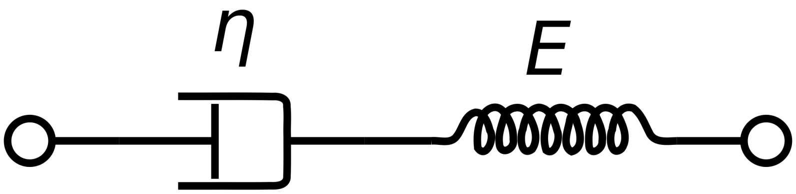

Figure 3.4: A schematic representation of the Maxwell model for viscoelastic liquids, where a Newtonian dashpot and Hookean spring assembled in series.

will depend on the type of motion the molecules experience at the applied temperature and the frequency range. For example, supramolecular dynamics will be measured at lower (slower) frequencies relative to orientational dynamics.

Materials that experience both viscous and elastic behavior when undergoing deformation are referred to as viscoelastic materials. To model this behavior, James Clerk Maxwell developed a model which considers a Newtonian dashpot and Hookean spring assembled in series. This is depicted in Figure 3.4, where the dashpot is under η indicating viscous behavior and the spring is under the E indicating elastic behavior. At frequencies above the timescale of molecular motion, when the material is responding as an elastic solid, the shear stress response can be written as:

$$\sigma = G\gamma \tag{3.2}$$

where G is the shear modulus and gamma is the strain. At frequencies slower than the rate of molecular motion, the molecules have time to move past each other and the material behaves viscous. This behavior can be described by Newton's law of viscosity:

$$\sigma = \eta \frac{\partial \nu_x}{\partial y} = \eta \dot{\gamma} \tag{3.3}$$

where η is the zero-shear viscosity and $\frac{\partial \nu_x}{\partial y}$ and $\dot{\gamma}$ are the strain rate. To reiterate, when the material is not given enough time to respond to the strain, it acts as a solid (Equation 3.2) which is accounted for by the spring. However, at slower timescales, the material is able to respond as a viscous liquid (Equation 3.3), which is accounted for by the dashpot. Together, the Maxwell model accounts for both behaviors exhibited in a viscoelastic liquid. The total strain is given by:

$$\gamma_0 = \gamma_E + \gamma_V \tag{3.4}$$

where E and V denote the elastic and viscous responses respectively.

A TA instruments Discovery Hybrid Rheometer-2 with a TA Instruments Environment Test Chamber (accuracy better than ±0.1 K) for temperature control was used for the experiments in this dissertation. The samples were loaded between parallel plates. The

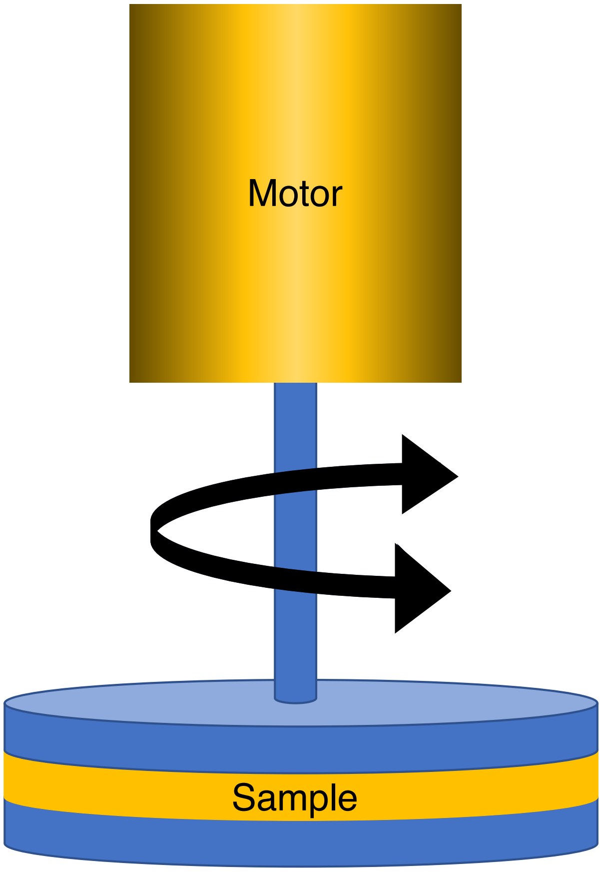

Figure 3.5: A schematic for oscillatory shear rheology. The sample is loaded in between two parallel plates to which an oscillating strain is imposed upon using a transducer (electrical motor).

plates used were 3 and 8 mm disposable aluminum plates. A schematic of an oscillatory shear rheology experient using this setup is given in Figure 3.5. The top plate oscillates above the sample imposing a sinusoidal strain, given by: $\gamma = \gamma_0 \sin(\omega t)$. The time derivative of this is:

$$\dot{\gamma} = \frac{\partial \gamma}{\partial t} = \frac{\partial \gamma_E}{\partial t} + \frac{\partial \gamma_V}{\partial t} \omega \gamma_0 \cos \omega t = \frac{1}{G_0} \frac{\partial \sigma}{\partial t} + \frac{1}{\eta_0} \sigma \tag{3.5}$$

Using the solution $\sigma(t) = A \sin(\omega t) + B \cos(\omega t)$, we can obtain:

$$\sigma(t) = \frac{G_0 \gamma_0 \omega^2 \tau^2}{\omega^2 \tau^2 + 1} \sin(\omega) + \frac{G_0 \gamma_0 \omega \tau}{\omega^2 \tau^2 + 1} \cos(\omega) \tag{3.6}$$

$$\sigma(t) = G' \gamma_0 \sin(\omega t) + G'' \gamma_0 \cos(\omega t) \tag{3.7}$$

The terms G' and G'' refer to the real and imaginary parts of the complex shear modulus, $G^*(\omega) = G'(\omega) + iG''(\omega)$. G' is the storage modulus, which is in phase with γ, and consequently related to the elastic response. Alternatively, G'' is the loss modulus, which is 90° out of phase with the strain, meaning it is in phase with $\dot{\gamma}$ and related to the viscous response of a material. Using the shear modulus allows us to obtain data in the frequency domain. Additionally, the real and imaginary parts of complex shear modulus can be related to the real and imaginary parts of the complex viscosity as $\eta'(\omega) = G''(\omega)/\omega$ and $\eta''(\omega) = G'(\omega)/\omega$.

Viscoelastic materials can be fit with the Maxwell model for the complex shear modulus, given by:

$$G^*(\omega) = G_\infty \left[1 - \frac{1}{1 + i\omega\tau} \right] \tag{3.8}$$

where G_∞ is the high frequency shear modulus and τ is the relaxation time.[124, 125] Similarly to the modified Debye functions described in the Section 3.3.1, shape parameters can be added to the Maxwell model to account for broadening in the curve due to a larger distribution of relaxation times. A Cole-Davidson modified Maxwell model is expressed in Equation 3.9.[126]

$$G^*(\omega) = G_\infty \left[1 - \frac{1}{(1 + i\omega\tau)^\gamma} \right] \tag{3.9}$$

where gamma is a shape parameter.

3.3 Broadband Dielectric Spectroscopy

Dielectric spectroscopy (DS) measures the polarization response of a material to an alternating electric field. The history of this technique dates back to the 1770s, beginning with the unpublished work of Henry Cavendish. Over a century later, in 1879, after other scientists had obtained the same results and been credited for them, James Clerk Maxwell collected and published Cavendish's findings. Most notably pertaining to DS, Cavendish discovered that the capacitance (the ratio of charge to voltage, $C = q/V$) of Leyden jar or condenser (early names for a capacitor) was dependent on the insulating material between the electrodes, as well as the thickness of the electrodes, at a constant V. Michael Faraday later developed this postulation and defined this property as the specific inductive capacity, more commonly known present day as the relative dielectric permittivity, $\varepsilon = C/C_0$, where C is the capacitance and C_0 is the capacitance of a reference.

3.3.1 General Theory

In 1864, Maxwell formulated four foundational equations which relate electric, magnetic, and light phenomena in what is now known as electromagnetic theory:

$$\nabla \cdot \mathbf{B} = 0 \tag{3.10}$$

$$\nabla \times \mathbf{E} = -\frac{\partial}{\partial t}\mathbf{B} \tag{3.11}$$

$$\nabla \cdot \mathbf{D} = \rho_e \tag{3.12}$$

$$\nabla \times \mathbf{H} = \vec{j} + \frac{\partial}{\partial t}\mathbf{D} \tag{3.13}$$

where $\mathbf{B}$ is the magnetic induction, $\mathbf{H}$ and $\mathbf{E}$ are the electric and magnetic fields, $\mathbf{D}$ is the dielectric displacement, ρ_e is the charge density, and $\vec{j}$ is the electric current. For small electric fields (<10^6 V/m), the dielectric displacement can be further defined as:

$$\mathbf{D} = \varepsilon^* \varepsilon_0 \mathbf{E} \tag{3.14}$$

where ε^* is the complex dielectric function and the constant $\varepsilon_0 = 8.854 \times 10^{-12}$ F/m is the permittivity of a vacuum. **D** occurs from the displacements bound charges within the dielectric medium. Moreover, polarization, **P**, describes the dielectric displacement from motion of mobile charge carriers in the medium. Therefore, it can be defined as:

$$\mathbf{P} = \mathbf{D} - D_0 = \varepsilon^* \varepsilon_0 \mathbf{E} - \varepsilon_0 \mathbf{E} = \varepsilon_0 \mathbf{E}(\varepsilon^* - 1) \tag{3.15}$$

where D_0 is the dielectric displacement of an empty capacitor. Also, $\varepsilon^* - 1 = \chi^*$ can be defined as the dielectric susceptibility.

We know now that **P** is directly related to **E** as well as ε^*, which per Maxwell's equations, we also know is time or frequency dependent. The complex dielectric function can be separated into its real and imaginary parts as: $\varepsilon^*(\omega) = \varepsilon'(\omega) - i\varepsilon''(\omega)$, where $i = \sqrt{-1}$, $\omega = 2\pi\nu$ is radial frequency and ν is frequency. The time-dependent applied electric field can be defined as $\mathbf{E}(t) = \mathbf{E}_0 \exp(-i\omega t)$. Additionally, Ohm's Law relates the current density to the electric field:

$$\vec{j} = \sigma^* \mathbf{E} \tag{3.16}$$

where σ^* is the complex conductivity function. Therefore, using the equations and relations mentioned thus far, the complex conductivity function can be related to the complex dielectric function as:

$$\sigma^*(\omega) = i\omega\varepsilon_0\varepsilon^*(\omega) \tag{3.17}$$

The complex conductivity function can also be separated into its real and imaginary parts: $\sigma^*(\omega) = \sigma'(\omega) + i\sigma''(\omega)$. Dielectric data is commonly analyzed in terms of $\varepsilon'(\omega)$, $\varepsilon''(\omega)$, $\sigma'(\omega)$, and/or $\sigma''(\omega)$.

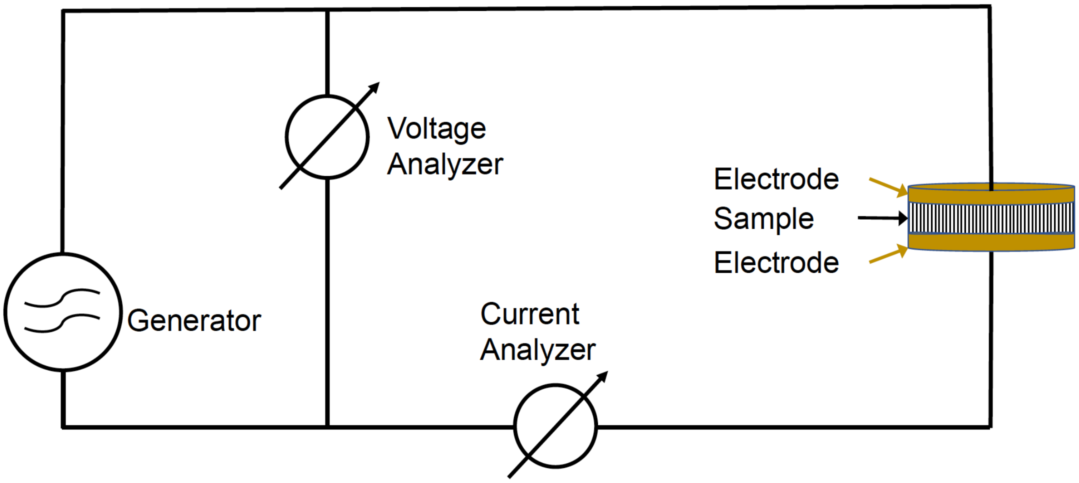

Figure 3.6: A schematic of a simplified dielectric spectrometer apparatus.

To make a dielectric spectroscopy measurement in the 10^{-6} Hz to 10^{11} Hz range, a sample is loaded in a parallel plate capacitor, which (a simplified version of this) is depicted in Figure 3.6. To make a measurement, the generator is used to apply a frequency dependent voltage, $U^*(\omega)$, to the capacitor and the current response, $I^*(\omega)$ is measured. Complex impedance can be determined by taking the ratio of applied voltage to the measured current, which can also be related to the inverse of complex capacitance:

$$Z^*(\omega) = \frac{U^*(\omega)}{I^*(\omega)} = \frac{1}{i\omega C^*(\omega)}. \tag{3.18}$$

Since $\varepsilon^*(\omega) = C^*(\omega)/C_0$, we know now that:

$$\varepsilon^*(\omega) = \frac{I^*(\omega)}{i\omega C_0 U^*(\omega)}. \tag{3.19}$$

To cover this wide frequency domain, the instrument utilizes Fourier correlation analysis in concert with dielectric converters, which increases accuracy and reduces noise as well.

The polarization can be related to microscopic dipole moments as:

$$\mathbf{P} = \frac{1}{V}\sum p_i \tag{3.20}$$

where V is the volume and p is the microscopic dipole moment of the molecule or particle for i dipole moments in the system. The dipole moments can be permanent or induced by a local electric field, $\mathbf{E}_l$. The total polarization can be separated into the permanent and induced components as $\mathbf{P} = \mathbf{P}_\mu + \mathbf{P}_\infty$. The induced polarization can be defined as $\mathbf{P}_\infty = \sum_k n_k \alpha_k (\mathbf{E}_l)_k$, where n is the number density of molecules k and α is the polarizability. Similarly, the permanent dipole or orientational polarization is given by $\mathbf{P}_\mu = \sum_k n_k \overline{\mu_k}$, where n is the number density of dipoles k and $\overline{\mu_k}$ is the mean dipole moment. Concerning systems with only one type of dipole, the summation may be removed.

Under the assumptions that dipoles are non-interacting or negligible and $\mathbf{E}_l$ is equal to the applied external electric field, $\mathbf{E}_d$, the interaction energy of a dipole in an external electric field can be written as $U = -\mu \cdot \mathbf{E}_d = -|\mu||\mathbf{E}_d|\cos(\theta)$, where θ is the angle of the dipole to the $\mathbf{E}_d$. Boltzmann's statistics states that the mean dipole moment resulting from

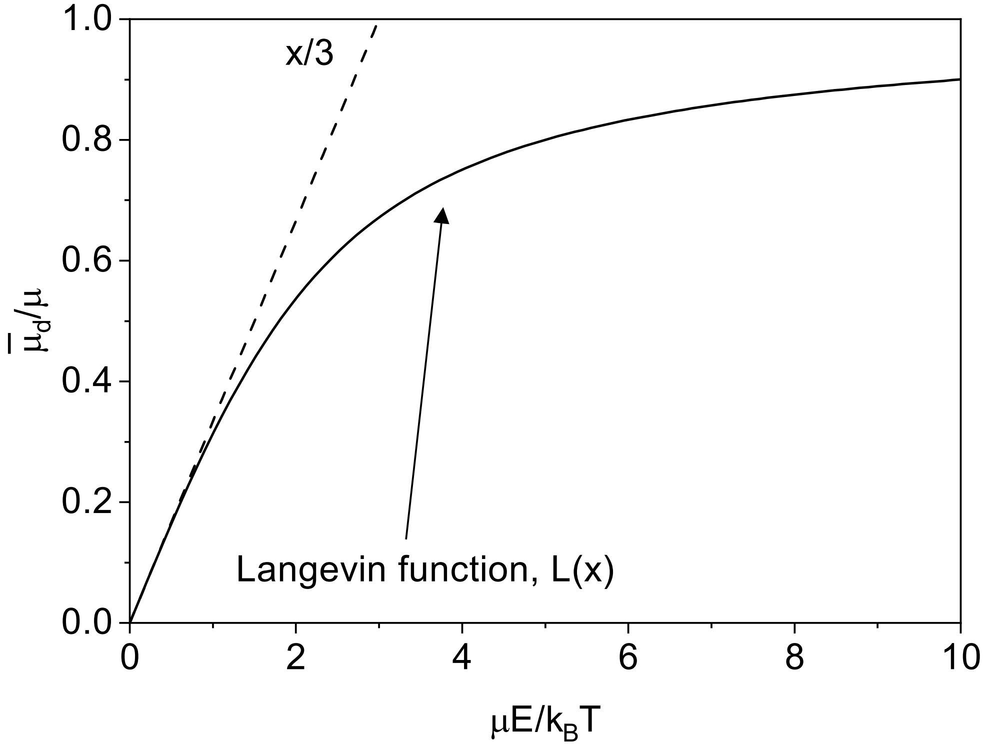

Figure 3.7: Solid line: Langevin function, $L(x)$, given in Equation 3.22 plotted as $\overline{\mu_d}/\mu$ versus $\mu\mathbf{E}/k_BT$. Dashed line: Simplification to $L(x) \approx x/3$ for low electric fields.

orientational polarization is defined as:

$$\overline{\mu_k} = \frac{\int_0^\pi \mu \cos\theta \exp\left(\frac{|\mu||\mathbf{E}_d|\cos\theta}{k_B T}\right)\frac{1}{2}\sin\theta \; d\theta}{\int_0^\pi \exp\left(\frac{|\mu||\mathbf{E}_d|\cos\theta}{k_B T}\right)\frac{1}{2}\sin\theta \; d\theta} \tag{3.21}$$

We can substitute $x = \frac{|\mu||\mathbf{E}_d|}{k_B T}$ into Equation 3.21 and solve the integrals, yielding:

$$\frac{\overline{\mu_k}}{\mu} = \coth x - \frac{1}{x} \tag{3.22}$$

which is known as the Langevin function, $L(x)$. For electric field strengths $\leq 10^6 \; V/m$, the mean dipole moment from orientational polarization varies linearly as $\overline{\mu_k} = \frac{|\mu|^2}{3k_B T}\mathbf{E}_d$. This yields an approximation of the Langevin function to be reduced to $L(x) \approx x/3$. The original Langevin function and simplified version for low electric fields are both plotted in Figure 3.7.

Now, the total polarization can be written as:

$$\mathbf{P} = \mathbf{P}_\mu + \mathbf{P}_\infty = \varepsilon_0 \mathbf{E}(\varepsilon^* - 1) = \sum_k n_k[\alpha_k(\mathbf{E}_l)_k + \frac{\mu^2}{3k_B T}(\mathbf{E}_d)_k] \tag{3.23}$$

for the polarization response of a dielectric material to an external electric field. Peter Debye's approach to solve this equation for total polarization was to set the local, external, and Lorentz electric fields equal to each other. The Lorentz field is derived from considering virtual sphere inside a dielectric material that is homogeneously polarized with a constant dielectric permittivity, where the external electric field induces charges on the outer surface of the sphere. The expression for Debye's original approach is given by:

$$\mathbf{E}_L = \mathbf{E}_l = \mathbf{E}_d = \mathbf{E}\left(1 + \frac{\varepsilon + 2}{3}\right) \tag{3.24}$$

where $\mathbf{E}_L$ is the Lorentz field and ε is the low frequency limit in the real part of the complex dielectric function. If substituted back into Equation 3.23, we obtain:

$$\frac{\varepsilon - 1}{\varepsilon + 2} = \frac{n}{3\varepsilon_0}\left(\alpha + \frac{\mu^2}{3k_B T}\right) \tag{3.25}$$

which is the infamous Debye formula.[127, 128] For non-polar dielectric materials with no permanent dipole, the orientational polarization component can be removed, simplifying the equation to:

$$\frac{\varepsilon_\infty - 1}{\varepsilon_\infty + 2} = \frac{n\alpha}{3\varepsilon_0} \tag{3.26}$$

which is known as the Clausius-Mossotti formula for the high frequency limiting permittivity, ε_∞.[129] This can also be applied to polar dielectrics in the high frequency limit.

The Debye formula gives accurate estimations for μ for polar molecules in the gas phase or dilute solutions of polar molecules in a nonpolar solvent. However, it fails for polar, liquid dielectric materials due to the poor approximation of the local electric field, $\mathbf{E}_l$, by the Lorentz field, $\mathbf{E}_L$. To address this, Lars Onsager developed an approach which accounts for additional polarizations using reaction field theory. The reaction field of the spherical cavity is parallel to the permanent dipole moment in the center of the cavity. The Onsager cavity yields more accurate approximations of the local electric field than the Lorentz cavity.[130] This yields the Onsager equation:

$$\varepsilon_s - \varepsilon_\infty = \frac{3\varepsilon_s}{2\varepsilon_s + \varepsilon_\infty}\left(\frac{\varepsilon_\infty + 2}{3}\right)^2 \frac{n\mu^2}{3k_B T} \tag{3.27}$$

where ε_s is the static dielectric permittivity. This equation provides good results for non-interacting dipolar liquids. However, it fails for dipolar materials where the intermolecular interactions, such as hydrogen bonding, are present.

John Gamble Kirkwood and Herbert Fröhlich added a term to this, known as the Kirkwood-Fröhlich correlation factor, $g_k = 1 + z\overline{\cos\gamma}$,[131, 132] to account for these interactions, which yields:

$$\varepsilon_s - \varepsilon_\infty = \frac{3\varepsilon_s}{2\varepsilon_s + \varepsilon_\infty}\left(\frac{\varepsilon_\infty + 2}{3}\right)^2 \frac{n\mu^2}{3k_BT}(1 + z\overline{\cos\gamma}) \tag{3.28}$$

where z is the average number of nearest neighbors to a dipole and γ is the angle of orientation between dipoles. When $g_k > 1$, the dipoles are aligned parallel to one another, and vice versa for $g_k < 1$, the dipoles are aligned anti-parallel resulting in higher or lower ε_s values compared to those from the Onsager equation respectively.

This is the case for a system under a direct current (dc) voltage for a long enough period of time where the polarization response of a dielectric material reaches equilibrium. Now, we will consider what occurs when the that external electric field is removed or turned off. When this occurs, the molecules will begin to relax until a new equilibrium is formed. For small electric fields, the following equation can be used to describe the time-dependent polarization response to a step change in the external electric field:

$$\mathbf{P}(t) = \mathbf{P}_\infty + \varepsilon_0 \int_\infty^t \varepsilon(t - t')\frac{d\mathbf{E}(t')}{dt'}dt' \tag{3.29}$$

When the electric field is alternating or oscillating at a certain frequency, it can be described by: $\mathbf{E}(t)(\omega) = \mathbf{E}_0 \exp(-i\omega t)$. Therefore, Equation 3.29 can be rewritten as:

$$\mathbf{P}(t)(\omega) = \varepsilon_0(\varepsilon^*(\omega) - 1)\mathbf{E}_0 \exp(-i\omega t) \tag{3.30}$$

Now, the complex dielectric function can be defined as:

$$\varepsilon^*(\omega) = \varepsilon'(\omega) - i\varepsilon''(\omega) = \varepsilon_\infty - \int_0^\infty \frac{d\varepsilon(t)}{dt}\exp(-i\omega t)dt \tag{3.31}$$

Using the correlation function $\phi(t) = \exp -t/\tau$, where t time and τ is the dipole relaxation time, we can perform a Laplace transform into the frequency domain:

$$\varepsilon^*(\omega) = \varepsilon_\infty - \Delta\varepsilon \int_0^\infty \exp(-i\omega t)\frac{d\phi(t)}{dt}dt = \varepsilon_\infty + \frac{\Delta\varepsilon}{1 + i\omega\tau} \tag{3.32}$$

where $\omega = 2\pi\nu$ is the radial frequency, ε_∞ is the high frequency limiting value of $\varepsilon'(\omega)$, $\Delta\varepsilon$ is the dielectric strength of the relaxation, and τ is the characteristic dipole relaxation time. This is commonly known as the Debye equation for dipolar relaxations. This describes a relaxation process with a single relaxation time. However, the majority of liquids experience a wide distribution of relaxation times.

To describe such a system in the time domain, a stretched exponential correlation function can be used. The Kohlrausch-Williams-Watts (KWW) equation, $g(t) = \exp(-t/\tau)^\beta$,[133] can be used, where β is a stretching/fitting parameter. In the frequency domain, several modifications of the Debye equation have been made to describe the stretching or broadening that occurs in non-Debye like liquids. The most general form is the Havriliak-Negami function, written as:

$$\varepsilon^*(\omega) = \varepsilon_\infty + \frac{\Delta\varepsilon}{(1 + (i\omega\tau_{HN})^\gamma)^\beta} \tag{3.33}$$

where γ and β are fitting parameters. When $\beta = 1$, this is the Cole-Cole modification, and when $\gamma = 1$, the Cole-Davidson modification is obtained.

3.3.2 Analysis of Dielectric Spectra

The primary spectrometer used in this dissertation is a Novocontrol High Resolution Alpha Dielectric Analyzer in combination with a Quatro cryogenic temperature control system perform the dielectric measurements from 10^{-1} to 10^7 Hz in the temperature range of 150 K to 400 K, with accuracy better than ±0.1 K. In addition, an Agilent E5071C Vector Network Analyzer is used to obtain room temperature dielectric measurements from 3×10^5 to 2×10^9 Hz. For the samples measured with the Novocontrol system, the material was loaded in parallel plate capacitor geometry with 20 mm diameter gold-plated brass electrodes, as shown earlier in Figure 3.6.

The complex dielectric function is frequency and temperature dependent due to being related to the the polarization response of a material, which gives rise to relaxation phenomena that can be observed in ε' and ε''. In the real part of $\varepsilon^*(\omega)$, which can be thought of as energy stored in the dielectric material, a relaxation process can be observed

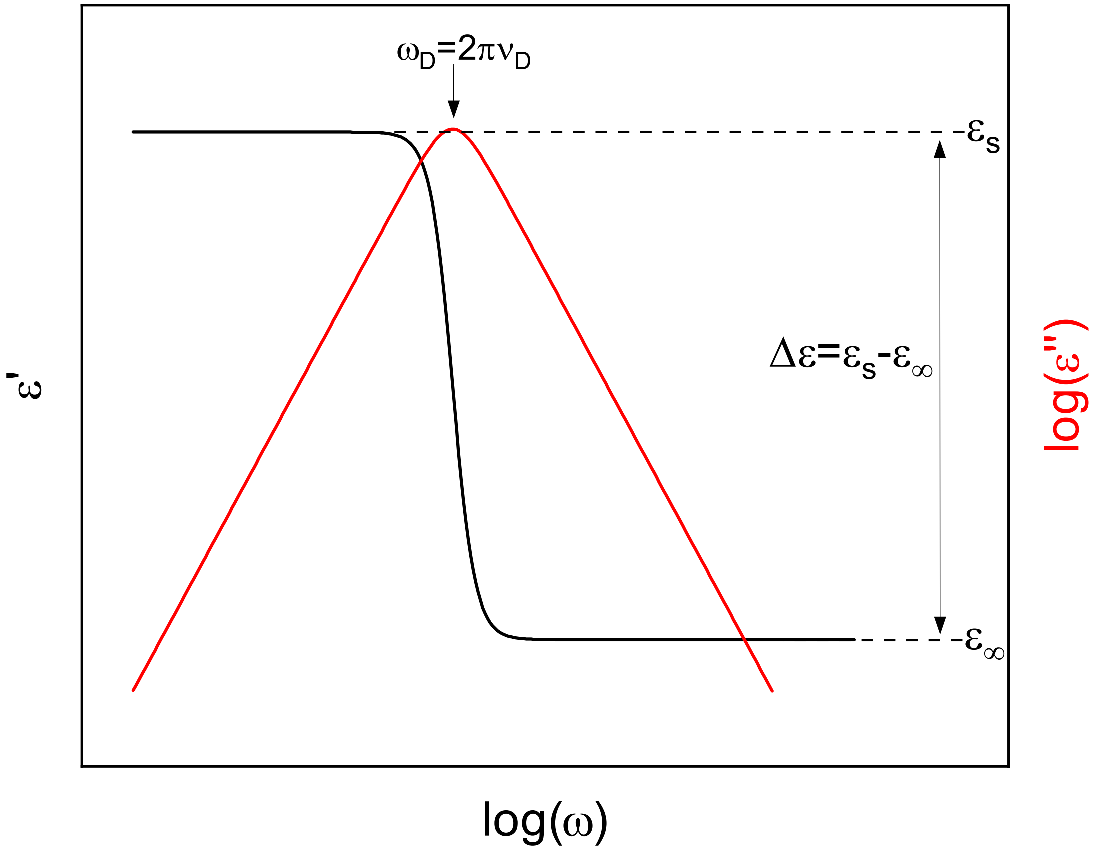

Figure 3.8: The real and imaginary parts of the complex dielectric function plotted versus arbitrary frequency for a Debye function. Important qualities such as ω_D, ε_s, ε_∞, and $\Delta\varepsilon$ are pointed out on the curves. Recreated from [10].

as a step-like decrease. In the imaginary part of $\varepsilon^*(\omega)$, which can be viewed as the energy dissipated by the dielectric material, a relaxation process can be observed as a peak or hump. The real and imaginary parts of the complex conductivity function also display the relaxation processes in different ways, but our primary focus for analysis in this dissertation is $\varepsilon^*(\omega)$.

Figure 4.1 provides an example of the real and imaginary parts of the complex dielectric function for a generic Debye relaxation, highlighting the important features. The low and high-frequency limiting values, ε_s and ε_∞ respectfully, are pointed out using dashed lines. The difference between them is the dielectric strength of the relaxation, $\Delta\varepsilon$, is shown within the dotted line. The characteristic relaxation time for a Debye relaxation, τ_D is shown at the peak maximum in ε'' or the halfway point for the step in ε'. It should be noted that in the modified functions, such as the Havriliak-Negami function shown in Equation 3.33, τ_{HN} does not correspond to the peak maximum of the relaxation in ε''. The frequency of the peak maximum can be calculated using the following equation:

$$\omega_{max} = \frac{1}{\tau_{HN}} \left[\sin \frac{\beta\pi}{2+2\gamma}\right]^{1/\beta} \left[\sin \frac{\beta\gamma\pi}{2+2\gamma}\right]^{-1/\beta} \tag{3.34}$$

The types of polarizations that can occur, and therefore types of relaxation phenomena that can be observed, are plotted as a function of the time of the applied alternating current (ac) electric field in Figure 3.9. At very small, fast timescales, electronic and atomic polarizations occur, referring to the displacements of electrons and atoms respectively. These can be observed with techniques like ultraviolet–visible (UV-Vis) spectroscopy and infrared (IR) spectroscopy. At slightly larger, slower timescales, molecules with dipole moments will undergo orientational or dipolar polarization. The final two polarizations occur in dielectric materials with mobile charge carriers. First, ion hopping polarization occurs, which is the translational motion of charged species. Finally, at the slowest timescales, interfacial polarization occurs, where so much time passes that charges accumulate on the electrodes.

We have discussed models to describe orientational polarization in dipolar liquids. However, to describe the long-range translational diffusion of ions in ion-conducting

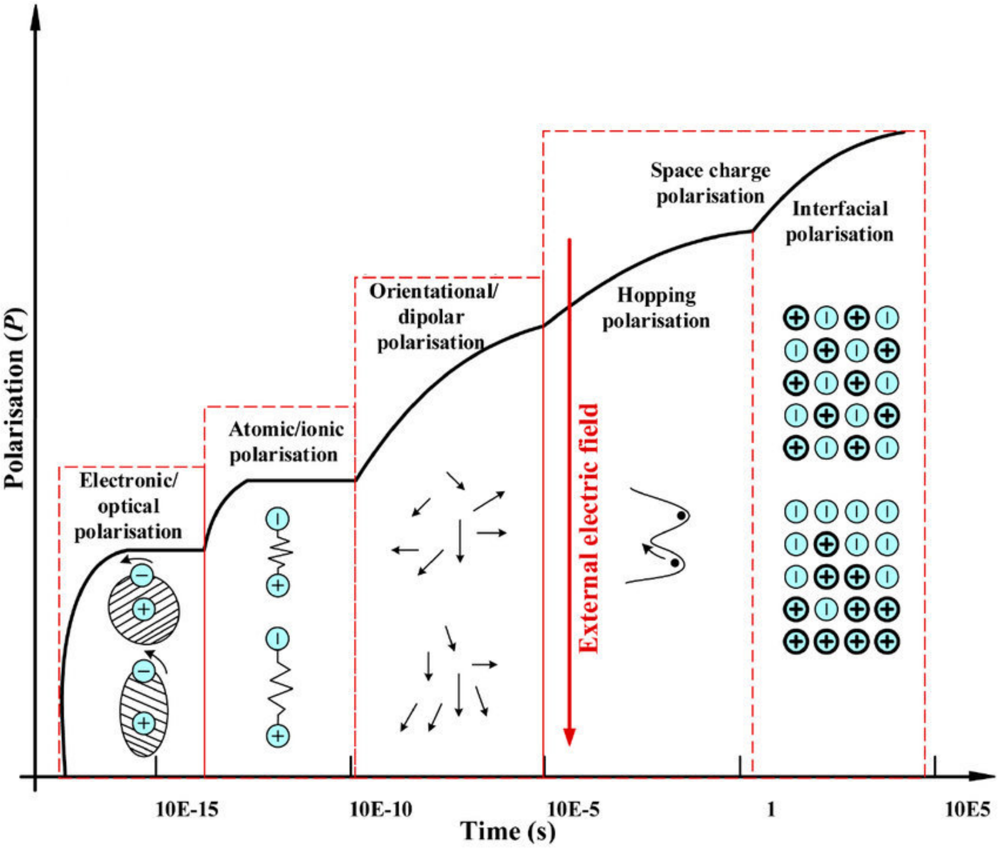

Figure 3.9: Types of polarization and a function of time of the ac electric field. Reprinted with permission from [11].

materials, Jeppe Dyre formulated the Random Barrier Model, given by:

$$\varepsilon^*(\omega) = \frac{\sigma_0}{i\omega\varepsilon_0}\frac{i\omega\tau_e}{\ln(1 + i\omega\tau_e)} \tag{3.35}$$

where σ_0 is the dc ionic conductivity obtained from the plateau in σ' and τ_e is the characteristic ion hopping time. This model describes an ion which has to overcome a randomly varying potential energy landscape to hop or move to the next spot. The onset of σ_0 correlates to the average time, τ_e, it takes for the ion to overcome the energy barrier.

Chapter 4

Enhancement of dynamics and ion transport at the eutectic composition in deep eutectic solvents

In this chapter, we will be exploring the importance of the eutectic composition regarding physicochemical properties. DESs are well-known for their depressed melting temperature, therefore, the eutectic composition for which this occurs is of clear importance. However, it is unclear if the eutectic composition is where the most optimal properties occur. Therefore, this study seeks to understand if the eutectic composition is influential on properties such as rate of orientational dynamics and dc ionic conductivity. DSC and BDS experiments were performed by the Joshua Sangoro group. The fs-TAS experiments were completed by the Clemens Burda group at Case Western Reserve University. My primary contributions were the Sangoro group experiments and data analysis, the interpretation of all results, and the writing. This paper is currently under review. Changes include supplementary information being integrated into the main text.

4.1 Abstract

Deep eutectic solvents (DESs) are a class of versatile solvents with promise for a wide range of applications from separation processes to electrochemical energy storage technologies. Fundamental understanding of the correlation among the structure, thermodynamics, and dynamics in these materials, necessary for targeted rational design for specific applications, is still at the nascent stage. Here, we employ differential scanning calorimetry (DSC), broadband dielectric spectroscopy (BDS), and femtosecond-transient absorption spectroscopy (fs-TAS) to investigate the correlation among thermodynamics, dynamics, and charge transport in mixtures comprising a wide range of compositions of choline chloride (ChCl) and ethylene glycol (EG). Detailed analyses reveal that (i) the eutectic composition of this prototypical DES occurs in the 15-20mol% ChCl in EG range rather than the previously assumed 33mol%, and (ii) both rotational dynamics and charge transport at the eutectic composition are enhanced in this composition range. These findings highlight the fundamental interplay between thermodynamics and dynamics in determining the properties of DESs relevant for many applications.

4.2 Introduction

Deep eutectic solvents (DESs) are a class of solvents that have shown great potential in many areas such as biomass processing,[134, 135, 136] pharmaceutical research,[137, 138, 139] CO_2 capture,[140, 141] and redox flow batteries.[100, 142, 101] The appeal for them as alternative solvents arises from their relative ease of synthesis from potentially inexpensive and sustainable parent materials.[117, 143] DESs are simply mixtures of two or more components that result in a depressed melting temperature, significantly below that of its parent compounds.[144] The resulting properties often include wide liquidus ranges, low volatility, low flammability, and high tunability.[2, 145, 84, 88] Since the design space for DESs is large, predictive knowledge and understanding of the impact of the chemical structure as well as composition on the physicochemical properties of the DES is important in selecting solvents for specific applications.[146] Many existing DES studies typically report properties or applications of DESs at one or two compositions, presumably due to the scarcity of data on the phase characteristics of the DES investigated. Furthermore, it has been suggested that the eutectic compositions do not necessarily matter in terms of the overall physicochemical properties of DESs and there are no "magic" compositions.[147] While this picture may indeed hold for a limited set of properties, the general validity of this conclusion is yet to be rigorously demonstrated.

Given that Ethaline is one of the prototypical DESs in the current literature due to its low viscosity relative to other DESs, it is an excellent model system to employ in evaluating the potential impact of thermodynamic transitions on macroscopic properties.[102] Ethaline was first reported by Abbott *et al.* as a 1:2 molar ratio of ChCl (T_m=575 K) to EG (T_m=260 K) with a freezing point of 283 K.[148] However, some more recent reports have also provided conflicting values of melting temperature (T_m), such as 237 K[149] and 207 K.[150] Additionally, Agieienko *et al.* reported that the actual eutectic composition is at 17.1mol% ChCl or a 1:4.85 molar ratio of ChCl to EG.[151] This raises a pertinent question: how does the existence of eutectic compositions impact dynamics and charge transport in deep eutectic solvents?

Here, we employ DSC, fs-TAS, and BDS to study ChCl and EG mixtures in a wide composition range to unravel the correlations between thermodynamic transitions and dynamics in these systems. We determine that the lowest liquidus temperatures occur in the 15-20mol% ChCl range, concomitant with the fastest dynamics measured by fs-TAS and BDS as well as the highest dc ionic conductivity determined by BDS at the same eutectic composition. It is suggested that the enhancement of transport and dynamics at the eutectic composition is intuitive based on the well-established Lindemann's criterion linking the melting temperatures to the glass transition. Knowledge of the range of compositions that yield eutectic systems may prove crucial role in many applications such as solvation in deep eutectic solvents.

4.3 Materials and Methods

4.3.1 Sample Preparation

EG was purchased from ACROS Organics at ≥99% purity. ChCl was purchased from Sigma Aldrich at ≥98% purity. The ChCl was dried in a vacuum oven for at least 48 hours days 70°C. EG was used as received. An appropriate amount of ChCl was added to EG, and stirred at 80°C in a dry nitrogen atmosphere until the mixture appeared homogeneous.[145] For fs-TAS experiments, Reichardt's dye (betaine-30) was added to the prepared mixtures to achieve absorption of 0.5 at the excitation wavelength.

4.3.2 Differential Scanning Calorimetry

Differential Scanning Calorimetry (DSC) was employed to study thermodynamic transitions in the samples. DSC testing was performed using a TA Instruments DSC 2500. The samples were prepared using hermetically sealed aluminum pans within an enclosed, nitrogen-purged glovebox to prevent exposure to ambient atmospheric conditions. Tests were performed for each composition using constant heat flow heating and cooling cycles from -120°C to 75°C. Each composition was first annealed $\approx$ 20°C above their respective melting points for 10 min, then thermodynamically cycled at a constant heating and cooling rate of 1 and 2°C/min using both the temperature modulated DSC (MDSC) scans for higher accuracy, and standard heat-cool-heat cycling to check for thermal reversibility of the melting signals and overall reproducibility of the measurements.

4.3.3 Steady-state UV-Vis Absorption Spectroscopy and Femtosecond Transient Absorption Spectroscopy

Steady-state UV-Vis measurements were performed using a Varian Cary 50 UV-Vis spectrophotometer. Femtosecond transient absorption (fs-TA) measurements were carried out using a Clark MXR 2010 femtosecond laser system that generates a fundamental output wavelength of 780 nm and 100 fs laser pulse duration at a pulse repetition rate of 1 kHz.

The laser beam was split to generate (i) a 390 nm pump pulse using a second harmonic generation crystal and (ii) a white-light continuum probe pulse by using a sapphire crystal. The probe light was delay-controlled using a computer-controlled optical delay stage. All fs-TA measurements were carried out in 2 mm quartz cuvettes at room temperature. Pump power was chosen as low as possible, which still provided a reliable signal-to-noise ratio in order to avoid unnecessary photodamage of the probe molecule B30 dye, at 40 mJ cm^{-2}. The fs-TA data were pulse chirp-corrected and globally fitted at selected monitoring wavelengths (550-600 nm) to biexponential decay functions, modeled by $TA(t,\tau) = A_1 e^{-t/\tau_1} + A_2 e^{-t/\tau_2}$, where A_1 and A_2 are amplitude coefficients which combine to unity, t is time, and τ_1 and τ_2 are the fitted time constants. Steady-state absorption spectra were taken before and after experiments to confirm that no photodegradation is indicated due to the laser spectroscopic experimentation.

4.3.4 Broadband Dielectric Spectroscopy

BDS measures the polarization response to an alternating electric field using a wide frequency and temperature range. The response is given in terms of complex permittivity, $\varepsilon^*(\omega) = \varepsilon'(\omega) - i\varepsilon''(\omega)$, and complex conductivity, $\sigma^*(\omega) = \sigma'(\omega) + i\sigma''(\omega)$, where ω is radial frequency. These functions are related to each other as $\varepsilon^*(\omega) = i\omega\varepsilon_0\sigma^*(\omega)$, where ε_0 is the permittivity of free space, making the imaginary part of complex permittivity directly related to the real part of complex conductivity. Because of this, in ion-conducting systems such as the ones measured in this work, dielectric relaxations can become overshadowed by contributions from the dc ionic conductivity. Therefore, we analyze the derivative representation of the dielectric loss, $\varepsilon''_{der} = -\pi/2(\partial\varepsilon'/\partial\ln(\omega))$, to uncover relaxations that might be obscured by conductivity contributions. Data was fit as described previously by Spittle *et al.*[152] Briefly, the data was fit using a linear combination of a Debye function, Havriliak-Negami function, and a Random Barrier Model:

$$\varepsilon^*(\omega) = \varepsilon_\infty + \frac{(\Delta\varepsilon)_{Debye}}{1 + i\omega\tau_{Debye}} + \frac{\sigma_0\tau_{ion}}{\varepsilon_0(ln(1 + i\omega\tau_{ion}))} + \frac{(\Delta\varepsilon)_\alpha}{(1 + (i\omega\tau_\alpha)^\beta)^\gamma} \tag{4.1}$$

where ε_∞ is the high frequency plateau, $\Delta\varepsilon$ is the dielectric strength, τ is the mean relaxation time, and γ and β are shape parameters. The *Debye*, α, and *ion* subscripts denote the relaxation the parameter is associated with, being the ion rearrangement process, structural relaxation, and ion hopping motion, respectively.

4.4 Results and Discussion

Figure 4.1 shows the thermograms obtained for compositions ranging from 0-50mol% ChCl in EG. These data were collected to examine the phase behavior of DESs at a wide range of compositions and temperatures to obtain an accurate phase diagram for ChCl/EG mixtures. Figure 4.2 highlights the thermograms obtained for 0, 5, 20, and 33mol% ChCl to use in discussion of interesting phase behavior. Moreover, Figure 4.2d demonstrates that EG exhibits a single melting event upon heating, as expected for single component systems. A corresponding crystallization event is not observed. As ChCl is introduced, several additional crystallization and melting events emerge, as shown in Figures 4.2b-c for 20 and 5 mol% ChCl. For 33 mol% in Figure 4.2a, only a single broad crystallization feature is observed, followed by a broad melting feature. It is worth noting that the broad melting point at the 33 mol% composition is an important and expected feature of eutectic mixtures.[153, 154] Typically, broad melting events in DSC are attributed to a distribution of solid structures undergoing melting over a range of temperatures, as opposed to the sharply defined feature for a pure, highly-ordered crystal lattice such as is observed in the pure EG scan.

The broad melting region for the 33 mol% ChCl is indicative of a dual-phase region in a binary phase diagram, where both solid and liquid phases are present in non-eutectic compositions for a range of isotherms. These are typically denoted with solidus and liquidus transitions, where the dual-phase region is demarcated from the all-solid mixture at low temperatures, and the all-liquid mixture at high temperatures, respectively. A wide dual-phase region is therefore to be expected for all non-eutectic compositions, with T_m temperatures indicating the temperature at which the solid mixture first begins to melt, and T_L the temperatures marking the final melting of all the solid (denoted in bold).[155]

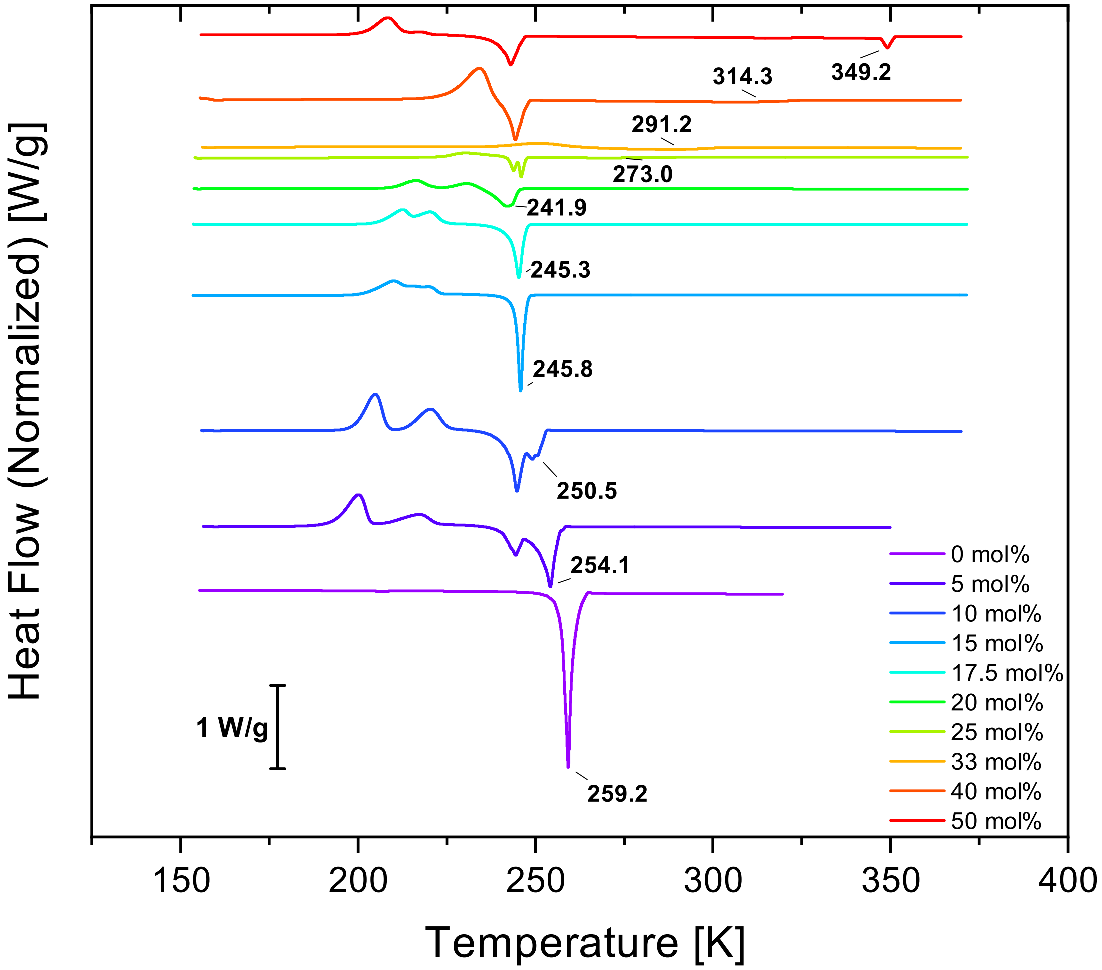

Figure 4.1: Normalized total heat flow obtained from modulated differential scanning calorimetry versus temperature for all compositions measured from 0-50mol% ChCl in EG. Data is arbitrarily stacked.

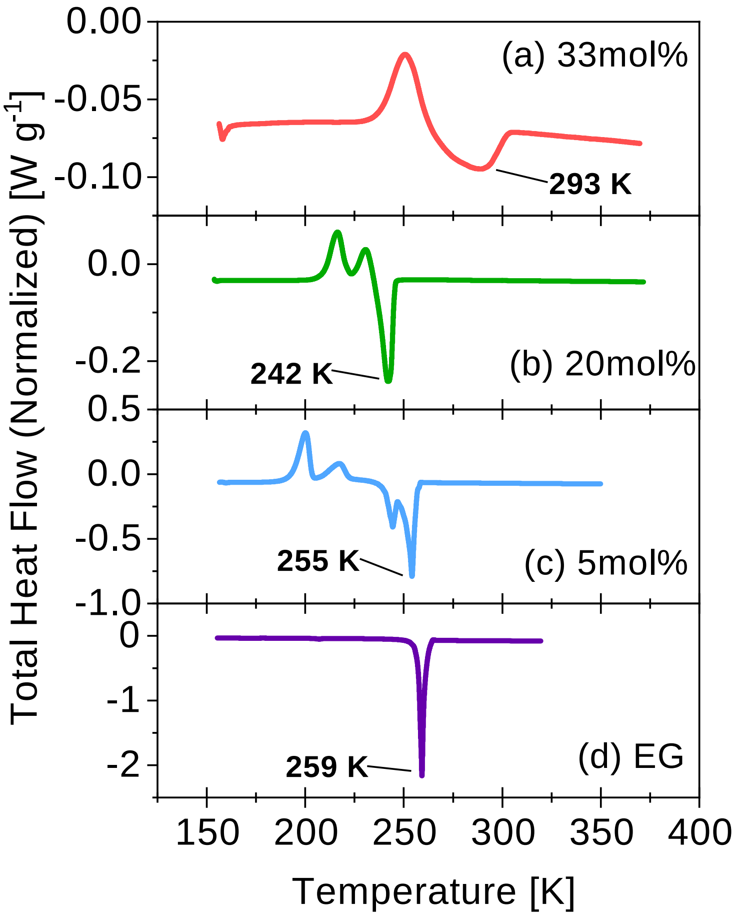

Figure 4.2: Normalized total heat flow obtained from modulated differential scanning calorimetry versus temperature for (a) 33, (b) 20, and (c) 5mol% ChCl in EG as well as (d) neat EG. In this work, the error bars are smaller than the size of the symbols, unless otherwise indicated. The T_Ls are denoted in the boldface font.

As compositions get closer to the eutectic composition, however, the solidus and liquidus temperatures converge into a single peak which is then called the eutectic point.[156] The 5 and 33 mol% compositions in Figure 4.2c and 4.2a demonstrate the former case as either multiple melting peaks, or as a wide, continuous trough - whereas the 20 mol% demonstrates the latter case, exhibiting only a single sharp melting event at the lowest observed temperature for any of the compositions, suggesting that 20 mol% is indeed the eutectic composition for the ChCl/EG mixture.

The primary focus of the current work is to evaluate correlations between the thermodynamic transitions and dynamics in DESs. For many electrochemical energy conversion and storage applications, a lowered melting point at the eutectic point – corresponding to an increased ionic conductivity, ion mobility, and overall faster solvent dynamics – would be beneficial. Here, we probe solvent dynamics using transient-absorption spectroscopy with femtosecond time resolution (fs-TAS). Since ChCl/EG mixtures do not absorb visible-light wavelengths, a well-established probe for solvent relaxation dynamics, Reichhardt's dye B30 is used in this study.[157] B30 has been used for solvent studies in many prior solvent systems[157, 158] and as probe molecule recently also for deep eutectic solvents.[159]

For protic solvents such as ChCl/EG mixtures, the normalized absorbance from fs-TAS measurements generally decays with two main components, which can be fitted with a biexponential function. Figure 4.3 shows data from two experiments performed with Reichardt's dye B30. The first, shown in Figure 4.3a, displays the steady-state absorption of B30, and is used as a measure of solvent polarity on a broadly accepted solvent scale of ET30 values. It indicates that the solvent polarity of ChCl/EG mixtures increases with ChCl addition as shown in the inset. Figure 4.3b shows the relaxation dynamics measured as the transient absorption dynamics of B30 as a function of time for compositions 0-33mol%. Figure 4.3c highlights the curves for 5, 16.67, and 33.33 mol% of ChCl in EG from 4.3b for discussion. The spectra reveal two distinct time components, which both show that solvation dynamics are enhanced with composition up to 16.67mol% ChCl, but are slowed down after this point as the composition approaches 33mol% ChCl. While there may be multiple processes taking place in solubilizing photoexcited B30, the literature on

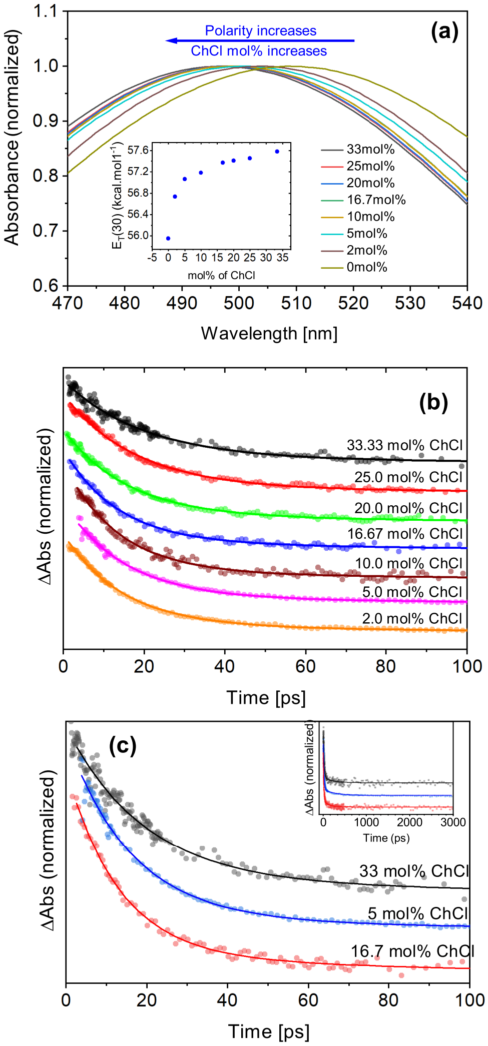

Figure 4.3: (a) Steady-state absorption spectra of the solvatochromic dye B30 in ethaline at various choline chloride (ChCl) concentrations from 0.0 to 33.33 mol% ChCl measured at 298K. The continuous blue-shift of λ_{max}(B30) with increasing ChCl mol%, shows increasing polarity at higher mol% of ChCl. Inset: The $E_T(30)$-polarity of ethaline solutions are calculated based on their λ_{max} values as summarized in Table 4.1. $E_T(30)$-polarity increases with increasing the mol%. (b)Normalized relaxation dynamics obtained for all compositions measured from 2.0-33.3mol% ChCl in EG. The curves are arbitrarily stacked for improved clarity. (c) fs-transient absorption kinetics of B30 measured at $\lambda_{probe} = 580$ nm at 298K and biexponential fits at 3 different mol% of ChCl in EG. Data sets are normalized and vertically offset for direct visual comparison. Other compositions (2, 10, 20, 25 mol%) are omitted for clarity; see SI for remaining kinetics. Inset: shows the kinetics up to 3 ns.

Table 4.1: Absorption wavelength maxima of B30 and $E_T(30)$, and E_T^N polarities for various ChCl/EG mixtures.

[ChCl]:[EG]	mol% of ChCl	λ_{max} $[nm]$	$E_T(30)$ $[kcal/mol]$	E_N^T
1:2	33.33	19.1 ± 0.6	235.5 ± 6.1	40
1:3	25	17.4 ± 0.1	195.9 ± 5.3	35.2
1:4	20	15.6 ± 0.1	129.4 ± 5.1	26.8
1:5	16.67	12.8 ± 0.1	108.2 ± 3.2	24.8
1:9	10	13.7 ± 0.1	128.5 ± 10.2	27.9
1:19	5	17.4 ± 0.1	152.1 ± 2.6	34.2
1:49	2	21.7 ± 0.7	166.8 ± 5.3	40

Table 4.2: Kinetic fit parameters for B30 in various ChCl/EG mixtures obtained using a global fit at λ_{probe} = 550-600 nm.

[ChCl]:[EG]	mol% of ChCl	τ_1 [ps]	τ_2 [ps])	τ_{avg} [ps])
1:2	33.33	19.1 ± 0.6	235.5 ± 6.1	40
1:3	25	17.4 ± 0.1	195.9 ± 5.3	35.2
1:4	20	15.6 ± 0.1	129.4 ± 5.1	26.8
1:5	16.67	12.8 ± 0.1	108.2 ± 3.2	24.8
1:9	10	13.7 ± 0.1	128.5 ± 10.2	27.9
1:19	5	17.4 ± 0.1	152.1 ± 2.6	34.2
1:49	2	21.7 ± 0.7	166.8 ± 5.3	40

femtosecond dynamics of B30 solvation generally attributes the initial fast component to the solvent reorientation while the slower component is assigned to the rearrangement of the hydrogen bonding network.[160, 161] Our previous studies indicate that the slow component is consistently absent in non-protic solvents.[162] Additional fs-TAS results for a series of ChCl/EG mixtures investigated are shown in Table 4.2, clearly highlighting the change in the solvation dynamics at the eutectic range at which both time constants are the fastest.

Broadband dielectric spectroscopy was employed to study reorientational and ion dynamics in each composition of ChCl in EG. Figure 4.4 shows the (a) real part of the complex dielectric function as well as (b) the dielectric loss obtained from the derivative representation employed to suppress the dc ionic conductivity and reveal any underlying relaxations in the spectra of 20mol% ChCl in EG at various temperatures. The spectra were fit with a linear combination of a Debye model, a Havriliak-Negami function, and a Random Barrier Model (RBM) to account for ion rearrangements, the structural relaxation, and ion hopping, respectively. These processes were observed for all compositions investigated, as previously reported.[152] In our previous study of ChCl/glycerol mixtures, we assigned the slow, Debye-like process to the rotational dynamics of choline ions that are inhibited by the hydrogen-bonded network of the hydrogen bond donor (HBD).

According to Debye's theory, relaxation of an isolated dipole can be described by an exponential function in the time domain, which yields symmetric dielectric relaxation spectra in the frequency domain.[127] Spatial and temporal inhomogeneities in a material lead to non-exponential functions which can, in principle, be decomposed into superpositions of single exponential (Debye-like modes) functions.[163] The more heterogeneous the dynamics, the broader the distribution of local relaxation times. To evaluate the dependence of the spectral shapes on composition, the dielectric loss normalized by the peak maximum is plotted versus radial frequency, normalized by the primary structural relaxation rate for each composition was analyzed, as shown in Figure 4.4c. It is observed that as ChCl concentration increases, the relaxation attributed to ion rearrangements speeds up and becomes more intense relative to the structural relaxation. Additionally, the spectral shapes become broader, suggesting that the mixtures are becoming more heterogeneous. This is consistent with a previous study

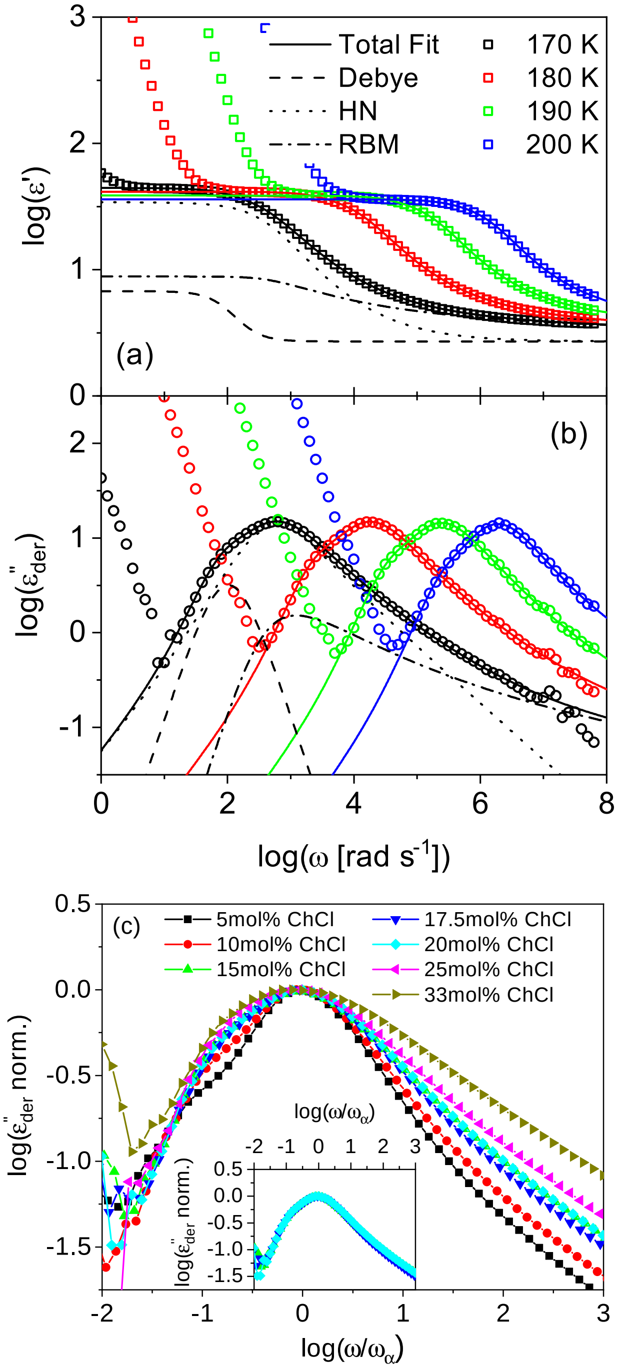

Figure 4.4: (a) The real part of the complex dielectric function of 20mol% ChCl in EG at various temperatures. (b) The derivative representation of the dielectric loss for various temperatures. The solid lines are total fits, dashed lines represent the Debye function, dotted lines denote the Havriliak-Negami (HN) function, and dash-dot lines are obtained from the random barrier model (RBM), as indicated. (c) The dielectric loss obtained from the derivative representation normalized by the value at the peak of the α-relaxation plotted versus radial frequency normalized by the mean rate of the α-relaxation for each composition at 170 K. Inset: Compositions of 15, 17.5, and 20mol% ChCl isolated to show their similarity.

Table 4.3: Fitting parameters for BDS data of 5mol% ChCl in EG using a Debye, Havriliak-Negami function, and Random Barrier Model.

T $[K]$	$\Delta\varepsilon_{\infty}$	$\Delta\varepsilon_{Debye}$	τ_{Debye}	$\Delta\varepsilon_{\alpha}$	τ_{α}	β	γ	σ_0 $[S/cm]$	τ_{ion} $[s]$
165	2.50	4.44	2.37E-01	45.5	2.40E-02	0.88	0.78	1.58E-11	6.64E-02
170	2.47	4.60	2.96E-02	43.6	2.86E-03	0.90	0.79	1.16E-10	9.01E-03
175	2.43	4.55	4.86E-03	41.6	4.63E-04	0.91	0.80	6.71E-10	1.58E-03
180	2.38	4.40	9.78E-04	39.5	9.42E-05	0.92	0.80	3.17E-09	3.43E-04
185	2.36	4.09	2.37E-04	36.3	2.31E-05	0.93	0.81	1.23E-08	8.83E-05

Table 4.4: Fitting parameters for BDS data of 10mol% ChCl in EG using a Debye, Havriliak-Negami function, and Random Barrier Model.

T $[K]$	$\Delta\varepsilon_{\infty}$	$\Delta\varepsilon_{Debye}$	τ_{Debye}	$\Delta\varepsilon_{\alpha}$	τ_{α}	β	γ	σ_0 $[S/cm]$	τ_{ion} $[s]$
165	2.69	6.13	1.12E-01	47.2	1.91E-02	0.88	0.73	3.84E-11	2.56E-02
170	2.47	5.60	1.49E-02	45.1	2.21E-03	0.87	0.78	2.83E-10	4.16E-03
175	2.45	5.56	2.47E-03	43.1	3.63E-04	0.88	0.79	1.63E-09	7.21E-04
180	2.43	5.43	5.06E-04	41.2	7.53E-05	0.90	0.79	7.72E-09	1.51E-04
185	2.55	5.22	1.24E-04	39.9	1.91E-05	0.91	0.79	3.08E-08	3.43E-05
190	2.61	4.75	3.52E-05	38.0	5.53E-06	0.91	0.81	1.04E-07	9.76E-06
195	2.09	3.37	1.45E-05	23.7	1.74E-06	0.91	0.82	2.11E-07	6.45E-06

Table 4.5: Fitting parameters for BDS data of 15mol% ChCl in EG using a Debye, Havriliak-Negami function, and Random Barrier Model.

T $[K]$	$\Delta\varepsilon_{\infty}$	$\Delta\varepsilon_{Debye}$	τ_{Debye}	$\Delta\varepsilon_{\alpha}$	τ_{α}	β	γ	σ_0 $[S/cm]$	τ_{ion} $[s]$
170	2.71	4.11	1.05E-02	31.1	2.35E-03	0.82	0.72	3.36E-10	3.20E-03
175	2.68	3.77	1.73E-03	30.0	3.60E-04	0.83	0.75	2.00E-09	5.36E-04
180	2.68	3.66	3.50E-04	28.8	7.20E-05	0.84	0.76	9.67E-09	1.09E-04
185	2.86	3.50	8.55E-05	28.2	1.81E-05	0.86	0.75	3.90E-08	2.30E-05
190	2.90	3.24	2.38E-05	27.1	5.17E-06	0.86	0.77	1.35E-07	6.52E-06
195	2.91	3.42	7.92E-06	25.5	1.72E-06	0.88	0.76	4.13E-07	2.12E-06

Table 4.6: Fitting parameters for BDS data of 17.5mol% ChCl in EG using a Debye, Havriliak-Negami function, and Random Barrier Model.

T $[K]$	$\Delta\varepsilon_\infty$	$\Delta\varepsilon_{Debye}$	τ_{Debye}	$\Delta\varepsilon_\alpha$	τ_α	β	γ	σ_0 $[S/cm]$	τ_{ion} $[s]$
165	2.67	4.87	7.35E-02	35.4	1.73E-02	0.84	0.71	5.17E-11	2.26E-02
170	2.67	4.40	9.69E-03	34.9	2.01E-03	0.84	0.74	3.89E-10	2.92E-03
175	2.66	4.37	1.65E-03	33.4	3.24E-04	0.85	0.75	2.25E-09	4.96E-04
180	2.65	4.16	3.40E-04	32.1	6.66E-05	0.86	0.77	1.07E-08	1.04E-04
185	2.80	3.94	8.40E-05	31.3	1.69E-05	0.87	0.77	4.26E-08	2.29E-05
190	2.77	3.68	2.37E-05	29.9	4.86E-06	0.87	0.79	1.46E-07	6.86E-06
195	2.03	3.12	9.53E-06	26.0	1.52E-06	0.86	0.87	4.23E-07	3.64E-06

Table 4.7: Fitting parameters for BDS data of 20mol% ChCl in EG using a Debye, Havriliak-Negami function, and Random Barrier Model.

T $[K]$	$\Delta\varepsilon_\infty$	$\Delta\varepsilon_{Debye}$	τ_{Debye}	$\Delta\varepsilon_\alpha$	τ_α	β	γ	σ_0 $[S/cm]$	τ_{ion} $[s]$
165	2.70	4.32	7.69E-02	32.3	2.00E-02	0.82	0.69	4.73E-11	2.37E-02
170	2.70	4.05	9.73E-03	31.5	2.21E-03	0.82	0.72	3.60E-10	3.01E-03
175	2.71	4.00	1.61E-03	30.3	3.47E-04	0.84	0.74	2.11E-09	4.95E-04
180	2.71	3.78	3.33E-04	29.1	7.01E-05	0.85	0.75	1.01E-08	1.02E-04
185	2.94	3.65	8.14E-05	28.7	1.78E-05	0.86	0.74	4.05E-08	2.06E-05
190	3.09	3.50	2.27E-05	27.8	5.13E-06	0.87	0.75	1.40E-07	5.33E-06
195	2.71	3.52	7.49E-06	25.3	1.66E-06	0.88	0.78	4.28E-07	2.37E-06
200	2.27	2.74	2.94E-06	23.7	6.32E-07	0.88	0.80	1.18E-06	1.09E-06
205	2.70	1.00	1.57E-06	25.2	2.73E-07	0.82	0.86	2.79E-06	3.50E-07

Table 4.8: Fitting parameters for BDS data of 25mol% ChCl in EG using a Debye, Havriliak-Negami function, and Random Barrier Model.

T $[K]$	$\Delta\varepsilon_\infty$	$\Delta\varepsilon_{Debye}$	τ_{Debye}	$\Delta\varepsilon_\alpha$	τ_α	β	γ	σ_0 $[S/cm]$	τ_{ion} $[s]$
170	2.70	3.53	1.28E-02	26.1	3.47E-03	0.79	0.70	2.58E-10	3.85E-03
175	2.64	3.30	1.90E-03	25.0	4.70E-04	0.80	0.73	1.59E-09	6.41E-04
180	2.60	3.24	3.73E-04	23.8	8.94E-05	0.81	0.74	7.85E-09	1.31E-04
185	2.74	2.99	8.92E-05	23.5	2.19E-05	0.83	0.74	3.23E-08	2.74E-05
190	2.91	2.90	2.43E-05	23.0	6.19E-06	0.84	0.74	1.13E-07	6.70E-06
195	3.08	2.71	8.29E-06	22.6	2.06E-06	0.86	0.72	3.52E-07	1.76E-06
200	3.74	2.18	2.98E-06	23.9	7.62E-07	0.87	0.70	9.84E-07	1.92E-07
205	3.23	2.13	9.84E-07	22.1	3.09E-07	0.86	0.72	2.50E-06	1.62E-07
210	4.35	3.82	2.98E-07	17.5	8.28E-08	0.83	1.00	5.64E-06	7.77E-08

Table 4.9: Fitting parameters for BDS data of 33mol% ChCl in EG using a Debye, Havriliak-Negami function, and Random Barrier Model.

T $[K]$	$\Delta\varepsilon_\infty$	$\Delta\varepsilon_{Debye}$	τ_{Debye}	$\Delta\varepsilon_\alpha$	τ_α	β	γ	σ_0 $[S/cm]$	τ_{ion} $[s]$
165	2.96	1.41	2.82E-01	26.3	1.46E-01	0.76	0.55	1.76E-11	5.94E-02
170	3.12	2.40	2.35E-02	25.2	9.11E-03	0.74	0.61	1.55E-10	5.24E-03
175	3.10	2.70	3.03E-03	23.7	9.85E-04	0.73	0.67	1.00E-09	8.25E-04
180	3.15	2.56	5.45E-04	22.8	1.64E-04	0.73	0.70	5.14E-09	1.53E-04
185	3.30	2.60	1.26E-04	22.1	3.61E-05	0.76	0.69	2.18E-08	3.00E-05
190	3.45	2.56	3.29E-05	21.5	9.41E-06	0.78	0.70	7.84E-08	7.04E-06
195	3.50	2.61	1.07E-05	20.4	2.91E-06	0.80	0.70	2.49E-07	2.16E-06
200	3.60	2.00	4.09E-06	20.5	1.10E-06	0.82	0.69	7.10E-07	6.44E-07

of 33mol% ChCl in EG, which confirmed the presence of dynamic heterogeneities.[97] The similarity of the spectral shapes for the 15, 17.5, and 20mol% compositions shown in the inset of Figure 4.4c is striking, as it suggests that their dynamic environments are comparable. The fitting parameters for each composition are given in Tables 4.3-4.9.

In Figure 4.5, the key parameters characterizing dynamics and ion transport as well as the relevant thermodynamic transitions are plotted as functions of the composition of the ChCl/EG mixtures. Contrary to the common assumption that the eutectic composition is at 33mol% ChCl or a 1:2 molar ratio of ChCl to EG, it is evident that the composition with the lowest melting temperature is in the 15-20mol% ChCl range. This result agrees with the solid-liquid equilibrium phase diagrams reported by Crespo *et al.* and Agieienko *et al.*, which also show that the lowest T_m occurs in this range for ChCl/EG mixtures.[164, 151] Tellingly, the structural relaxation rates from BDS at 170 K, plotted in Figure 4.5a, also show that the fastest dynamics occur in the 15-20mol% ChCl range, consistent with the fs-TAS results in Figure 4.5b. To our knowledge, this correlation between the eutectic composition and dynamics has not been previously reported. It is remarkable that the trend also holds for the other dielectric relaxations described earlier (Tables 4.3-4.9).

The time constants from fs-TAS shown in Figure 4.5b indicate that the relaxation dynamics first speed up with increasing mol% of ChCl up to 16.67 mol% and then become slower as ChCl mol% composition continues to increase up to 33mol%. This trend reveals a correlation between solvation dynamics and the thermodynamic transitions with the fastest dynamics at the eutectic composition. Consistent with the trends in the dynamics, Figure 4.5c shows that the dc ionic conductivity at 300 K and 170 K are also enhanced in the 15-20mol% ChCl range. The similarity of the dielectric spectral shapes in this concentration range shown in the inset of Figure 4.4c implies that the eutectic composition could also be regarded as a range, rather than a single value. However, further DESs should be studied before a general conclusion can be made regarding this point. In any case, these results agree with the recent experimental and computational work by Zhang *et al.*, also reporting a peak in the ionic conductivity at 20mol% ChCl.[107] Although Zhang *et al.* attributed this

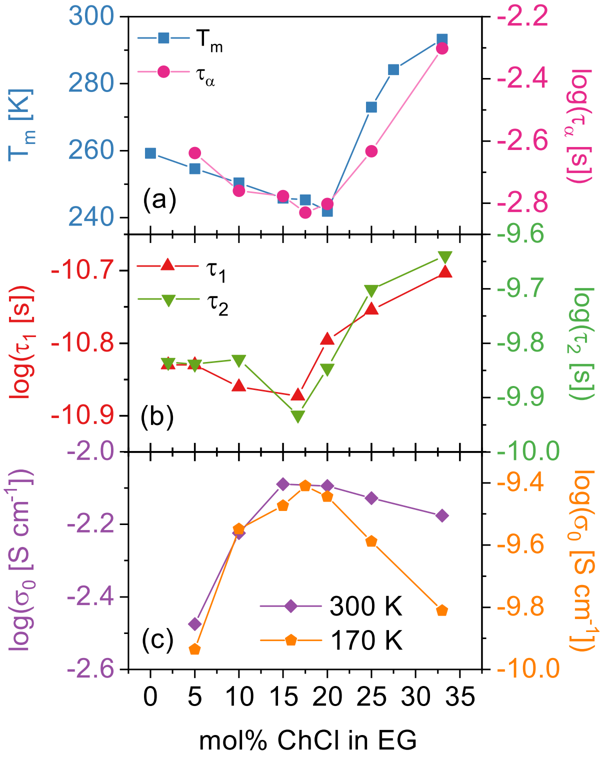

Figure 4.5: (a) Liquidus temperatures (blue squares) and structural relaxation rates from BDS at 170 K (pink circles) plotted versus mol% ChCl. (b) Relaxation time constants for the fast component τ_1 (red up triangles) and slow component τ_2 (green down triangles) from fs-TA kinetics of B30 in ethaline at room temperature plotted versus mol% ChCl. (c) DC ionic conductivities plotted versus mol% ChCl at 300 K (purple diamonds) and 170 K (orange pentagons). All three experimental quantities (panels a,b,c) align with the recent report that eutectic properties are found at a 1:4.85 molar ratio.

observation to a balance between concentration and viscosity effects, the picture emerging in the current work implies that the ionic conductivity is simply exhibiting a similar trend in the primary structural and ion dynamics.

Taken altogether, the current results suggest that the eutectic composition occurs in the 15-20mol% ChCl range. The T_L of 33mol% ChCl in EG (previously reported eutectic composition) occurs at 293 K, which agrees with the first report by Abbott *et al.*[148] For simple liquids, the Lindemann's criterion predicts a linear relationship between the glass transition (T_g) and melting temperatures.[23] Given that the T_g is a surrogate for the primary structural relaxation, the enhancement of dynamics at the eutectic composition is easily understood. We now need to rationalize the apparent discrepancy between the reported zero-shear viscosity and the dynamics presented in the current work. In a report by Zhang et al., the zero-shear viscosity does not exhibit a similar trend with concentration of the ChCl at the eutectic composition reported here.[107] Instead, the viscosity of ChCl/EG increases with increasing ChCl composition up to 33 mol%. This trend is not yet understood, but we conjecture that there exist slower mechanical relaxation modes beyond the primary structural dynamics that contribute to the overall viscosity of these mixtures. Indeed, the broadening of the dielectric spectra with increasing ChCl concentration observed in Figure 4.4, as well as the evidence of heterogeneities recently reported by Spittle *et al.* support this conjecture.[152] Overall, the data presented herein instead indicate that the 15-20mol% ChCl composition range offers the best opportunities for faster orientational and solvation dynamics, in addition to improving the dc ionic conductivity. As such, these compositions should be relevant for applications requiring DESs to serve as media for solvation and transport.

In conclusion, DSC, BDS, and fs-TAS, are employed to investigate the impact of thermodynamic transitions on dynamics in choline chloride ethylene glycol mixture across a wide range of compositions. It is shown that the eutectic composition range of the DES occurs at 15-20 mol% ChCl in EG, which correlates strongly with enhancement in both the primary structural relaxation, solvation dynamics, and increases in the dc ionic conductivity. This result is described within the framework of established glass transition models, and highlights the potential relevance of understanding the phase characteristics of DESs.

Chapter 5

Evolution of microscopic heterogeneity and dynamics in choline chloride-based deep eutectic solvents

The importance of understanding the DESs at a fundamental level has been established. In the previous chapter, it was shown that in Ethaline, the eutectic composition corresponds to faster dynamics and increased ionic conductivity. Still, it is unclear what impact the local structure and dynamics have on the properties. In this chapter, we examine two popular DESs - Ethaline and Glyceline - across multiple time- and length-scales using a wide array of experimental and computational techniques. This allowed a uniform picture to be put together about what microscopic dynamics and interactions contribute to the macroscopic properties we observe in these DESs. The BDS, DSC, and DMS experiments were performed by the Sangoro group. The CMD and AIMD simulations were performed by the Edward Maginn group at University of Notre Dame and the Mark Tuckerman group at New York University respectively. The ^{1}H NMR spectroscopy experiments were performed by the Thomas Zawodzinski group at University of Tennessee. The PFG-NMR experiments were performed by the the Steve Greenbaum group at Hunter College. The fs-TAS experiments were performed by the Clemens Burda group at CWRU. The density, viscosity, and ionic conductivity measurements were done by the Burcu Gurkan group at CWRU. The wide-angle neutron scattering (WANS) experiments were performed by the Mark Dadmun group at University of Tennessee. The QENS experiments were performed by Madhusdan Tyagi at the NIST Center for Neutron Research. The coordination, overall analysis, and writing of this project was directed by the Sangoro and Maginn groups to show a full picture and therefore all data collected is included in this chapter. This chapter is a reprinting of a previously published article and its supporting material. Changes from the originally published version are including supplementary material in the main text. My contributions to this article include the Sangoro group experiments and their data analysis, the interpretation of results from all techniques, and writing. Reprinted with permission from (Stephanie Spittle, Derrick Poe, Brian Doherty, Charles Kolodziej, Luke Heroux, Md Ashraful Haque, Henry Squire, Tyler Cosby, Yong Zhang, Carla Fraenza, Sahana Bhattacharyya, Madhusudan Tyagi, Jing Peng, Ramez A Elgammal, Thomas Zawodzinski, Mark Tuckerman, Steve Greenbaum, Burcu Gurkan, Mark Dadmun, Edward J Maginn, and Joshua Sangoro. Evolution of microscopic heterogeneity and dynamics in choline chloride-based deep eutectic solvents. *Nature Communications*, 13(1), 2022.). Copyright (2022) Springer Nature Limited.

5.1 Abstract

Deep eutectic solvents (DESs) are an emerging class of non-aqueous solvents that are potentially scalable, easy to prepare and functionalize for many applications ranging from biomass processing to energy storage technologies. Predictive understanding of the fundamental correlations between local structure and macroscopic properties is needed to exploit the large design space and tunability of DESs for specific applications. Here, we employ a range of computational and experimental techniques that span length-scales from molecular to macroscopic and timescales from picoseconds to seconds to study the evolution of structure and dynamics in model DESs, namely Glyceline and Ethaline, starting from the parent compounds. We show that systematic addition of choline chloride leads to microscopic heterogeneities that alter the primary structural relaxation in glycerol and ethylene glycol

and result in new dynamic modes that are strongly correlated to the macroscopic properties of the DES formed.

5.2 Introduction

Deep eutectic solvents (DESs) are an emerging class of materials with exceptional properties that make them promising for applications in solar cells, [165] redox flow batteries,[142, 101, 166] thermoelectric energy conversion,[167] supercapacitors,[168] chemical sensors,[169] chemical separation processes,[170] drug solubility,[139] and environmentally benign solvents for chemical synthesis and biomass processing.[171, 79] DESs are mixtures of two or more species, typically a hydrogen bond donor (HBD) species and a hydrogen bond acceptor (HBA) species, that results in a depressed melting temperature significantly below those of the parent compounds.[76, 80, 172, 109] The name deep eutectic solvent was first coined for this new class of solvents by Abbott *et al.* in 2004.[144] DESs are often considered a subclass of ionic liquids because of their similar properties such as low volatility, low flammability, and wide electrochemical and thermal stability windows.[102, 173, 150] In contrast to standard ionic liquids, these materials are often inexpensive to synthesize, and can usually be made from biodegradable, and nontoxic constituents.[117, 80] Although there are many possible combinations of HBAs and HBDs available to form DESs, predictive understanding of structure-property relationships necessary to design DESs for specific applications remains elusive. For instance, DESs exhibit relatively high viscosities, which limits their uses in many technologies, but there is no generally established approach to tune viscosities based entirely on the knowledge of the HBA and HBD chemistry. Although DES-related publications have now surpassed 3000, considerable work still needs to be done to unravel the fundamental relationships between the molecular structure and the macroscopic properties. Detailed fundamental studies of DESs have been largely limited to a few salt-based DESs usually at a single concentration. The depression in melting temperature is typically attributed to the complexation of the HBA, specifically the ions in salt-containing DESs, by the HBD through hydrogen bonding.[109, 144, 150] Hydrogen bonded networks (HBN) exist in pure HBDs, and these networks are characterized by unique local and supramolecular dynamics.[174, 175, 163] Moreover, in lithium salt and amide based DESs, Kaur *et al.* and Subba *et al.* confirmed the existence of spatial and temporal nanoscale heterogeneity, respectively, which likely results from segregated ionic and HBD domains.[110, 176] However, the evolution of such heterogeneities in DESs with composition as well as their resulting influence on macroscopic transport properties of DESs remain poorly understood.

Many key scientific questions remain unanswered. For instance, (i) how do the local structures and microscopic dynamics evolve with variation of composition of the mixtures approaching the eutectic concentration and (ii) how do spatial and temporal heterogeneities influence the macroscopic properties? To answer these questions, we start with canonical HBDs, namely glycerol and ethylene glycol (EG), and track the evolution of structure and dynamics as the HBA, choline chloride (ChCl), is added using a combination of experimental and computational techniques spanning length-scales from molecular to macroscopic as well as broad ranges of time-scales from picoseconds to seconds. Recent studies of Glyceline by pulsed field gradient nuclear magnetic resonance spectroscopy (PFG-NMR) revealed that the self diffusivity of choline is lower than glycerol.[7] However, when the same system is probed using quasi-elastic neutron scattering (QENS) over a shorter timescale, choline is found to diffuse faster than glycerol despite the larger size of choline.[177] These studies highlight the need to understand structure and dynamics across multiple time- and length-scales, thereby yielding comprehensive structural and dynamic information necessary to evaluate how microscopic properties, including interactions and local structures, affect the physicochemical properties observed at the macroscopic level.

We seek to understand how the systematic introduction of the HBA alters the structure and dynamics of HBD and dynamic environments of each component and unravel the underpinnings governing transport properties in DES. To do so, we start with well understood HBDs, glycerol and EG, and track the evolution of structure and dynamics as the HBA, ChCl, is added up to the eutectic composition (33mol% ChCl in glycerol and EG, namely Glyceline and Ethaline, respectively) using an array of complementary experimental and computational techniques capable of spanning lengthscales from molecular to macroscopic and timescales from sub-picoseconds to seconds and beyond. Techniques employed include PFG- and proton (^{1}H) NMR, *ab initio* (AIMD) and classical (CMD) molecular dynamics simulations, QENS and wide angle neutron scattering (WANS), broadband dielectric spectroscopy (BDS), dynamic mechanical spectroscopy (DMS), femtosecond transient absorption (fs-TA) spectroscopy, and differential scanning calorimetry (DSC). A combination of these methods provides access to a wealth of microscopic information across multiple time- and length-scales.

Using ^{1}H NMR, WANS, CMD, and AIMD simulations, we observe that as the concentration of ChCl is increased, the chloride ions increasingly interact with glycerol molecules, thereby altering the HBN and weakening the self-interactions of glycerol moieties. In addition, DMS reveals that the HBN of glycerol is substantially weakened but not completely destroyed. The dynamics of choline cations are investigated by QENS, PFG-NMR, and indirectly by BDS, and are shown to exhibit lower mobility than the glycerol molecules. However, as the concentration of ChCl increases towards the eutectic composition, we observe that the mobility of all constituent molecules increase, with choline dynamics becoming faster relative to the mean primary structural relaxation rates. These results together provide detailed insights into the observed increase in glass transition temperature depression, dc ionic conductivity, fluidity, and the mean rates of orientational dynamics as ChCl concentration is increased. These fundamental insights form a scientific basis for the understanding of the dominant correlations in structure-property relationships of DESs needed for rational design and tunable applications.

5.3 Materials and Methods

5.3.1 Sample Preparation for Protonated Samples

Glycerol and choline chloride were purchased from Sigma Aldrich at ≥99% and ≥98% purity respectively. Ethylene glycol was purchased from ACROS Organics at 99+% purity. Betaine-30 (Reichardt's dye, 90%, Sigma-Aldrich) was used as received for fs-TS measurements.

Glycerol was used as received. The DES preparation and characterization was performed following protocols reported by Gurkan *et al.*[145] ChCl was dried in a vacuum oven for 2 days at 393 K. Appropriate amounts of ChCl were added to glycerol, and stirred at 353 K in a dry nitrogen atmosphere until a clear liquid was formed. Samples prepared for ^{1}H NMR, BDS, DMS, fs-TA, and DSC were not prepared in a glove box, so they were briefly exposed to ambient conditions.

5.3.2 Proton and Pulsed-Field Gradient Nuclear Magnetic Resonance Spectroscopy

^{1}H NMR data were recorded on a Bruker Avance III spectrometer operating at 400 MHz using a direct 5-mm broadband probe. The sample temperature was established at 333 K with an equilibration period of 1 hour before data acquisition. The chemical shifts were referenced to trimethylsilane (TMS) as an external standard. ^{1}H NMR spectra were recorded with a standard one-pulse sequence with 90° flip angle, with a spectral width of 20 ppm, and a relaxation delay of 1 second.

NMR diffusion experiments were performed with a 400MHz Bruker spectrometer. PFG-NMR stimulated echo sequence was used to measure the self-diffusion coefficients of glycerol and choline independently (using their well-differentiated peaks in the NMR spectrum), at variable temperatures covering the 298-338 K range. The gradient strength, g, was varied linearly over 16 values ranging from 0-80 G-cm^{-1}. The gradient pulse duration was $\delta = 7 - 9\ ms$ and the diffusion delay was $\Delta = 0.5 - 1.2\ s$. The self-diffusion coefficients, D, were then extracted by fitting the decay echo signal with the Stejskal–Tanner equation: $I = I_0\, exp[-D\,(\gamma\, g\, \delta)^2(\Delta - \delta/3)]$, where I is the amplitude of the attenuated echo signal, I_0 is the initial intensity and γ is the proton gyromagnetic ratio.[178]

5.3.3 Classical Molecular Dynamics Simulations

Fully atomistic equilibrium molecular dynamics simulations were run using LAMMPS [179] with intra- and inter-molecular interactions described by the general AMBER force field

(GAFF).[180] Initial structures of individual glycerol and choline molecules were optimized in vacuum-phase using Gaussian 09 [181] using a B3LYP/aug-cc-pvdz basis set. Atomic Lennard-Jones (LJ) sigma and epsilon values were adapted from a study by Perkins *et al.*[182] Atomic charges were also adapted from the same study, though the atomic charges of choline and chloride were uniformly re-scaled from the given 0.9 to 0.7 net molecular charge. Charges of glycerol atoms were unmodified. The studies indicated that charge scaling higher than 0.7 did not correctly model ChCl glycerol mixture dynamics, resulting in systems that became slower with added choline chloride rather than faster. While a 0.7e scaling resulted in absolute bulk phase dynamics that were faster than experimental measurements, the correct physical trends were properly captured for the observed concentration and temperature range. The parameters used to describe ChCl and EG mixtures were detailed in our previous publication.[97] A 1 fs timestep, velocity Verlet integrator, periodic boundary conditions in all directions, cutoffs for LJ and Coulombic interactions of 12 Å, and a particle-particle particle-mesh long range solver at 10^{-4} accuracy were used for all simulations.

Initial conformations were randomly and loosely packed into a cube via Packmol.[183, 184] The composition of each simulation box is summarized in Table 5.1. Simulations for ChCl and glycerol mixtures were run at temperatures between 280 K and 400 K in 20 K increments for a total of seven temperatures. ChCl and EG mixtures were simulated at 298 K. Boxes were equilibrated for 2 ns in the isothermal isobaric (NPT) ensemble at one atmosphere and their respective temperatures until the density and total energy had converged for at least 1 ns. Box dimensions were taken from the average of the last 1 ns of the converged NPT run for initializing a canonical (NVT) ensemble production run. Production runs were carried out for 20 ns. A Nosé-Hoover-chain thermostat and Nosé-Hoover-chain barostat with a chain length of 3 and time constant of 100 fs were used where applicable in all simulations. Further production runs specifically for viscosity calculations were initialized from the equilibrated NVT configurations following the method detailed by Zhang *et al.* with viscosity calculated via a time decomposition method using the integral over time of

Table 5.1: Composition of simulation boxes.

ChCl mol%	Number of ChCl	Number of HBD	Number of total atoms
		glycerol	
0	0	715	10010
5	35	665	10080
10	68	612	10064
20	129	516	10062
33	200	400	10000
		ethylene glycol	
0	0	1000	10000
5	100	1900	21200
10	150	1350	16800
16.7	150	750	10800
20	175	700	10850
25	200	600	10400
33	250	500	10500

the pressure tensor autocorrelation function:[185]

$$\eta = \frac{V}{6k_BT} \int_0^\infty \sum_{\alpha\leq\beta} \langle \bar{P}_{\alpha\beta}(t) \cdot \bar{P}_{\alpha\beta}(0) \rangle \; \mathrm{d}t \tag{5.1}$$

In the above equation, V is the system volume, k_B is the Boltzmann constant, T is system temperature, and $\bar{P}_{\alpha\beta}$ is the modified pressure tensor of element $\alpha\beta$. To improve statistics, viscosities are averaged over the six correlation functions of the modified pressure tensors: $\bar{P}_{xy} = P_{xy}$, $\bar{P}_{yz} = P_{yz}$, $\bar{P}_{xz} = P_{zx}$, $\bar{P}_{xx} = 0.5(P_{xx} - P_{yy})$, $\bar{P}_{yy} = 0.5(P_{yy} - P_{zz})$, $\bar{P}_{zz} = 0.5(P_{xx} - P_{zz})$. $P_{\alpha\beta}$ are elements of the standard pressure tensor. Viscosity calculations were carried out using the PyLAT tool[186].

Site-site radial distribution functions (RDFs), coordination numbers (N_{coord}), combined distribution functions (CDFs), and hydrogen bond dynamics were calculated using the TRAVIS program.[187]. Self-diffusion coefficients were calculated using the Einstein expression in equation 5.2 and the MSD was calculated using equation 5.3.

$$D_S = \frac{1}{6N} \lim_{t\to\infty} \frac{\mathrm{d}}{\mathrm{d}t} \sum_{i=1}^{N} \langle [\mathbf{r}_i(t) - \mathbf{r}_i(0)]^2 \rangle \tag{5.2}$$

$$\langle [\mathbf{r}_i(t) - \mathbf{r}_i(0)]^2 \rangle \;\; = \frac{1}{n+1} \sum_{t_0=0}^{n} [\mathbf{r}_i(t_0 + t) - \mathbf{r}_i(t_0)]^2 \tag{5.3}$$

where N is the number of individual species and $\mathbf{r}_i$ is the center of mass position of the ith species. The dipole moment was defined for each molecule by calculating the positive and negative centers of charge, using only positive and negative atoms respectively, and drawing a vector between the two for each molecule. A dipole auto-correlation was calculated using the correlation function:

$$C(t) = \left\langle \frac{1}{2N_i} \sum_{i=1}^{N_i} [3\cos^2\theta_i(t) - 1] \right\rangle \tag{5.4}$$

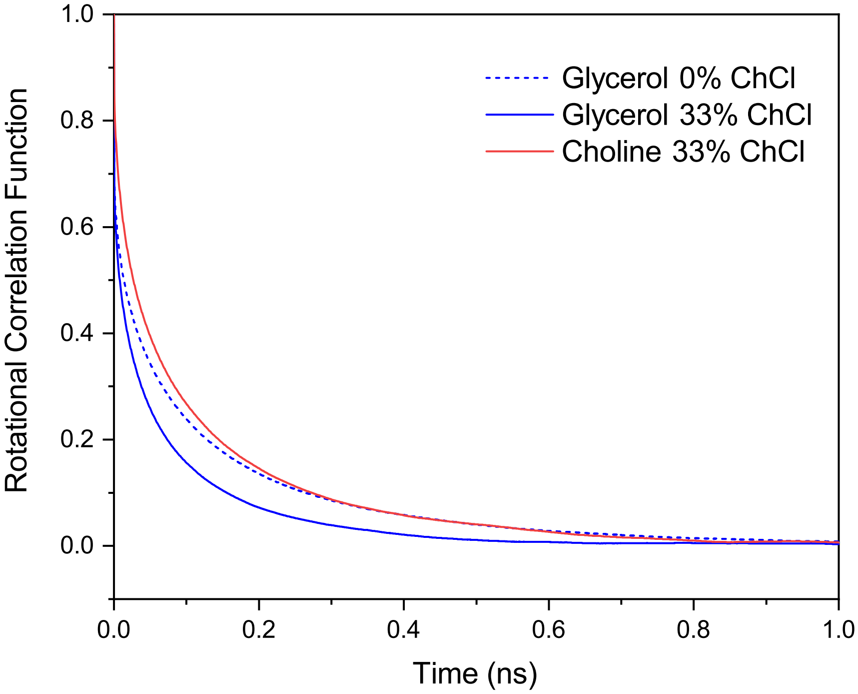

Figure 5.1: Normalized dipole moment rotational correlation function of glycerol and choline in Glyceline (solid) and pure glycerol (dashed) at 300K

where N_i is the number of such vectors, and $\theta_i(t)$ is the angle between each vector at time $t = 0$ and the same vector at time t. The decay behavior of the correlation functions with ChCl present exhibited both fast and slow modes not easily fit to a pure exponential function, possibly due to non-integer dynamics at fast time-scales. Examples of the correlation functions are shown in Supplementary Figure 5.1. To model this, the following functional form was used:

$$C(t) = b_1 E_{\alpha 1}(-(t/\tau_1)^{\alpha_1}) + b_2 E_{\alpha 2}(-(t/\tau_2)^{\alpha_2}) \tag{5.5}$$

where $z = t/\tau_n$ and $E_\alpha(z)$ is the Mittag-Leffler function:

$$E_\alpha(z) = \sum_{n=0}^{\infty} \frac{z^n}{\Gamma(\alpha + 1)} \tag{5.6}$$

also expressed as the Laplace transform:[188, 189]

$$E_\alpha(-z^\alpha) = \frac{1}{\pi} \int_0^\infty e^{-xz} \frac{x^{\alpha-1} \sin \pi\alpha}{x^{2\alpha} + 2x^\alpha \cos \pi\alpha + 1} dx, 0 < \alpha < 1 \tag{5.7}$$

where $b_n (b_1 + b_2 = 1)$, α_n, and τ_n, $n = 1, 2$, are fitting parameters, with τ_n capturing relevant time scales in the system, and $\Gamma(x)$ is the Gamma function. Note that a Mittag-Leffler function reduces to an exponential function when $\alpha = 1$. For non-integer values of α, $E_\alpha(z)$ behaves as a stretched exponential for small z, $E_\alpha(-(t/\tau)^\alpha) \approx \exp(-(t/\tau)^\alpha)/\Gamma(1 + \alpha)$, and then decays asymptotically according to a power law $(t/\tau)^{-\alpha}$.

Simulated neutron scattering structure factors, $S(q)$, were computed by:

$$S(q) = \frac{\rho_0 \sum_i \sum_j x_i x_j f_i f_j \int_0^{\frac{L}{2}} 4\pi r^2 (g_{ij}(r) - 1) \frac{sin(qr)}{qr} W(r) dr}{[\sum_i x_i f_i]^2} \tag{5.8}$$

where ρ_0 is the total count density, x_i and x_j are the mole fractions of atoms i and j, f_i and f_j are the tabulated neutron scattering form factors[190] of atoms i and j, L is the simulation box length, $g_{ij}(r)$ is the RDF between atoms i and j, and $W(r) = sin(2\pi r/L)/(2\pi r/L)$ is a Lorch window function to account for finite size truncation of the $g_{ij}(r)$ at large r.

5.3.4 *Ab Initio* Molecular Dynamics Simulations

Starting geometries for all AIMD simulations were prepared using CMD in the simulation package PINY_MD[191] with a previously developed force field for DES systems[192] in a canonical NVT ensemble for 10ns. Each DES system was constructed using the program Packmol[184]. For the Glyceline system, 16 choline chloride ion pairs were used along with 32 glycerol molecules. Cubic boxes were kept constant to reproduce extrapolated experimental densities at 400K.[193] In order to alleviate the high calculation costs of an AIMD simulation, multiple time stepping techniques (MTS) have previously been developed.[194, 195] Of these MTS methods, the reversible reference system propagator algorithm (r-RESPA)[196] was utilized. In this approach, the force of the system $F(\mathbf{R})$ is separated into an inexpensive reference-system force $F_{ref}(\mathbf{R})$, that serves as a crude approximation of $F(\mathbf{R})$, and a correction $F_{corr}(\mathbf{R})$ such that $F(\mathbf{R}) = F_{ref}(\mathbf{R}) + F_{corr}(\mathbf{R})$. Both $F_{ref}(\mathbf{R})$ and $F_{corr}(\mathbf{R})$ are treated with different time steps and levels of theory while retaining time reversibility and numerical stability. Recently, this approach has been successfully applied to liquid imidazole using a combination of density functional tight binding (DFTB)[197, 198] as a reference system and corrections derived from full density functional theory (DFT).[199] The success of this recent study shows that r-RESPA can be integrated into the AIMD framework and can be applied to DESs as well.[200]

AIMD simulations using r-RESPA were carried out using DFT and the 3rd order variant of the density functional tight binding method (DFTB3) within the CP2K package utilizing the QUICKSTEP module.[201] For the DFT correction, forces and energies of all atoms of the system were calculated using a hybrid Gaussian and planewave (GPW) approach with the molecular optimized triple- basis set (MOLOPT-TZVP-GTH)[202], along with the Perdew-Burke-Ernzerhof (PBE) functional and the corresponding Goedecker-Teter-Hutter (GTH) psuedopotentials.[203] A density cutoff of 520 Ry was used. The finest grid level was set with a multigrid number 4 and a relative cutoff of 60 using the smoothing for the electron density (NN10_SMOOTH) and its derivative (NN10).[201] To include dispersion, an empirical dispersion correction was included (D3).[204] To calculate $F_{ref}(\mathbf{R})$, DFTB3 was used in conjunction with the 3ob-3-1 parameters[205, 206] and the D3 dispersion correction. Trajectories were sampled using periodic boundary conditions and boxes were equilibrated for 10 ps with the canonical NVT ensemble at 400 K held using the Nosé-Hoover-chain thermostat.[207, 208] Production runs were carried out for an additional 25 ps. The DFTB3 reference system was integrated with a time step of 0.5 fs and the DFT corrections were applied every 2.0 fs. Radial distribution functions (RDFs) and combined distribution functions (CDFs) were calculated using the program TRAVIS.[187]

5.3.5 Wide-Angle and Quasi Elastic Neutron Scattering

Wide angle neutron scattering measurements (WANS) were collected at the Nanoscale Ordered Materials Diffractometer (NOMAD) at Oak Ridge National Laboratory over a diffraction range from 0.1 Å^{-1} up to 30 Å^{-1}. Choline chloride and glycerol mixtures of 1:2 (33% ChCl) and 1:20 (5% ChCl) were prepared using d-choline chloride (trimethyl-d9, 98%) and d-glycerol (d8, 99%), from Chemical Isotopes Laboratory in a glove box with $\leq$0.2ppm O_2 and sealed in 3mm quartz capillaries. Measurements were taken in 30-minute intervals and multiple sets of the same composition were summed together prior to reduction to improve statistics. $S(q)$ data were obtained by reduction of data using Addie.[209] Quartz capillary background scattering was subtracted from sample scattering. Glyceline data were then normalized to scattering from vanadium.

For the QENS experiment, four choline chloride and glycerol mixtures were prepared in a controlled atmosphere glove box. Two samples were prepared in the ratio of 1:9 (10% ChCl, 90% d-glycerol, and 10% d-ChCl, 90% glycerol) and the other two samples were mixed in the ratio of 1:2 (33% ChCl, 67% d-glycerol and 33% d-ChCl, 67% glycerol). Prior to mixing, ChCl was heated for two hours at 393 K. After the addition of the appropriate amount of glycerol with ChCl, the mixtures were kept at 353 K for an additional two hours for equilibration. Elastic fixed window scans (FWS) were completed on 10% and 33% ChCl samples using the High Flux Backscattering Spectrometer (HFBS) at the National Institute of Standards and Technology (NIST) Center for Neutron Research (NCNR).[210] The HFBS has an instrument resolution of ~0.8 μeV (about 2 ns) and elastic intensity was measured over the q range of 0.25 to 1.75 Å^{-1} in the temperature window from 4 to 298 K with a temperature ramp rate of 0.8 K/min. The elastic intensity was measured on heating and cooling to verify the reversibility of the dynamics and that the components did not crystallize during the process. The measurements were reduced and analyzed using DAVE, a data analysis and visualization software.[211]

5.3.6 Broadband Dielectric Spectroscopy

Broadband dielectric spectroscopy investigates the polarization response to an alternating electric field over a wide frequency and temperature range. This response may be given in terms of the real and imaginary parts of complex permittivity, $\varepsilon^*(\omega) = \varepsilon'(\omega) - i\varepsilon''(\omega)$, which can be directly related to complex conductivity as $\varepsilon^*(\omega) = i\omega\varepsilon_0\sigma^*(\omega)$, where ω is radial frequency and ε_0 is the permittivity of free space. The complex conductivity function can also be expressed in terms of the real and imaginary parts as $\sigma^*(\omega) = \sigma'(\omega) + i\sigma''(\omega)$. Since $\varepsilon''(\omega)$ is directly related to the real part of conductivity, $\sigma'(\omega)$, dielectric relaxations can become obscured in ion-conducting materials due to the dominant contributions of the dc ionic conductivity. Therefore, we instead examine the derivative representation, $\varepsilon''_{der} = -\pi/2(\partial\varepsilon^{'}/\partial\ln(\omega))$, to unveil any relaxations which may be overshadowed by contributions from the ionic conductivity.

A Novocontrol High Resolution Alpha Dielectric Analyzer in combination with a Quatro cryogenic temperature control system were used to perform the dielectric measurements from 10^{-1} to 10^{7} Hz from 150 K to 400 K, with accuracy better than $\pm 0.1K$. The samples were measured in parallel plate capacitor geometry with 20 mm diameter gold-plated brass electrodes. In addition, an Agilent E5071C Vector Network Analyzer was used for room temperature measurements from 3×10^5 to 2×10^{11} Hz. The dielectric data for glycerol in the high frequency regime were adequately fit using a single Havriliak-Negami function (Equation 3.33). However, the data for the ChCl/glycerol and ChCl/EG mixtures were fit using a combination of a Debye function, Havriliak-Negami function, and a Random Barrier

Model (Equation 4.1). The three functions for the mixtures were necessary to account for contributions from the slow, structural α, and ion dynamics, respectively.

5.3.7 Dynamic Mechanical Spectroscopy

Oscillatory-shear rheology measurements of 0, 5, 10, 20, and 33 mol% ChCl in glycerol were made using a TA Instruments Discovery Hybrid Rheometer-2. Parallel plate geometry was used with 8 mm for higher temperatures and 3 mm plates for measurements at temperatures approaching the glass transition. The dynamic mechanical spectra were obtained from 10^{-1} to 10^{2} Hz at temperatures ranging from 178 to 223 K. Time-temperature superposition was employed to obtain a master curve for each composition investigated. The data were fit using the linear addition of two Cole-Davidson modified Maxwell equations (Equation 3.9).[126] Viscosity measurements below 298 K were made on the TA Instruments Discovery Hybrid Rheometer-2 by applying a constant shear rate.

5.3.8 Femtosecond Transient Absorption Spectroscopy

The samples of glycerol and mixtures with ChCl were cooled from 353 K after mixing to 303 K, and transferred into sealed cuvettes to prevent moisture ingress. Femtosecond transient absorption spectroscopy was performed on a ClarkMXR CPA-2001 laser, outputting 780 nm fundamental wavelength, at a repetition rate of 1 kHz. This output beam was split, with 5% going to a sapphire crystal to create the supercontinuum probe beam, and the rest to a light conversion TOPAS to produce a 490 nm wavelength pump beam. Pump power was chosen as the lowest power that provided stable signal, which was 40 mJ cm^{-2}. Steady state UV-Vis measurements were performed using a Varian Cary 50 UV-Vis Spectrophotometer. Data were chirp-corrected and fit to biexponential decay functions, modeled by: $\Delta Abs = A_1 exp(\tau_1 t) + A_2 exp(\tau_2 t)$, where A_1 and A_2 are amplitude coefficients, t is time, and τ_1 and τ_2 are time constants.

It is worth pointing out that preferential solvation to betaine-30 probes has been observed in past experiments.[212, 213, 214] Indeed, apolar probes elicit hydrophobic solute-solvent interactions (Van der Waals type interactions), while polar groups lead to the possible induction of electronic polarizations, ionic interactions and also possible hydrogen bonding. The solvent systems studied here are of highly polar character, with dominant hydrogen-bonding characteristics. Thus, an apolar probe molecule might have led to different results and different relaxation components. This is why we have chosen betaine-30 as the probe molecule, which has a pronounced charge transfer character in its ground state. The charge transfer characteristic implies that the molecule is strongly surrounded by the HBD molecules of the DES, as well as the ionic species, as suggested above. Furthermore, the molecular simulations in this work suggest a strong hydrogen bonding network in the bulk solvent. The similarity in solvent-solvent interactions in the bulk and the solvent-solute interactions in the surrounding of the probe molecule explains the observed quantitative agreement in the mean rates of the dynamics obtained from fs-transient absorption measurements, broadband dielectric spectroscopy, and dynamic molecular simulation data.

5.3.9 Differential Scanning Calorimetry

A TA Instruments Q2000 Differential Scanning Calorimeter was used to determine the calorimetric glass transition temperatures. The measurements were obtained by cycling from 298 to 163 K and back up to 298 K twice at 10 K/min. No melting or crystallization was observed.

5.4 Results

We begin with investigation of the neat HBD species, glycerol, and then gradually increase the concentration of the HBA species, ChCl, up to the eutectic composition to observe the evolution of the structure and dynamics across multiple time- and length-scales.

5.4.1 Local Structure and Microscopic Interactions

The microscopic properties are examined first. The ^{1}H NMR spectra of the $0 - 33$ mol% ChCl/glycerol mixtures are shown in Figure 5.2. These were obtained at 333 K instead of room temperature to improve the spectral resolution. The proton from the hydroxyl group of choline, peak 'i', is only observed as a slight shoulder in 5mol% ChCl due to the low concentration of ChCl. The peak assignment is consistent with previously reported data.[120] The spectra show rather broad peak widths ranging from 6 to 51 Hz full width at half maximum (FWHM), which is consistent with the high viscosities of the samples (Table 5.2). In general, as the ChCl concentration increases, the peak width decreases with the exception of peak 'f', which may indicate more restricted motion of the methyl group on ChCl, and peak 'i' the OH group on ChCl due to exchange processes.

Interestingly, a pronounced difference in the chemical shift of the hydroxyl protons was observed, in particular for the hydroxyl protons, denoted by a, e, and i (Figure 5.2b and Table 5.3). This upfield shift suggests that as the concentration of ChCl is increased, the chloride anions interact with these protons, providing slight increases in electron density. The same trends are observed between neat EG and 33mol% ChCl in EG, shown in Figure 5.3. However, the shifts are more pronounced, suggesting that the interactions are stronger. The decrease in chemical shift of the ChCl OH proton as the concentration of ChCl increases also suggests that the intermolecular self hydrogen bonding decreases which contributes to the decrease in T_g. Chemical shift differences in this system may be primarily attributed to changes in the hydrogen bonding network, structural changes, and anisotropies, as has been seen in ionic liquids and other DESs.[215, 216]

To further monitor the evolution of the local structure with concentration of ChCl, we employ CMD and AIMD simulations to obtain the RDFs and coordination numbers ($\mathrm{N}_\mathrm{coord}$) associated with specific interactions. The CMD force field bulk behavior was first validated by comparing against experimental results. The computed density as a function of composition matched the absolute experimental values quite well, though the simulations predict a slightly greater composition dependence of the density than is observed

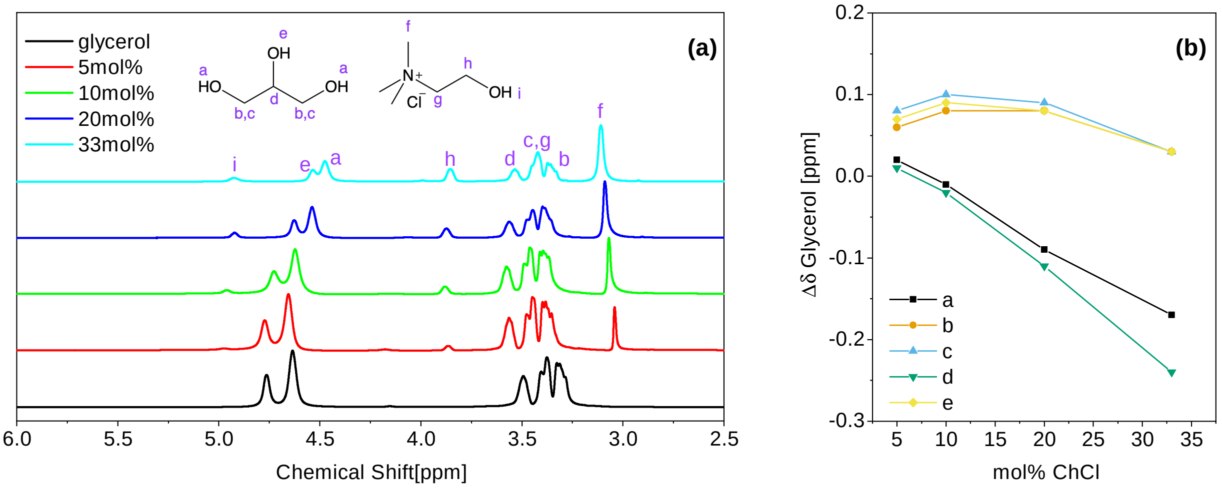

Figure 5.2: (a) ^{1}H NMR spectra of glycerol and mixtures of 5, 10, 20, and 33mol% ChCl in glycerol at 333 K. Purple letters a-f denote the various protons on glycerol (left chemical structure) and ChCl (right chemical structure). (b) Change in chemical shift in ppm with respect to neat glycerol as a function of ChCl concentration. Letters a-e denote the protons as specified in purple in part a.

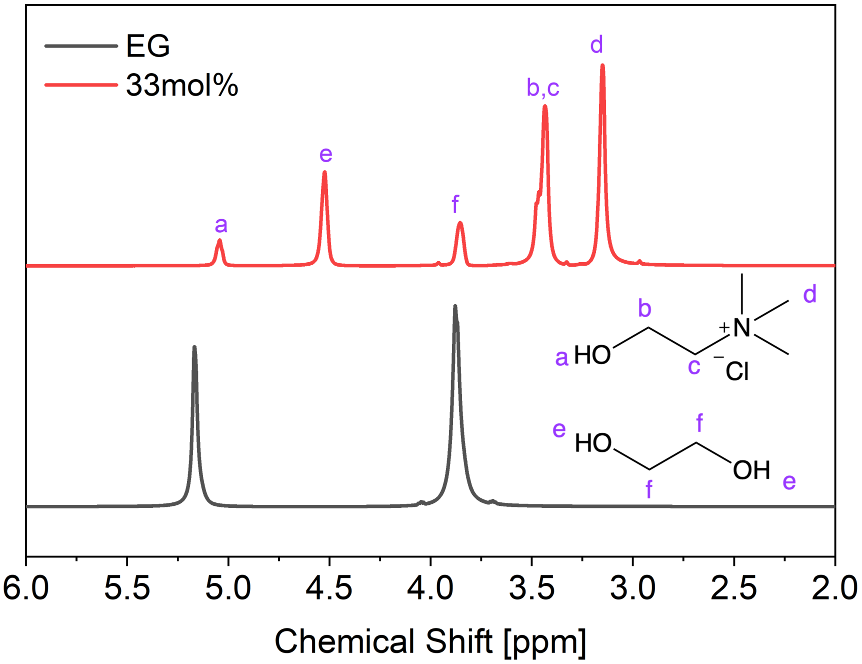

Figure 5.3: ^{1}H NMR spectra for 0 and 33mol% ChCl in ethylene glycol at 333 K.

Table 5.2: Peak widths in Hz at 333 K as a function of composition.

	a	b	c	d	e	f	g	h	i
Glycerol	15	22	24	17	14				
5 mol% ChCl	30	26	13	22	24	9	14	18	11
10 mol% ChCl	19	21	7	14	21	7	9	11	13
20 mol% ChCl	15	17	5	13	14	9	8	13	14
33 mol% ChCl	14	15	6	11	12	10	8	12	17

Table 5.3: ^{1}H chemical shifts in ppm at 333 K as a function of composition.

	a	b	c	d	e	f	g	h	i
Glycerol	4.63	3.31	3.39	3.49	4.75				
5 mol% ChCl	4.65	3.37	3.47	3.56	4.76	3.03	3.44	3.86	4.97
10 mol% ChCl	4.62	3.39	3.49	3.58	4.73	3.07	3.47	3.88	4.96
20 mol% ChCl	4.54	3.39	3.48	3.57	4.64	3.09	3.45	3.88	4.93
33 mol% ChCl	4.46	3.34	3.42	3.52	4.51	3.11	3.39	3.84	4.91

experimentally (Figure 5.4). Although the computed viscosity is lower than the experimental viscosity, the trend with composition is captured very well (Figure 5.5) and should yield reasonable predictions of composition-dependent dynamics. Figure 5.6a shows the ChCl and glycerol molecules, with examined atoms and interactions highlighted. Center and terminal hydrogen and oxygen atoms of glycerol are referred to as Hc, Ht, Oc, and Ot respectively. The hydroxyl group on choline is labeled Hy and Oy for the hydrogen and oxygen atoms respectively. Figure 5.6b shows the comparison of an overall RDF for the 33mol% ChCl system from AIMD and CMD, where peak shapes and positions are in excellent agreement with each other.

Partial RDFs are also provided (Figure 5.7), where pair-wise interactions with chloride are compared between AIMD and CMD. A small shift in the peak heights and distances is observed, however this result has been seen in a previous AIMD study for a 1:1 ratio of ChCl to glycerol by Korotkevich *et al.*,[217] and is likely due to the inclusion of polarization effects in the AIMD approach. Additionally, difference in peak heights can be due to many complicating factors such as system size, AIMD accounting for many-body terms, and the high sensitivity of RDFs to these influences. A more reliable measurement of local solvation structure is through $\mathrm{N}_{\mathrm{coord}}$. Integration of the RDF over the first solvation shell, defined as the first minimum after the first maximum in the RDF, provides $\mathrm{N}_{\mathrm{coord}}$ values that indicate the general local structuring. Table 5.4 summarizes the $\mathrm{N}_{\mathrm{coord}}$ corresponding to the local solvation environment with respect to the first atom in the site-site column. The results show a good agreement for $\mathrm{N}_{\mathrm{coord}}$ between CMD and AIMD. Local structuring was also compared with the calculated neutron scattering function $S(q)$ at 400 K for both AIMD and CMD and provided in Figure 5.8. The plots are nearly identical at this temperature, indicating that the force field is able to capture the relevant structural features.

Figure 5.6c provides an additional comparison of CDFs with an RDF on the x-axis and an angular distribution function (ADF) on the y-axis created from AIMD and CMD simulations at the eutectic composition, 33mol% ChCl in glycerol. Assessments of the HBN of DESs have been performed in the literature, where a maximum donor-acceptor distance has been set to either 3.0 Å [218] or 3.5 Å [182] with a minimum O-H-X angle of 150°[182] or 130°.[218] The

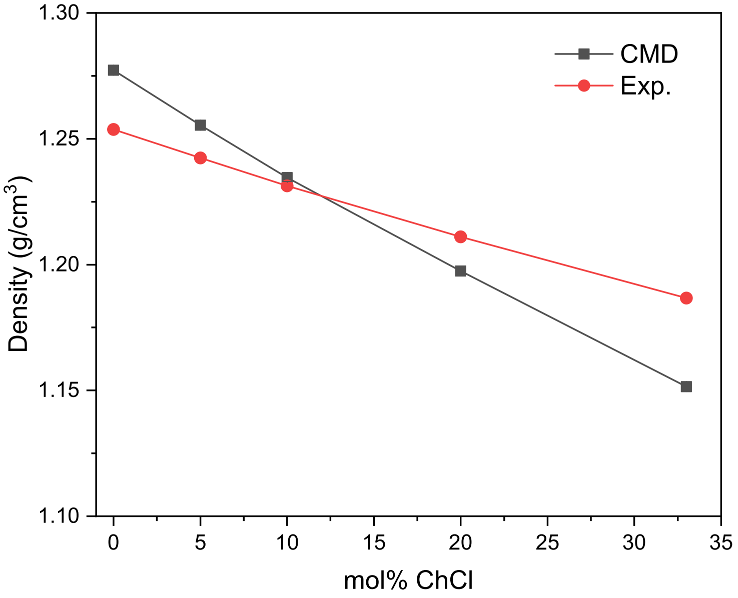

Figure 5.4: Density as a function of mol% Choline Chloride in Glycerol at 300K for CMD and experimental methods.

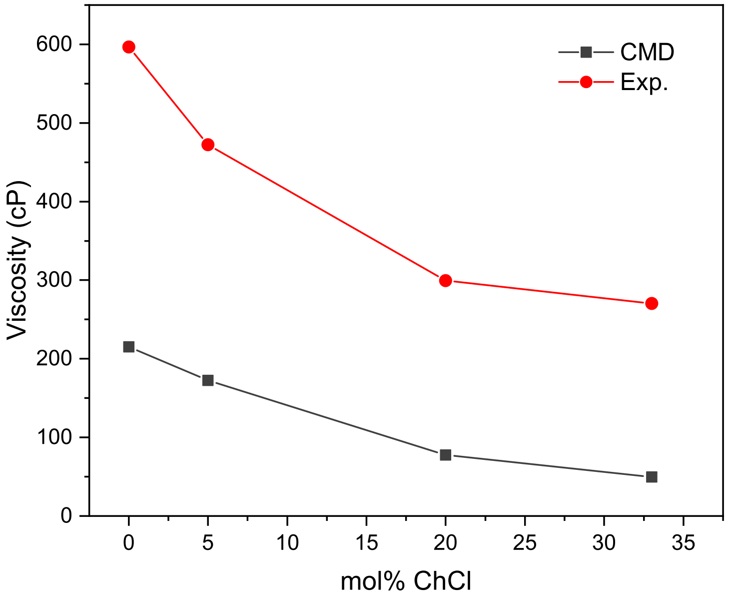

Figure 5.5: Viscosity as a function of mol% Choline Chloride in Glycerol at 300K for CMD and experimental methods.

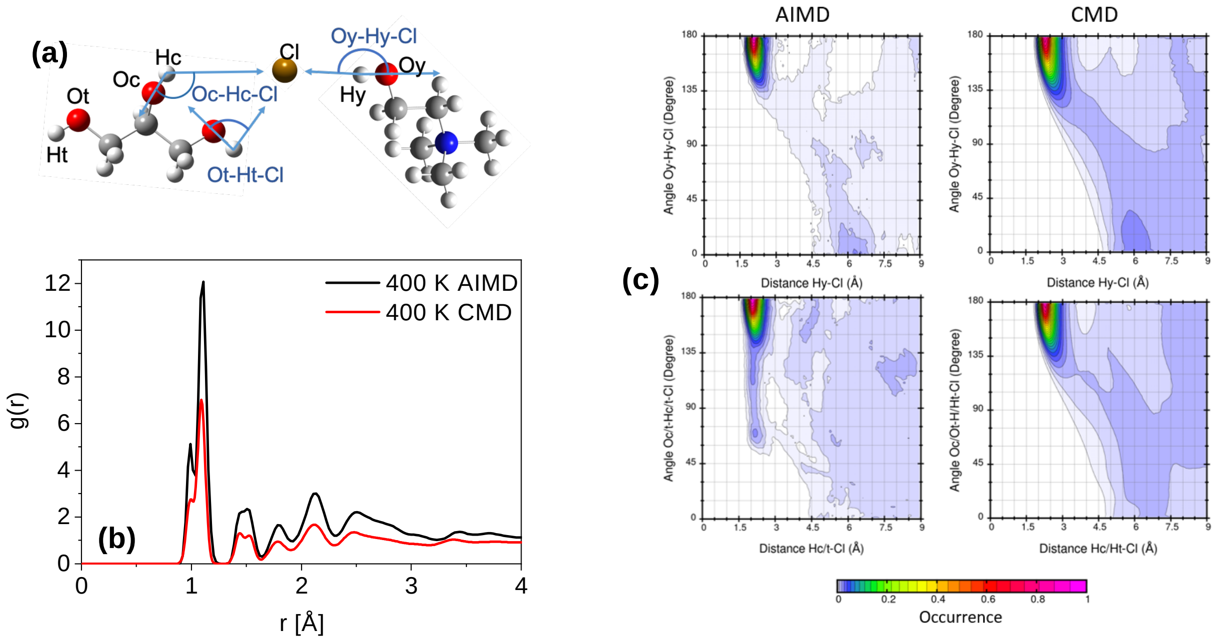

Figure 5.6: Simulated RDFs and CDFs by AIMD and CMD showing reasonable quantitative agreement. (a) The labeled atoms in black, Ht, Ot, Oc, Hc, Oy, Hy, and Cl, represent the different atoms in glycerol (left) and ChCl (right). The angles between atoms defined for the combined distribution functions are expressed in blue. (b) Comparison of CMD and AIMD overall radial distribution functions of 33 mol% ChCl in glycerol at 400 K. (c) Combined distribution functions (radial distribution between a hydroxyl hydrogen-Cl on the x-axis and angular distribution, defined in blue text in (a), on the y-axis) of chloride to the choline hydroxyl (top) and all three glycerol hydroxyl groups (bottom) from AIMD and CMD simulations at 400 K. Data were normalized to a range between 0 and 1 to generate the color scale provided.

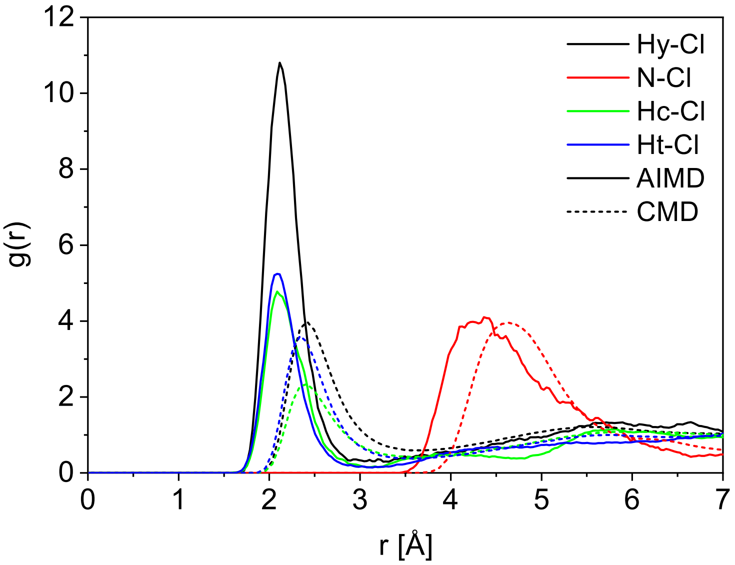

Figure 5.7: Partial RDFs for site–site interactions with chloride from CMD and AIMD simulations at 400K.

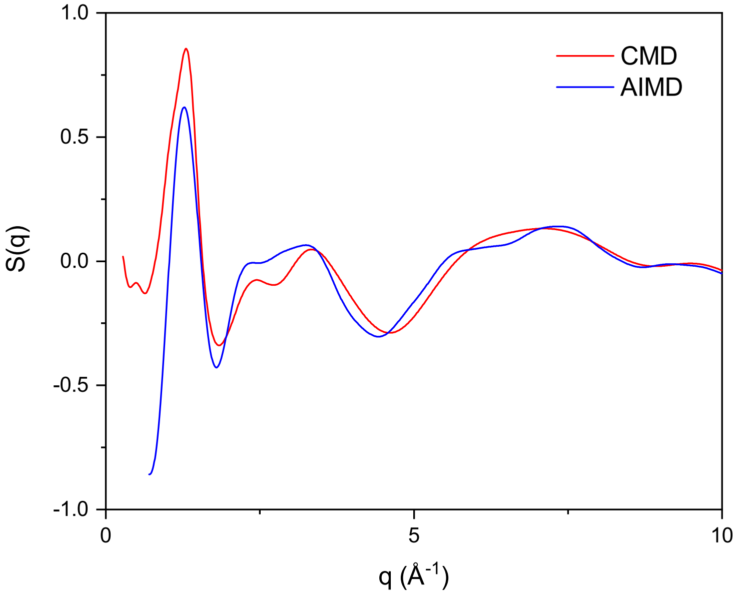

Figure 5.8: Comparison of CMD and AIMD simulated neutron scattering $S(q)$ versus q for 33 mol% ChCl in Glycerol at 400K.

high intensity regions in Figure 5.6c are consistent with even the most stringent hydrogen bonding criteria. In AIMD, chloride has an average donor-acceptor distance of 2.1 Å and a high probability of bonding angles greater than 150°. In CMD, the average donor-acceptor distance is 2.4 Å and a high probability of bonding angles greater than 135°. Based on the above discussion, agreement across the overall RDF, N_{coord}, S(q), and CDFs suggests that the force field used in the CMD simulations adequately captures the local structure of Glyceline, and can thus be used for large scale and long simulation times needed for analysis of dynamics.

The N_{coord} shown in Table 5.4 provide quantitative insight about the hydrogen bonded nature of 5mol% and 33mol% ChCl in glycerol. AIMD simulations at 33mol% indicate that the chloride anion does not selectively coordinate with the Hc or Ht hydrogens of glycerol, with N_{coord} of 0.62 (Hc) and 1.27 (Ht), respectively, considering the 1:2 ratio of Hc:Ht in glycerol. CMD results for 300K, 340K (provided in Table 5.5), and 400K show a slight preference for Ht with a ratio closer to 1:2.5, though this still indicates no strong selectivity of the Cl. These results agree with the ^{1}H NMR data at 333 K in Figure 5.2, which show a uniform shift of the Hc (e) and Ht (a) peaks as ChCl concentration is increased, rather than heterogeneous shift between the two protons that would indicate preferential association with chloride. At 300 K, however, the picture is slightly different, where Ht is moderately favored over Hc. The ratio of Hc and Ht coordinating with Cl remains the same at both low and high HBA concentrations. Choline self-interactions (Oy-Hy) are virtually non-existent at all concentrations. At low ChCl concentrations, choline is primarily solvated by the abundant glycerol molecules. As ChCl concentration is increased, a reduced coordination of the oxygen atom on choline by glycerol is observed through a decrease in N_{coord} of Oy-Hc and Oy-Ht. Furthermore, the hydroxyl proton of choline still mildly associates with glycerol at higher concentrations, indicated by slightly higher Oc-Hy and Oc-Hy numbers. However, there is a much stronger affinity to the chloride anions shown by the significantly elevated Cl-Hy and Cl-N coordination numbers. Chloride functions as an HBA and “linker“ that is capable of forming multiple hydrogen bonds with glycerol, as supported by high coordination numbers of Cl-Hc/t at 33mol% and much lower Oc/t-Hc/t interactions. On the other hand, all the

Table 5.4: Coordination numbers ($\mathrm{N_{coord}}$) for 5 and 33mol% ChCl in glycerol from CMD and AIMD at the specified temperatures (Gly = glycerol). Provided are the peak maxima ($\mathrm{r_{max}}$) and peak minima ($\mathrm{r_{min}}$) of the first solvation shell determined from radial distribution functions in angstrom. The first listed atom is the reference molecule and the second atom is the observed molecule. CMD coordination numbers for all concentrations are provided in Table 5.6.

		CMD 5mol% (300 K)			CMD 33mol% (300 K)			CMD 33mol% (400 K)			AIMD 33mol% (400 K)		
	site-site	$\mathrm{r_{max}}$	$\mathrm{r_{min}}$	$\mathrm{N_{coord}}$	$\mathrm{r_{max}}$	$\mathrm{r_{min}}$	$\mathrm{N_{coord}}$	$\mathrm{r_{max}}$	$\mathrm{r_{min}}$	$\mathrm{N_{coord}}$	$\mathrm{r_{max}}$	$\mathrm{r_{min}}$	$\mathrm{N_{coord}}$
Gly-Gly	Oc-Hc	1.9	2.5	0.28	1.9	2.5	0.19	1.9	2.6	0.14	1.8	2.6	0.19
	Oc-Ht	1.8	2.5	0.50	1.8	2.5	0.31	1.9	2.5	0.26	1.8	2.5	0.39
	Ot-Hc	1.8	2.5	0.31	1.8	2.6	0.22	1.9	2.6	0.17	1.8	2.5	0.22
	Ot-Ht	1.8	2.5	0.65	1.8	2.5	0.42	1.8	2.6	0.35	1.8	2.6	0.26
Cl-Gly	Cl-Hc	2.4	3.3	0.81	2.4	3.4	0.55	2.4	3.6	0.63	2.1	3.1	0.62
	Cl-Ht	2.3	3.3	2.33	2.3	3.4	1.42	2.3	3.6	1.54	2.1	3.2	1.27
Cl-Ch	Cl-Hy	2.4	3.4	0.11	2.4	3.5	0.50	2.4	3.6	0.52	2.1	3.0	0.62
	Cl-N	4.6	7.3	1.09	4.0	5.3	2.53	4.3	6.4	2.95	4.4	6.7	3.72
Gly-Ch	Oc-Hy	1.9	2.5	0.01	1.9	2.6	0.08	2.0	2.6	0.08	1.8	2.5	0.09
	Ot-Hy	1.9	2.6	0.02	1.9	2.6	0.10	1.9	2.7	0.09	1.9	2.5	0.04
	Oy-Hc	2.1	2.5	0.09	2.1	2.5	0.05	2.2	2.4	0.04	1.9	2.5	0.04
	Oy-Ht	2.0	2.4	0.11	2.1	2.4	0.05	2.2	2.3	0.05	1.9	2.5	0.15
Ch-Ch	Oy-Hy	2.1	2.3	0.00	2.1	2.3	0.01	2.1	2.3	0.01	1.9	2.6	0.04

Table 5.5: Coordination numbers and standard deviation of coordination numbers derived from three 6ns long CMD simulations at 340K for 33 mol% ChCl in Glycerol.

		33% 340K	
	site-site	Ncoor	stdev
Gly-Gly	Oc-Hc	0.17	0.0007
	Oc-Ht	0.28	0.0018
	Ot-Hc	0.20	0.0006
	Ot-Ht	0.38	0.0011
Cl-Gly	Cl-Hc	0.59	0.0026
	Cl-Ht	1.47	0.0075
Cl-Ch	Cl-Hy	0.51	0.0054
Gly-Ch	Oc-Hy	0.08	0.0002
	Ot-Hy	0.10	0.0006
Ch-Gly	Oy-Hc	0.04	0.0142
	Oy-Ht	0.05	0.0049
Ch-Ch	Oy-Hy	0.01	0.0037

Table 5.6: Full coordination numbers and standard deviation of coordination numbers derived from CMD simulations at 300K for 0, 5, 10, 20, and 33 mol% ChCl in Glycerol.

		0 mol%		5 mol%		10 mol%		20 mol%		33 mol%	
	site-site	N_{coor}	stdev	N_{coor}	stdev	N_{coor}	stdev	N_{coor}	stdev	N_{coor}	stdev
Gly-Gly	Oc-Hc	0.30	0.0005	0.28	0.002	0.26	0.0013	0.23	0.0027	0.31	0.0013
	Oc-Ht	0.53	0.0016	0.50	0.002	0.46	0.0032	0.39	0.0022	0.08	0.0009
	Ot-Hc	0.32	0.0008	0.31	0.001	0.29	0.0012	0.25	0.0011	0.42	0.0023
	Ot-Ht	0.71	0.0008	0.65	0.001	0.61	0.0016	0.52	0.0023	0.10	0.0009
Cl-Gly	Cl-Hc	-	-	0.81	0.030	0.76	0.0103	0.67	0.0056	0.55	0.0086
	Cl-Ht	-	-	2.33	0.030	2.13	0.0199	1.82	0.0092	1.42	0.0111
Cl-Ch	Cl-Hy	-	-	0.11	0.011	0.21	0.0109	0.34	0.0059	0.50	0.0087
Gly-Ch	Oc-Hy	-	-	0.01	0.001	0.03	0.0011	0.05	0.0006	0.08	0.0009
	Ot-Hy	-	-	0.02	0.000	0.03	0.0004	0.06	0.0005	0.10	0.0009
Ch-Gly	Oy-Hc	-	-	0.09	0.008	0.09	0.0052	0.07	0.0051	0.05	0.0030
	Oy-Ht	-	-	0.11	0.014	0.10	0.0067	0.08	0.0007	0.05	0.0009
Ch-Ch	Oy-Hy	-	-	0.00	0.001	0.00	0.0008	0.01	0.0008	0.01	0.0002

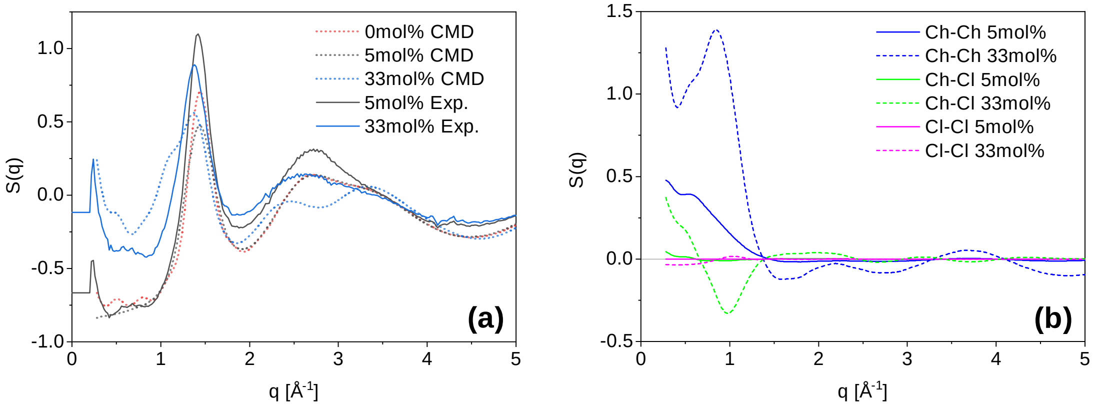

Figure 5.9: Experimental and simulated structure factors for 5 and 33mol% ChCl in glycerol decomposed. (a) Structure factors obtained from CMD simulations (0, 5, and 33mol% ChCl in glycerol) and WANS (5, and 33mol% ChCl) at 300 K. (b) Comparison of 5 and 33mol% for choline–choline, choline–chloride, and chloride–chloride interactions from CMD simulations.

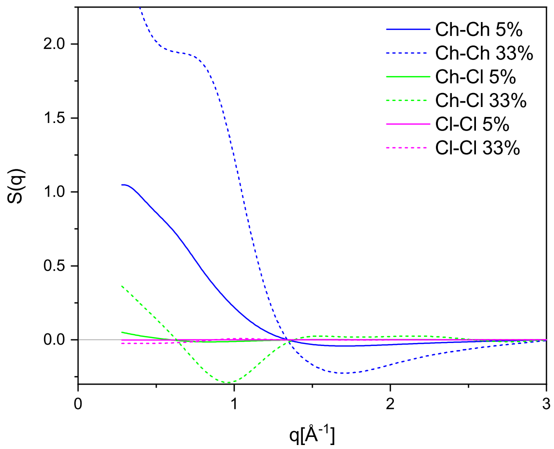

Figure 5.10: The structure factors associated with the ionic species obtained from neutron scattering for fully deuterated ChCl/glycerol mixtures.

N_{coord} associated with all Oy are near zero at 300 K, showing that choline does not function as an HBA in any appreciable capacity at room temperature.

For a further understanding of the impact of the HBA concentration on the evolution of the glycerol structure, we performed WANS experiments at 300 K. The structure factors, $S(q)$, of 5 and 33mol% d-ChCl in d-glycerol are shown in Figure 5.9a. The calculated results from CMD simulations at 0, 5, and 33 mol% ChCl are also provided. It is evident that the simulations are able to capture the key features and trends of the experimental $S(q)$ profiles. The peak at approximately 1.5 Å^{-1}, likely associated with the first solvation shell of glycerol-glycerol interactions, shifts to longer length-scales (lower q) with increasing ChCl concentration. This indicates that glycerol self-interactions are weakened as ChCl is introduced, which is consistent with N_{coord} trends. There are some noted deviations between simulations and experiments, seen as a shoulder at 1 Å^{-1} and peak splitting between 2 and 4 Å^{-1} in simulated 33 mol%. This is attributed to Ch–Ch interactions and is due to the mixed deuteration state of the experimental choline, something that was seen in Ethaline structure factors of a previous work.[97] A key advantage of the simulated structure factors is the ability to decompose the total profile and isolate individual molecule–molecule and atom–atom interactions. The decomposed Ch–Ch, Ch–Cl, and Cl–Cl correlations are shown in Figure 3b. At approximately 1.0 Å^{-1}, both Ch–Ch and Cl–Cl correlations show a positive feature whereas Ch–Cl has a negative feature in the 33mol% ChCl mixture in glycerol, which is the signature of a charge alternation structure.[219, 220] In order to rule out ambiguities from mixed deuteration and protiation states, as these have mixed negative and positive form factors, fully deuterated results are provided in Figure 5.10. These results also exhibit charge alternation occurring at the same q as Figure 5.9b.

5.4.2 Rotational and Translational Dynamics

Now, we investigate the evolution of the macroscopic properties of the ChCl and glycerol mixtures to determine how the microscopic changes in interactions of the HBN affect the bulk properties. To do so, BDS, DMS, and fs-TA spectroscopy are employed to obtain information

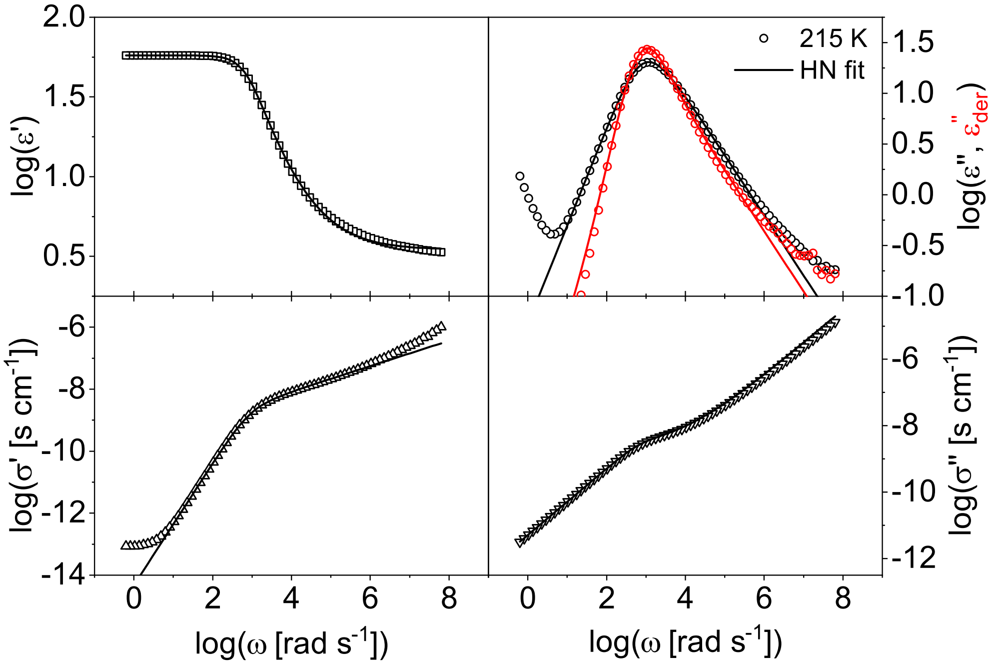

Figure 5.11: Real and imaginary parts of the complex dielectric function and complex conductivity function for glycerol at 215 K. The derivative representation of the dielectric loss is plotted in red. Solid lines are fits, which is a single Havriliak-Negami function.

Table 5.7: Fitting parameters for dielectric data of glycerol using a Havriliak-Negami function.

Temp. [K]	ε_∞	$\Delta\varepsilon$	τ_α [s]	β	γ
200	3.99	61.3	3.88E-01	0.90	0.67
205	3.89	57.7	4.19E-02	0.94	0.63
210	3.39	56.1	6.84E-03	0.96	0.61
215	3.50	54.2	1.28E-03	0.97	0.61
220	3.60	52.4	2.84E-04	0.97	0.62
225	3.60	50.7	7.44E-05	0.97	0.63
230	3.60	49.2	2.19E-05	0.97	0.64
235	3.70	47.5	7.19E-06	0.97	0.65
240	3.70	46.1	2.62E-06	0.97	0.66
245	3.70	44.6	1.05E-06	0.98	0.66
250	3.70	43.3	4.55E-07	0.98	0.66
255	3.69	41.9	2.04E-07	0.98	0.67
260	3.20	41.2	1.03E-07	0.98	0.66
265	3.30	39.8	5.15E-08	0.98	0.67
270	3.20	38.8	2.81E-08	0.98	0.68

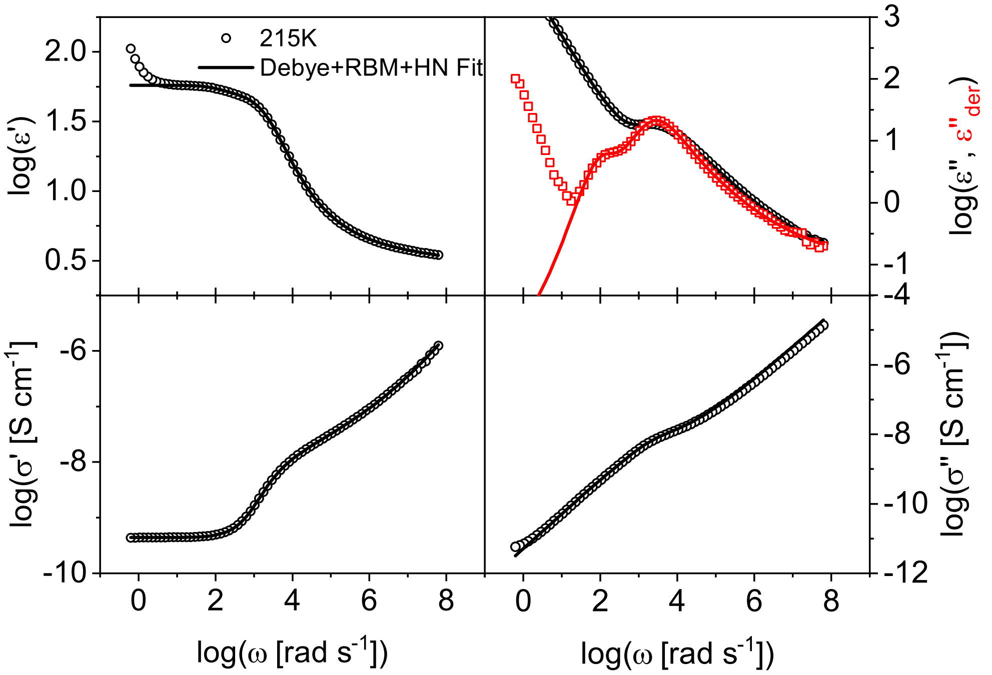

Figure 5.12: Real and imaginary parts of the complex dielectric function and complex conductivity function for 5mol% ChCl in glycerol at 215 K. The derivative representation of the dielectric loss is plotted in red. Solid lines are fits, which is are a combination of a Debye function, Havriliak-Negami , and a Random Barrier Model.

Table 5.8: Fitting parameters for dielectric data of 5mol% ChCl in glycerol using a Debye, Havriliak-Negami function, and Random Barrier Model.

Temp. [K]	ε_∞	$\Delta\varepsilon_{slow}$	τ_{slow} [s]	$\Delta\varepsilon_\alpha$	τ_α [s]	β	γ	σ_0 [S cm^{-1}]	τ_{ion} [s]
205	1.96	6.31	1.92E-01	43.8	1.09E-02	0.84	0.79	2.11E-11	8.20E-02
210	2.00	6.12	3.66E-02	42.1	1.94E-03	0.85	0.77	1.06E-10	1.56E-02
215	1.92	5.82	8.53E-03	40.3	4.18E-04	0.87	0.77	4.42E-10	3.82E-03
220	2.00	5.63	2.18E-03	39.1	1.08E-04	0.88	0.76	1.61E-09	9.88E-04
225	2.05	5.44	6.21E-04	37.8	3.17E-05	0.90	0.75	5.25E-09	2.86E-04
230	1.95	5.09	2.11E-04	36.3	1.00E-05	0.90	0.75	1.58E-08	9.84E-05
235	2.30	5.10	6.59E-05	35.9	3.60E-06	0.91	0.75	4.38E-08	2.82E-05
240	1.93	4.71	2.65E-05	33.7	1.39E-06	0.93	0.74	1.11E-07	1.35E-05
245	2.00	4.71	1.09E-05	32.8	6.03E-07	0.94	0.72	2.62E-07	5.22E-06
250	2.00	4.62	4.59E-06	33.2	2.84E-07	0.94	0.70	5.84E-07	1.82E-06

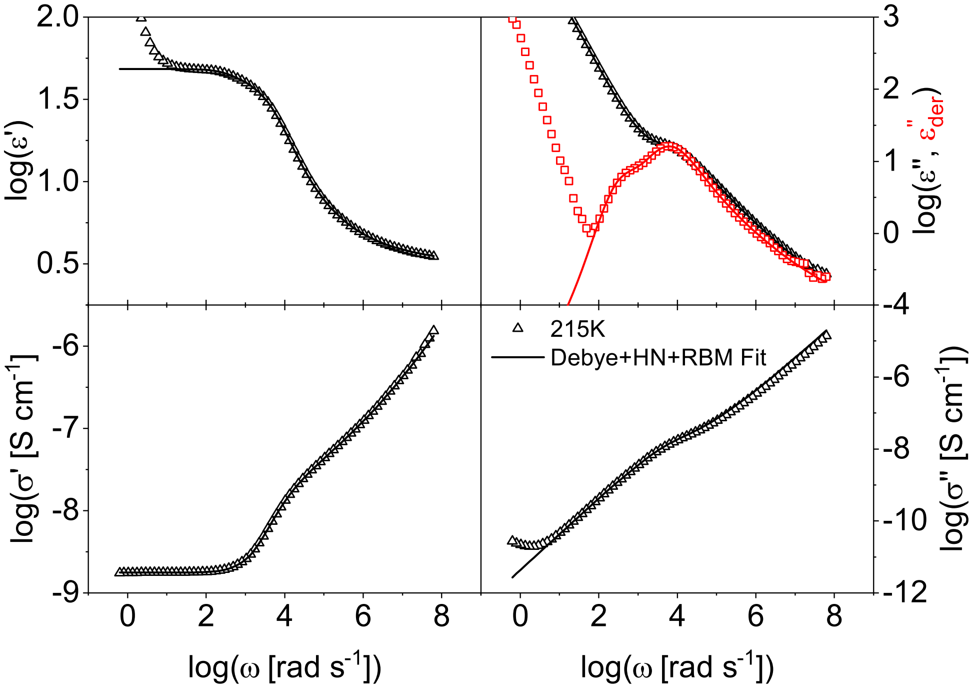

Figure 5.13: Real and imaginary parts of the complex dielectric function and complex conductivity function for 10mol% ChCl in glycerol at 215 K. The derivative representation of the dielectric loss is plotted in red. Solid lines are fits, which is are a combination of a Debye function, Havriliak-Negami , and a Random Barrier Model.

Table 5.9: Fitting parameters for dielectric data of 10mol% ChCl in glycerol using a Debye, Havriliak-Negami function, and Random Barrier Model.

Temp. [K]	ε_∞	$\Delta\varepsilon_{slow}$	τ_{slow} [s]	$\Delta\varepsilon_\alpha$	τ_α [s]	β	γ	σ_0 [S cm^{-1}]	τ_{ion} [s]
200	2.13	5.88	2.44E-01	37.7	2.64E-02	0.75	0.87	1.85E-11	7.81E-02
205	2.00	5.45	4.55E-02	35.9	4.02E-03	0.75	0.89	9.93E-11	1.55E-02
210	2.00	5.54	9.49E-03	34.2	7.96E-04	0.78	0.86	4.53E-10	3.30E-03
215	2.00	5.58	2.26E-03	32.6	1.88E-04	0.80	0.84	1.76E-09	8.27E-04
220	2.00	5.46	6.36E-04	31.2	5.23E-05	0.82	0.83	6.00E-09	2.37E-04
225	2.00	5.03	2.04E-04	30.3	1.60E-05	0.82	0.84	1.86E-08	7.52E-05
230	2.00	4.99	6.56E-05	28.9	5.45E-06	0.84	0.82	5.30E-08	2.58E-05
235	2.00	4.76	2.58E-05	27.8	2.11E-06	0.84	0.83	1.33E-07	1.03E-05
240	2.00	4.68	9.55E-06	26.7	8.23E-07	0.87	0.80	3.44E-07	3.80E-06
245	2.94	4.09	4.24E-06	29.5	4.07E-07	0.86	0.77	7.85E-07	6.77E-07
250	2.00	3.78	1.90E-06	26.8	1.77E-07	0.85	0.80	1.67E-06	6.09E-07

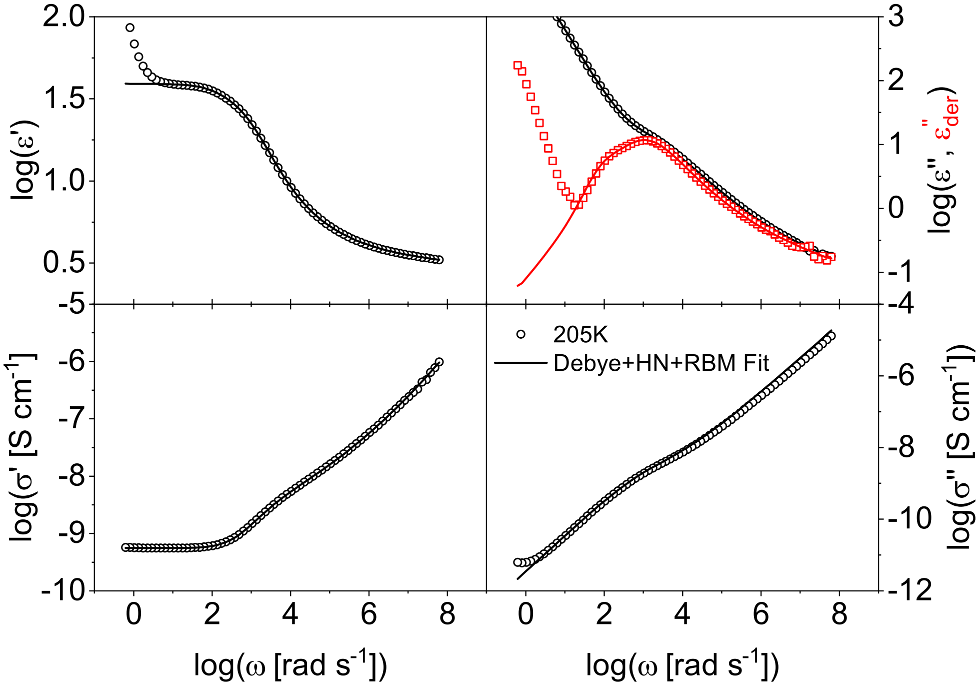

Figure 5.14: Real and imaginary parts of the complex dielectric function and complex conductivity function for 20mol% ChCl in glycerol at 205 K. The derivative representation of the dielectric loss is plotted in red. Solid lines are fits, which is are a combination of a Debye function, Havriliak-Negami , and a Random Barrier Model.

Table 5.10: Fitting parameters for dielectric data of 20mol% ChCl in glycerol using a Debye, Havriliak-Negami function, and Random Barrier Model.

Temp. [K]	ε_∞	$\Delta\varepsilon_{slow}$	τ_{slow} [s]	$\Delta\varepsilon_\alpha$	τ_α [s]	β	γ	σ_0 [S cm^{-1}]	τ_{ion} [s]
200	2.13	5.88	2.44E-01	37.7	2.64E-02	0.75	0.87	1.85E-11	7.81E-02
205	2.00	5.45	4.55E-02	35.9	4.02E-03	0.75	0.89	9.93E-11	1.55E-02
210	2.00	5.54	9.49E-03	34.2	7.96E-04	0.78	0.86	4.53E-10	3.30E-03
215	2.00	5.58	2.26E-03	32.6	1.88E-04	0.80	0.84	1.76E-09	8.27E-04
220	2.00	5.46	6.36E-04	31.2	5.23E-05	0.82	0.83	6.00E-09	2.37E-04
225	2.00	5.03	2.04E-04	30.3	1.60E-05	0.82	0.84	1.86E-08	7.52E-05
230	2.00	4.99	6.56E-05	28.9	5.45E-06	0.84	0.82	5.30E-08	2.58E-05
235	2.00	4.76	2.58E-05	27.8	2.11E-06	0.84	0.83	1.33E-07	1.03E-05
240	2.00	4.68	9.55E-06	26.7	8.23E-07	0.87	0.80	3.44E-07	3.80E-06
245	2.94	4.09	4.24E-06	29.5	4.07E-07	0.86	0.77	7.85E-07	6.77E-07
250	2.00	3.78	1.90E-06	26.8	1.77E-07	0.85	0.80	1.67E-06	6.09E-07

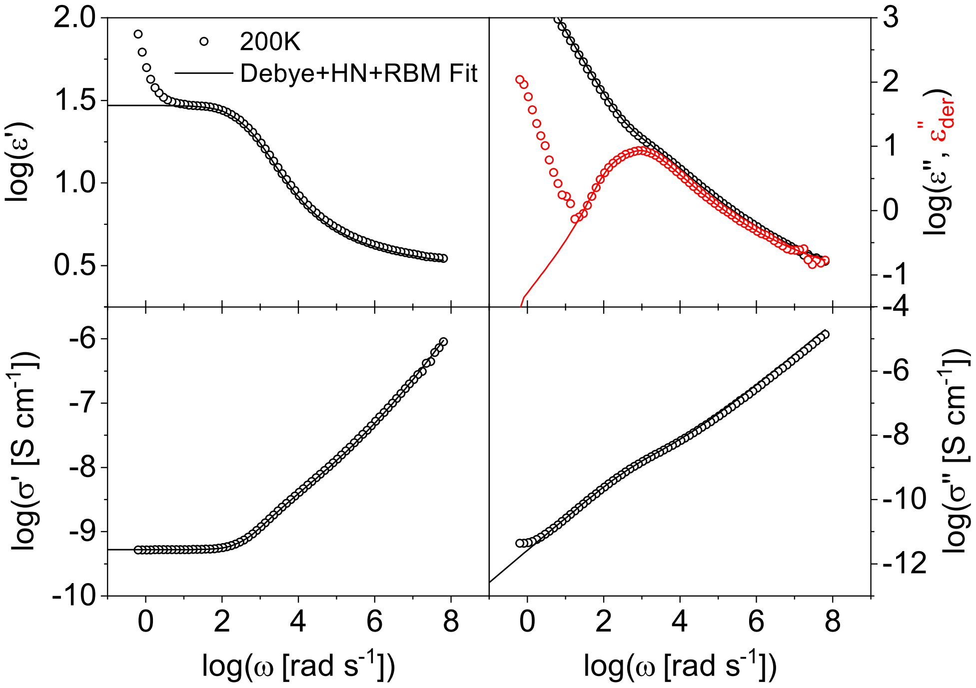

Figure 5.15: Real and imaginary parts of the complex dielectric function and complex conductivity function for 33mol% ChCl in glycerol at 200 K. The derivative representation of the dielectric loss is plotted in red. Solid lines are fits, which is are a combination of a Debye function, Havriliak-Negami , and a Random Barrier Model.

Table 5.11: Fitting parameters for dielectric data of 33mol% ChCl in glycerol using a Debye, Havriliak-Negami function, and Random Barrier Model.

Temp. [K]	ε_∞	$\Delta\varepsilon_{slow}$	τ_{slow} [s]	$\Delta\varepsilon_\alpha$	τ_α [s]	β	γ	σ_0 [S cm^{-1}]	τ_{ion} [s]
190	2.33	2.57	1.85E-01	19.0	5.82E-02	0.74	0.76	1.72E-11	7.73E-02
195	2.33	2.81	2.76E-02	19.1	8.00E-03	0.76	0.73	1.23E-10	1.05E-02
200	2.25	2.31	5.68E-03	18.0	1.43E-03	0.74	0.79	5.58E-10	2.33E-03
205	2.26	2.49	1.27E-03	17.9	3.02E-04	0.76	0.76	2.37E-09	5.41E-04
210	2.25	2.08	3.65E-04	17.0	7.95E-05	0.76	0.79	7.99E-09	1.54E-04
215	2.45	2.39	1.04E-04	17.4	2.47E-05	0.80	0.72	2.77E-08	3.75E-05
220	2.25	2.02	3.64E-05	15.7	7.85E-06	0.78	0.79	7.38E-08	1.58E-05
225	2.24	2.32	1.29E-05	15.3	2.81E-06	0.81	0.76	2.10E-07	5.60E-06
230	2.25	1.14	5.85E-06	15.8	1.28E-06	0.78	0.79	4.90E-07	2.18E-06
235	2.24	1.67	2.24E-06	15.3	5.68E-07	0.84	0.70	1.22E-06	8.39E-07
300	2.24	1.60	2.87E-09	14.5	6.59E-10	0.79	0.78	7.99E-04	1.84E-09

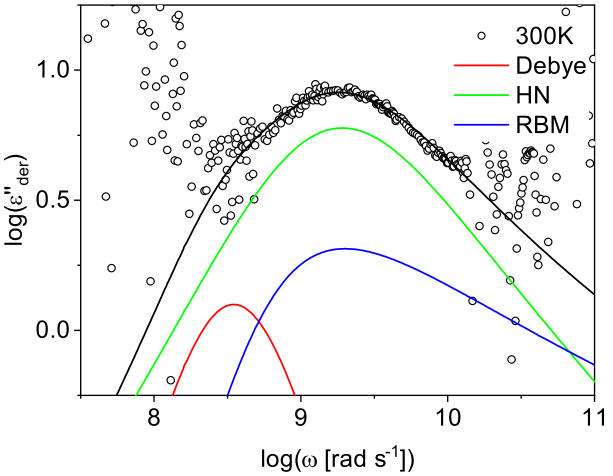

Figure 5.16: The derivative representation of the dielectric loss for 33mol% ChCl in glycerol at room temperature plotted as a function of radial frequency.

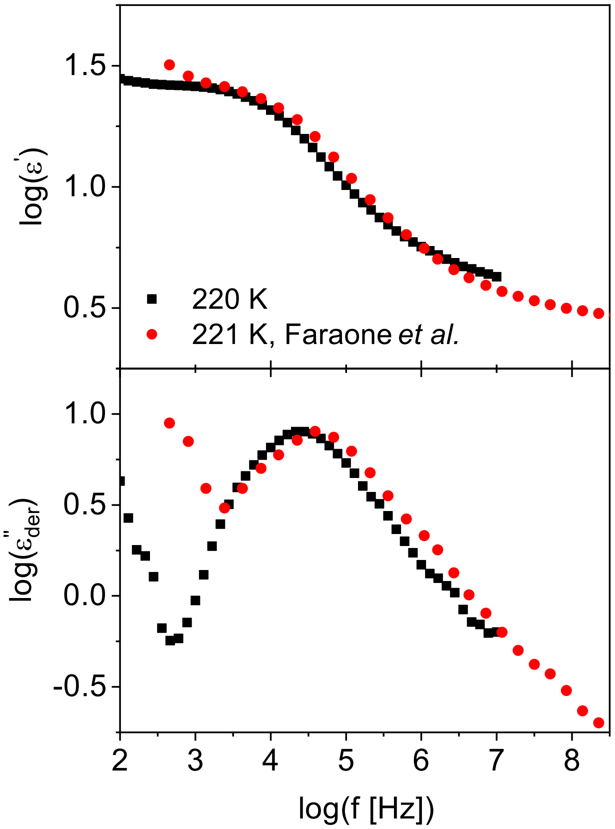

Figure 5.17: Top: Real part of complex permittivity for 33mol% ChCl in glycerol obtained for this paper and from Faraone *et al.* and 220 and 221 K respectively. Bottom: The derivative representation of the dielectric loss at 220 and 221 K from this paper and Faraone *et al.* respectively.

about the dynamics of the mixtures up to the eutectic composition. In Figure 5.18a, the derivative representation of the dielectric loss is shown for glycerol (top) and 5mol% ChCl in glycerol (bottom). For dipolar liquids, the primary dielectric relaxation is typically due to reorientations of molecular dipoles and is easily visible as a peak in the dielectric loss. This is commonly referred to as the structural, α-relaxation and is associated with the dynamic glass transition.[10, 16] In neat glycerol, only the α-relaxation is clearly observed. Upon the addition of ChCl, contributions from ion dynamics (dash-dot line) are observed, and a unique, slower relaxation emerges (shaded region). BDS data at a representative temperature for each concentration are provided in Figures 5.11-5.15 and all fitting parameters are provided in Tables 5.7-5.11. At low temperatures, we examine how dynamics change as the glass transition is approached. Additionally, a room temperature BDS measurement of 33mol% ChCl in glycerol is included in Figure 5.16 to show that trends and observations in the low temperature data hold true for higher temperatures as well. The slow, sub-α dielectric relaxation has not been reported in DESs before, presumably because the data were not analyzed in such detail. Faraone *et al.* studied BDS of Glyceline and only reported the structural relaxation and ion dynamics, however, the derivative representation of the dielectric loss was not examined, which is where the sub-α relaxation becomes obvious.[113] If considered, the sub-α relaxation is observed in their data as well (Figure 5.17).

Figure 5.18b shows a normalized plot of the dynamic mechanical spectra at different concentrations. The curves are normalized by the corresponding zero-shear viscosity (η_0) and mechanical structural relaxation rate (ω_α) for each concentration for straightforward comparison of the spectral shapes to evaluate the possible emergence of dynamic heterogeneity in the mixtures. Two distinct dynamic modes are observed for all compositions, namely the mechanical structural relaxation and a slow mechanical relaxation. This slow mechanical relaxation has been previously attributed to the motion of the HBN of glycerol.[221] It is clear from Figure 5.18b that the spectral shapes remain unaltered with addition of ChCl. This implies that although the mean rates of dynamics are increasing with composition towards the eutectic composition, the general form of the glycerol HBN is largely preserved up to the eutectic composition. The NMR data combined with WANS and MD simulations

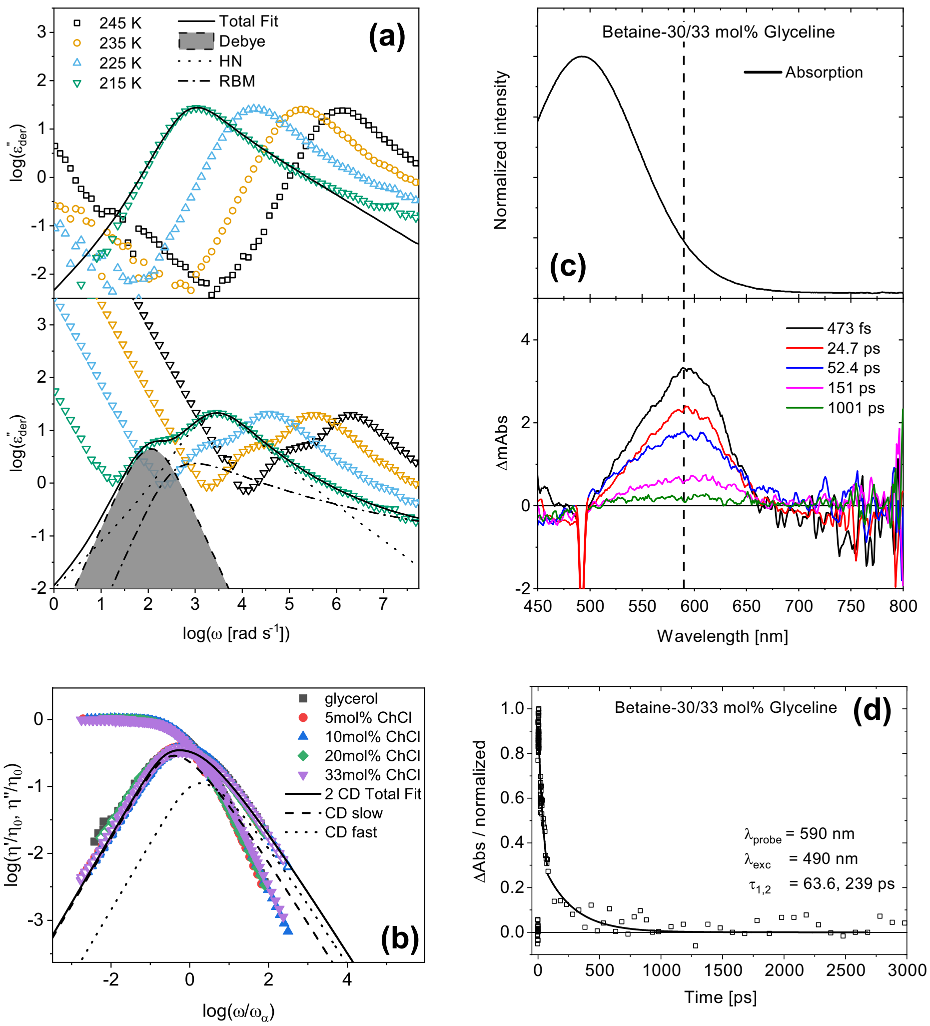

Figure 5.18: Dynamics measured from BDS, DMS, and fs-TA spectroscopy. (a) Top: The derivative representation of the dielectric loss, $\varepsilon^{''}_{der}[= -\pi/2\ \partial\varepsilon'/\partial ln(\omega)]$, for glycerol at selected temperatures plotted as a function of radial frequency. Bottom: $\varepsilon^{''}_{der}$ of 5mol% ChCl in glycerol plotted versus radial frequency at the same temperatures shown for glycerol. The solid black lines denote fits that account for the cumulative contributions observed in the mixtures. For glycerol, the fit comprises of a single empirical Havriliak-Negami function, while the fit for 5mol% ChCl (and all high ChCl concentrations measured) is the linear addition of a Debye function (shaded region), Havriliak-Negami (dotted line) and Random-Barrier Model (dash-dot line). Fits are described in the SI. (b) The real and imaginary parts of viscosity, η' and η'', for 0, 5, 10, 20, and 33 mol% ChCl in glycerol obtained from a time-temperature superposition as described in the DMS methods section, normalized by the corresponding zero-shear viscosity plotted versus angular frequency normalized by the mechanical structural relaxation rate at each concentration. The dotted line represents the probe wavelength at 590 nm. (c) Top panel: Steady-state UV-visible absorption of betaine-30, bottom panel: femtosecond transient absorption spectra at indicated delay times. (d) fs-TA kinetics of betaine-30 in 33 mol% Glyceline at a probe wavelength of 590 nm. The solid line at 0.0 represents the baseline.

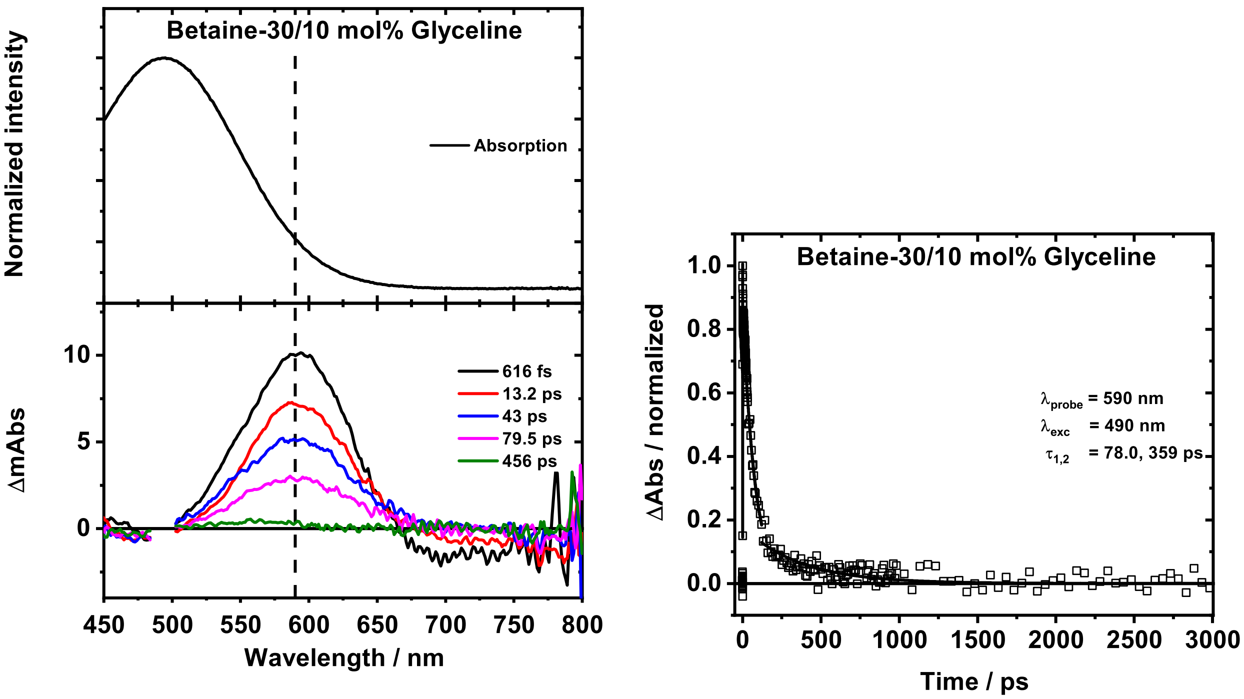

Figure 5.19: Left – top panel: Steady-state UV-visible absorption of betaine-30, bottom panel: femtosecond transient absorption spectra at indicated delay times. Right: – fs-TA kinetics of betaine-30 in 10 mol% Glyceline at a probe wavelength of 590 nm.

show that the addition of ChCl does alter the hydrogen bonds of glycerol and the nature of its HBN, however, the dynamic mechanical spectra suggest that the network is not completely disrupted. This is supported by previous reports, stating the HBN of glycerol is largely preserved at 33 mol% ChCl.[113, 112, 222] Figure 5.18c and 5.18d show the relaxation dynamics of betaine-30 (Reichardt's) dye in 33 mol% ChCl in glycerol. The absorption maxima and relaxation dynamics of betaine-30 are strongly influenced by its solvent environment. The longer time constant, τ_2, from fs-TA corresponds to orientational dynamics. By comparing the 10 mol% (Figure 5.19) and 33 mol% ChCl solvent systems, it is evident that the absorption maxima of our probe (betaine-30) remain unchanged between both DES compositions, indicating a similar dielectric constant from the perspective of the probe dye. However, the dynamics at higher ChCl concentration becomes faster, and the characteristic timescales obtained are in quantitative agreement with those of structural relaxation measured by BDS.

The mean structural relaxation rates (ω_α) obtained from all the techniques presented in Figure 5.18 are shown in Figure 5.20a for all mixtures investigated as a function of inverse temperature. The data for each concentration are well described by the Vogel-Fulcher-Tammann equation; $\tau = \tau_0 exp(A/(T - T_0))$, where τ_0, A, and T_0 are fitting parameters.[10] As temperature is decreased, the rate of dynamics for all relaxation processes is slowed down. Additionally, as the concentration of ChCl is increased up to the eutectic composition, the mean rates of the structural relaxation become faster. This shows that molecular mobility is increasing, which is consistent with the expectation of lowered melting temperature for the DES studied here.[109] Interestingly, the mean rates of orientational dynamics obtained from the fs-TA, BDS, and DMS are all in quantitative agreement. This remarkable agreement lends credence to our assignment of the primary dielectric relaxation to reorientational dynamics. Figure 5.20b displays the ε''_{der} data for the various concentrations plotted versus radial frequency normalized by the corresponding ω_α of each mixture. This shows the progression of the slow, sub-α relaxation with composition. It is clear that the slow, sub-α relaxation becomes faster relative to the structural relaxation with increasing concentration of ChCl. The same trend is observed for ChCl/EG mixtures, as shown in Figure 5.20d.

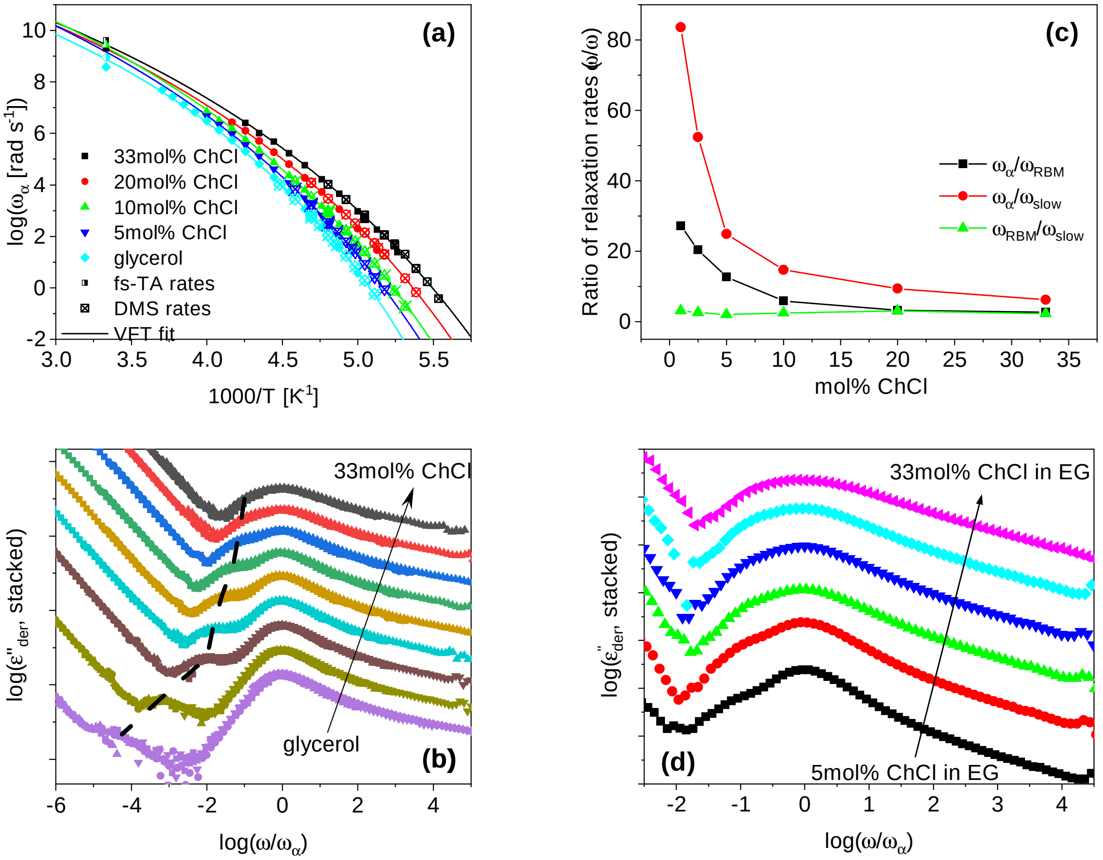

Figure 5.20: The dynamics become faster with increasing concentration. (a) Structural relaxation rates from dielectric, mechanical, and transient absorbance spectroscopy are plotted as a function of inverse temperature. The solid lines are fits obtained by the Vogel-Fulcher-Tammann equation. Parameters from these fits can be found in Table 5.12. (b) The ε''_{der} data for concentrations of 0, 0.05, 0.5, 1, 2.5, 5, 10, 20, and 33mol% ChCl in glycerol plotted versus radial frequency. The data is arbitrarily stacked to clearly show the evolution of the sub-α relaxation with increasing ChCl concentration. The dashed black line is a guide for the eyes to draw attention to the evolution of the sub-α relaxation. (c) The ratios of the various characteristic rates obtained from the dielectric spectra plotted versus mol% ChCl, at a constant T_{g}/T, showing that the slow relaxation is coupled to ion dynamics. (d) The ε''_{der} data for concentrations of 5, 10, 15, 20, 25, and 33mol% ChCl in EG plotted versus radial frequency. The data is arbitrarily stacked to clearly show the evolution of the sub-α relaxation with increasing ChCl concentration.

Table 5.12: Vogel-Fulcher-Tammann fit parameters for the structural relaxation rates for 0, 5, 10, 20, and 33mol% ChCl in glycerol.

	τ_0 [s]	T_0 [K]	A
glycerol	1.33E-15	127	2384
5mol% ChCl	1.93E-16	117	2755
10mol% ChCl	1.17E-16	114	2821
20mol% ChCl	5.04E-16	113	2592
33mol% ChCl	5.27E-16	109	2564

Table 5.13: Coefficients (time in ns) fitted to Equation 5.5 for the dipole moment rotational dynamics based on CMD simulations at 298 K.

	b_1	α_1	b_2	α_2	τ_1	τ_2	R^2
Choline							
0 mol%	-	-	-	-	-	-	-
5 mol%	0.4695	0.9690	0.5305	0.6212	0.4277 ±0.0993	0.0172 ±0.0099	0.9970
10 mol%	0.4308	0.9860	0.5692	0.6892	0.3739 ±0.0558	0.0184 ±0.0041	0.9984
20 mol%	0.4555	0.9659	0.5445	0.6846	0.2503 ±0.0228	0.0127 ±0.0017	0.9988
33 mol%	0.4607	0.9816	0.4258	0.7546	0.1681 ±0.0109	0.0092 ±0.0008	0.9977
Glycerol							
0 mol%	0.4748	0.9391	0.5252	0.6923	0.1403 ±0.0082	0.0016 ±0.0001	0.9963
5 mol%	0.4916	0.9142	0.5084	0.6394	0.1330 ±0.0081	0.0013 ±0.0006	0.9970
10 mol%	0.4881	0.9161	0.5119	0.6806	0.1286 ±0.0069	0.0014 ±0.0001	0.9971
20 mol%	0.4908	0.9150	0.5092	0.6919	0.1109 ±0.0061	0.0012 ±0.0005	0.9964
33 mol%	0.4599	0.9370	0.5143	0.7111	0.0924 ±0.0029	0.0014 ±0.0001	0.9959

Additionally, Figure 5.20c shows that the sub-α relaxation rate (ω_{slow}) is coupled to the ion hopping rate (ω_{ion}), and both are decoupled from ω_α in ChCl/glycerol mixtures. This suggests that the sub-α dielectric relaxation originates from ion rearrangements. These results are in contrast with recent reports by Faraone *et al.* and Reuter *et al.*, which suggested a strong coupling between ion dynamics and the structural relaxation.[113, 115] Again, their raw dielectric data for Glyceline agrees with ours, although electrode polarization appears at higher frequencies obscuring the slow mode that is revealed using the derivative formalism (Figure 5.17).

To further understand the potential microscopic origin of the sub-α relaxation observed in BDS, CMD simulations were used to obtain dipole moment rotational correlation functions of choline and glycerol at different compositions. These correlation functions were fit using the fraction kinetic model shown in equation 5.5 (found in the CMD methods section). The τ_1 is attributed to the reorientional motion of the molecules, while the shorter time process τ_2 is assigned to the dynamics associated with hydrogen bond formation and breaking events. All values calculated are shown in Table 5.13. Figure 5.21a plots τ_1 for choline and glycerol respectively, which shows that glycerol relaxes faster than choline for all mixtures up to the eutectic composition. Based on careful examination of the simulated dynamic profiles, we attribute the slow rotation of the choline cation at low concentrations to the "cage" created by neighboring glycerol molecules that remain interconnected through hydrogen bonding, leading to spatial and dynamic heterogeneities when viewed at the macroscopic length-scale. Moreover, as ChCl concentration is increased, the glycerol HBN is further weakened, which allows choline, along with the other molecules, to rotate more freely and easily. Choline rotates faster at a fixed timescale of glycerol motion, which is the same trend observed for the sub-α and α dielectric processes, respectively. Additionally considering the coupling of the sub-α relaxation to ion dynamics shown in Figure 5.20c, these results indicate that the origin of the sub-α relaxation is the slow choline rotational dynamics. While the overall dynamic trends observed in mixtures of EG and ChCl by CMD simulations are opposite to those of ChCl and glycerol, data shown in Table 5.14 indicates that choline dynamics are still slower than EG molecules at all concentrations.

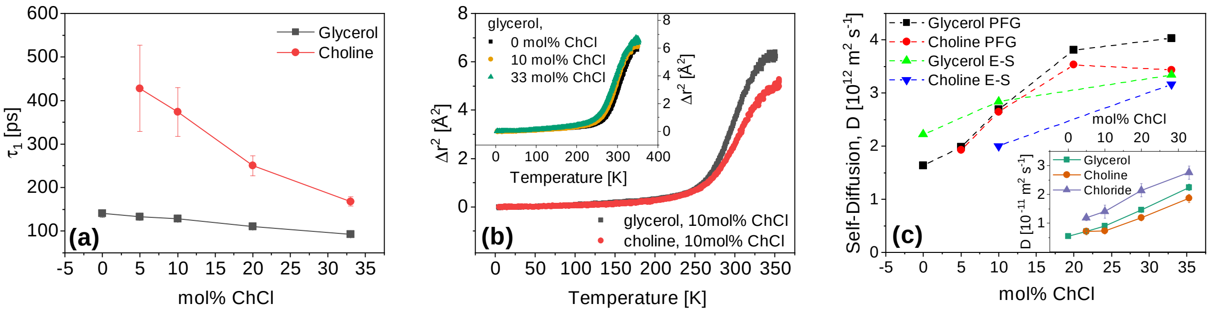

Figure 5.21: Glycerol diffuses and rotates faster than choline at all compositions. (a) The average slow characteristic time coefficient (τ_1) of dipole relaxation obtained from CMD simulations for choline and glycerol at various ChCl concentrations in glycerol. Error bars are one standard deviation from five independent simulations and fits. (b) Mean square displacement, $<\Delta r^2>$, of molecules in a mixture of 10mol% ChCl in glycerol as determined by quasielastic neutron scattering. Inset: MSD of ChCl/glycerol mixtures (black – pure glycerol; orange – 10mol% ChCl; green – 33mol% ChCl. (c) Diffusion coefficients determined from PFG-NMR and calculated from QENS data through the Einstein-Smoluchowski equation, denoted by PFG and E-S, respectively, of glycerol and choline at 298 K for compositions 0, 5, 10, 25, and 33mol% ChCl in glycerol. Inset: Average self-diffusion coefficients determined from CMD simulations of glycerol, choline, and chloride at 300 K for compositions 0, 5, 10, 20, and 33mol% ChCl in glycerol. Error bars are one standard deviation from five independent simulations.

Table 5.14: The average slow (τ_1) and fast (τ_2) characteristic time coefficients of dipole relaxation obtained from CMD simulations for choline and ethylene glycol at various ChCl concentrations in ethylene glycol.

		τ_1(ps)	τ_2(ps)
0% ChCl	EG	3.3	0.3
5% ChCl	Choline	25.0	2.2
	EG	4.9	0.3
10% ChCl	Choline	46.0	5.6
	EG	7.2	0.3
16.7% ChCl	Choline	84.1	9.3
	EG	12.2	0.4
20% ChCl	Choline	149.1	15.8
	EG	15.5	0.4
25% ChCl	Choline	210.1	17.8
	EG	22.6	0.5
33% ChCl	Choline	486.4	30.7
	EG	46.4	0.6

Figure 5.21b shows the mean square displacement (MSD) of the molecules in ChCl/glycerol mixtures over a timescale of approximately 2 ns obtained from QENS experiments. By selective deuteration, the motion of only one component in the mixture is monitored. The inset shows that the addition of ChCl leads to speeding up the motion of the glycerol as the concentration is raised towards the eutectic composition. This is consistent with all the results from other techniques in the current work, further demonstrating that the presence of ChCl modifies the HBN of glycerol, leading to enhanced molecular mobility. Figure 5.21b documents the motion of the glycerol (black curve) and the choline (red curve) in the 10mol% ChCl mixture. These data show that the motion of choline is slower than that of glycerol at this concentration. It is interesting to note that the QENS study by Wagle *et al.* uses a shorter timescale of 0.4 ns, and observes that choline is the faster component.[177]

To examine longer range translational dynamics, self-diffusion coefficients, D, were obtained from PFG-NMR and CMD simulations and are shown in Figure 5.21c. In addition, the Einstein-Smoluchowski equation was used to estimate the diffusion coefficient from QENS data through: $D = <\Delta r^2>/(6t)$, where t denotes the timescale.[29] Although the time- and length-scales of the two experiments differ by nearly three orders of magnitude, the values calculated from QENS agree remarkably with those from PFG-NMR, as shown in Figure 5.21c. While CMD dynamics are noticeably faster than PFG-NMR results, this is likely an effect of the significant charge scaling. resulting in faster bulk dynamics as mentioned before. Both methods show that the self-diffusivity of choline is slower than that of glycerol. In general, all the results indicate that the diffusivity increases with concentration of ChCl. Additionally, it is interesting to note from the inset of Figure 5.21c that chloride is the fastest species in the mixtures. Locally, CMD dipole moment rotational correlation time coefficients and QENS show that choline becomes faster relative to a fixed glycerol dynamic timescale with increasing ChCl concentration, which is the same trend observed in BDS between the sub-α and structural α-relaxation respectively.

To have a better understanding of the transport properties, the microscopic hydrogen bond dynamics was studied based on CMD simulations. Analysis of hydrogen bond dynamics performed through TRAVIS is based on reactive dynamic flux as laid out by Gehrke *et*

Table 5.15: Average hydrogen bond dynamics time constants (ps) derived from CMD simulations at 300K for 0, 5, 10, 20, and 33 mol% ChCl in Glycerol. τ_f is associated with hydrogen bond breaking and is equivalent to τ_{hb} which describes the average hydrogen bond lifetime. τ_b is the time constant of hydrogen bond reformation. Standard deviations of these values are provided in Supplementary Table 5.16.

		0 mol%		5 mol%		10 mol%		20 mol%		33 mol%	
	site-site	τ_f	τ_b	τ_f	τ_b	τ_f	τ_b	τ_f	τ_b	τ_f	τ_b
Gly-Gly	Oc-Hc	182.1	497.7	160.2	435.4	148.1	396.5	122.9	330.2	98.1	261.7
	Oc-Ht	181.2	467.5	167.2	487.2	153.8	459.0	127.5	420.6	103.2	388.4
	Ot-Hc	191.0	483.0	172.5	442.6	160.0	436.7	137.6	397.3	119.2	395.7
	Ot-Ht	182.1	497.7	198.7	390.8	182.4	356.4	150.8	290.6	122.7	233.3
Cl-Gly	Cl-Hc	-	-	162.9	159.9	148.5	162.9	114.8	125.8	87.4	91.9
	Cl-Ht	-	-	234.7	130.5	209.7	116.9	170.6	90.0	131.6	66.0
Cl-Ch	Cl-Hy	-	-	179.6	178.9	162.7	160.7	118.2	111.2	89.5	79.4
Gly-Ch	Oc-Hy	-	-	98.7	201.6	87.1	202.3	67.6	150.6	52.2	115.2
	Ot-Hy	-	-	117.7	204.9	105.2	181.6	79.4	128.8	62.3	95.0
Ch-Gly	Oy-Hc	-	-	67.5	612.7	66.5	527.3	54.6	501.6	42.8	383.5
	Oy-Ht	-	-	74.4	758.0	69.6	784.1	56.1	673.4	45.6	601.9
Ch-Ch	Oy-Hy	-	-	6.4	36.2	13.7	70.3	15.1	93.0	12.6	85.1

Table 5.16: Standard deviation of hydrogen bond dynamics time constants (ps) derived from CMD simulations at 300K for 0, 5, 10, 20, and 33 mol% ChCl in Glycerol.

		0 mol%		5 mol%		10 mol%		20 mol%		33 mol%	
	site-site	τ_f	τ_b	τ_f	τ_b	τ_f	τ_b	τ_f	τ_b	τ_f	τ_b
Gly-Gly	Oc-Hc	4.8	11.4	5.2	15.3	4.9	11.3	6.7	24.2	5.8	13.6
	Oc-Ht	4.8	11.0	2.6	10.5	7.4	15.9	4.0	12.7	4.9	8.9
	Ot-Hc	4.3	10.7	2.9	7.3	6.0	13.4	5.8	8.6	4.9	14.3
	Ot-Ht	4.8	11.4	3.7	6.3	6.8	9.5	7.2	13.7	4.8	8.3
Cl-Gly	Cl-Hc	-	-	12.5	12.2	7.8	7.6	5.6	7.0	5.1	6.1
	Cl-Ht	-	-	11.2	7.4	9.7	6.6	9.9	6.3	8.7	5.2
Cl-Ch	Cl-Hy	-	-	23.3	24.0	22.2	24.9	5.9	7.5	4.8	4.3
Gly-Ch	Oc-Hy	-	-	6.6	20.5	3.3	12.9	4.4	9.5	1.9	4.3
	Ot-Hy	-	-	1.1	2.0	4.3	12.5	5.8	9.1	3.4	5.8
Ch-Gly	Oy-Hc	-	-	8.5	63.1	5.2	23.3	4.1	48.2	3.1	32.0
	Oy-Ht	-	-	5.6	99.5	1.7	77.7	3.7	51.8	2.4	45.1
Ch-Ch	Oy-Hy	-	-	3.3	16.6	5.5	18.7	3.0	18.3	2.0	11.8

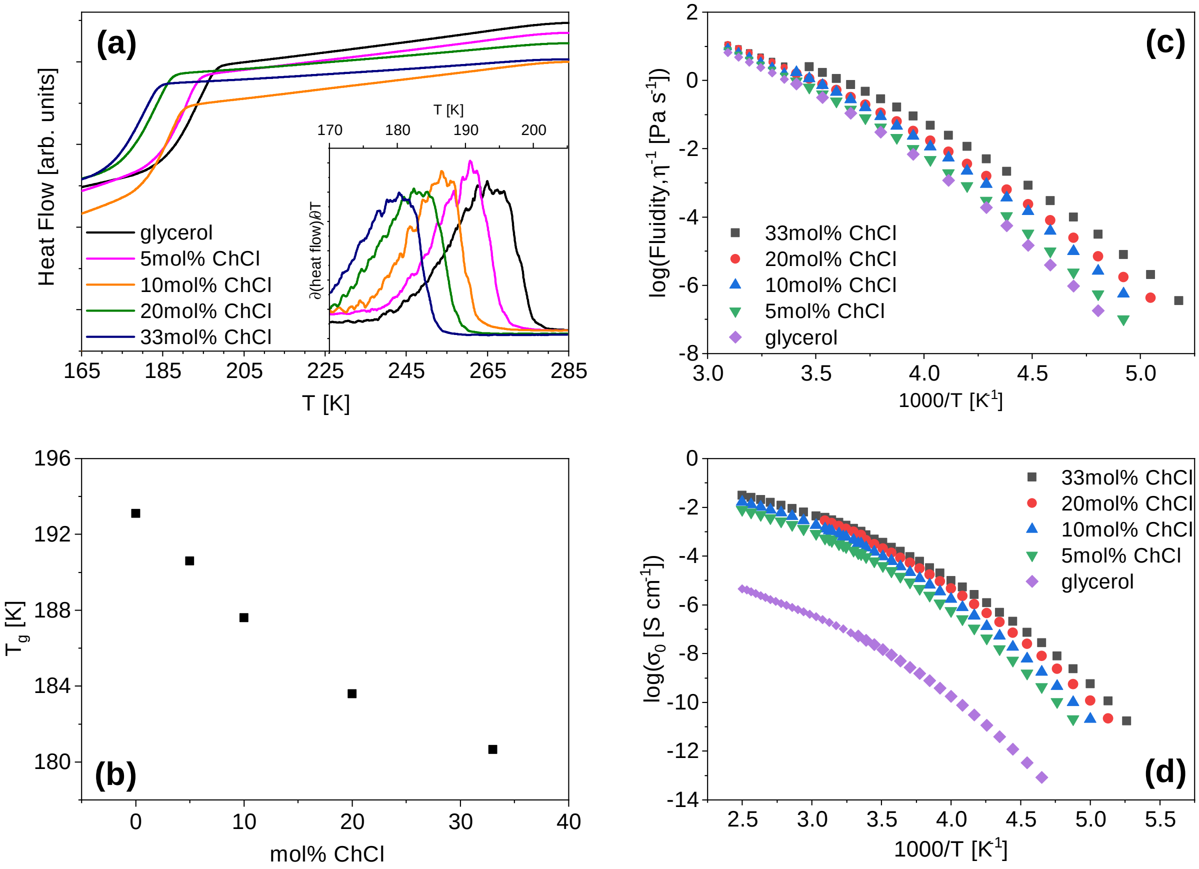

Figure 5.22: Physicochemical properties are enhanced in ChCl/glycerol mixtures as the eutectic composition is approached. (a) Heat flow plotted versus temperature for 0-33mol% ChCl for the cooling cycle obtained from DSC. Inset: The derivative of heat flow with respect to temperature plotted versus temperature. (b) Glass transition temperatures of the mixtures plotted versus the choline chloride concentration. (c) Fluidity, inverse viscosity, plotted versus inverse temperature for 0-33mol% ChCl in glycerol. Measurements below 298 K were obtained with the rheometer described in methods under DMS, and above 298 K were made with a viscometer. (d) Dc ionic conductivities of 0-33mol% ChCl in glycerol plotted versus inverse temperature.

al.,[223] with hydrogen bond criteria set to a HBA–HBD maximum angle deviation of 30°and a distance cutoff of the first minima for that interaction as listed in Table 5.4. This method allows for an understanding of timescales for both a forward and backward movement along a defined reaction coordinate. Forward movement is defined as hydrogen bond breaking and backward movement as hydrogen bond reformation with respective timescales of τ_f and τ_b. Forward movement can also be understood as the average hydrogen bond lifetime τ_{hb}, making τ_f and τ_{hb} equivalent in this definition. With these definitions in mind, the resultant forward and backward time constants for relevant HBA–HBD pairs are listed in Table 5.15. There is a reduction in both τ_f and τ_b in all pair-wise interactions with increasing ChCl save for Oy–Hy interactions that are not altered from the already low τ values (when considering the standard deviations provided in Table 5.16), indicating a marked increase in overall system fluidity with the addition of ChCl to glycerol, consistent with the trend in the rotational and translational dynamics. It is important to note the decrease in both the forward and backward time constants, as this implies an overall reduction in the activation energy of hydrogen bond dynamics rather than favoring only hydrogen bond breaking or reformation. It has been reported that the DES Ethaline has a higher viscosity than the corresponding pure HBD, EG,[224, 89] an opposite trend seen in Glyceline. In a recent study by Zhang *et al.*,[97] it was found that the hydrogen bonds between Cl and EG are much stronger than those between EG molecules and it was believed that these stronger Cl-EG interactions causes the increase in viscosity upon addition of ChCl to EG. This is supported by ^{1}H NMR data in Figure 5.3 as discussed earlier. The results in Table 5.15 show that, at low ChCl concentrations, the hydrogen bond lifetimes (or τ_f) for Cl-Hc are close to those of Oc-Hc and less than those of Ot-Ht. At high concentrations, Cl-Hc hydrogen bond lifetimes are less than those of both Oc-Hc and Ot-Hc. The hydrogen bond lifetime of Cl-Ht are slightly longer than those of Oc-Ht and Ot-Ht. These results suggest that the hydrogen bond interactions between Cl and glycerol are weaker or comparable to those between glycerol molecules.

5.4.3 Macroscopic Transport Properties and Emerging Picture

The increase in molecular mobility with the addition of ChCl noted in Figure 5.20a is consistent with the DSC data shown in Figure 5.22a and 5.22b, where a decrease in the glass transition temperature (T_{g}) is observed with increasing ChCl concentration. No melting or crystallization is observed in the DSC data, as all of these mixtures are glass-forming liquids. However, if the Lindeman's criterion for glass formers is valid such that $T_g \cong 2/3T_m$,[23] the melting and glass transition temperatures are expected to follow a similar trend. Increases in dc ionic conductivity and fluidity are also observed, as shown in Figures 5.22c and 5.22d. The dc ionic conductivity can be estimated by $\sigma_0 = \Sigma q_i \mu_i n_i$, where q is the charge, μ is the mobility, and n is the number density of charge carriers.[28] To a good approximation, the mobility of the ions is dominated by the structural dynamics of the matrix on which they are situated. Thus, faster structural relaxation rates would also imply a higher ionic conductivity. The mean structural relaxation rate is also directly related to fluidity by $\omega_\alpha \cong G_\infty \eta^{-1}$, where G_∞ is the high-frequency shear modulus.[26] This relationship qualitatively holds true since as ChCl concentration is increased, the mean relaxation rates and fluidity both increase. While these functional transport relationships hold at a qualitative level, these mixtures do not strictly obey the Stokes-Einstein equation. The Stokes-Einstein relation, which can be written as:

$$D = \frac{k_b\, T}{6\pi\eta r} \tag{5.9}$$

where D is the self-diffusion coefficient, k_b is the Boltzmann constant, T is temperature, η is viscosity, and r is radius. Using this, we can calculate what would be a constant $k_b/(6\pi r)$, if the relation held true. It is shown in Figure 5.23 that it does not hold true. This is not surprising since the moieties and local structures dominating the mass and charge transport are different.

Figure 5.24a displays a snapshot of 5mol% ChCl in glycerol, which shows that at this concentration the choline cations are "trapped" by the glycerol network. This result is captured in BDS, CMD simulations, and QENS which all indicate that the dynamics of choline is significantly slower than glycerol at the low ChCl concentrations. Depicted in

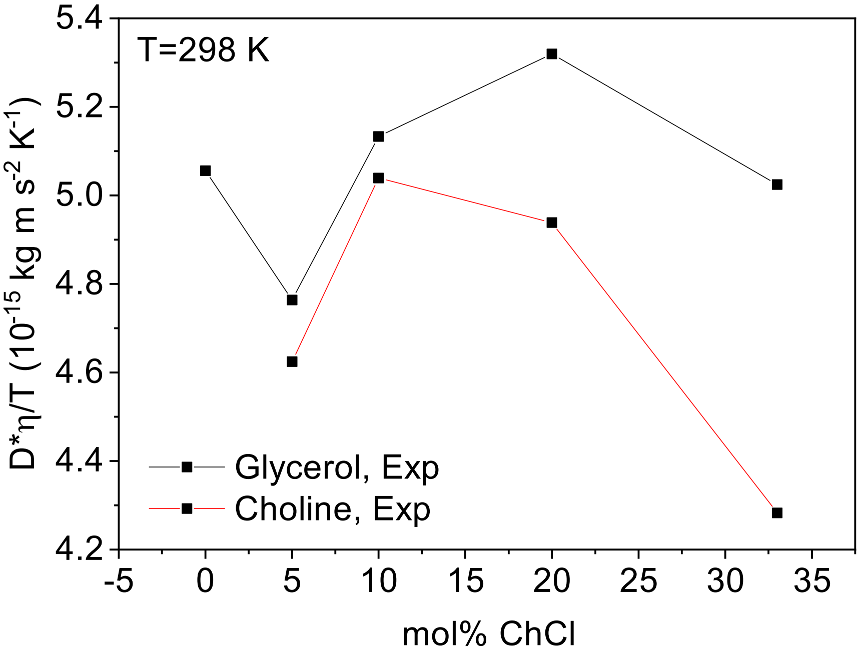

Figure 5.23: The self diffusion coefficient of choline and glycerol respectively multipled by viscosity divided by temperature at 298 K plotted versus mol% ChCl to test the Stokes-Einstein relation.

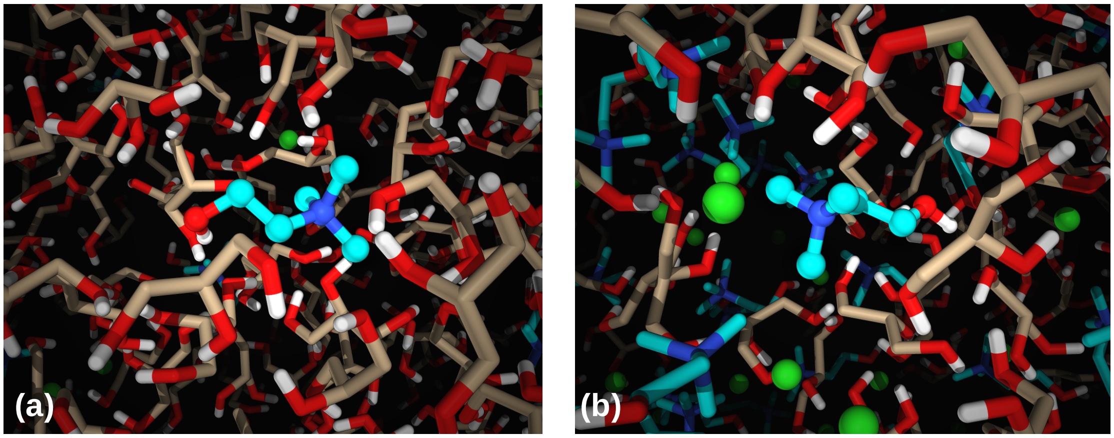

Figure 5.24: Snapshots of the environment of choline in 5 and 33mol% ChCl in glycerol. (a) Snapshot from a CMD simulation of slow reorienting choline in 5 mol% ChCl. The white-red-tan molecule represents glycerol and the hydrogen-oxygen-carbon atoms respectively. The white-red-aqua-blue molecule represents choline and the hydrogen-oxygen-carbon-nitrogen atoms respectively. The lime green molecule is the chloride anion. Choline is 'trapped' within homogeneous glycerol HBN. (b) Snapshot from a CMD simulation of fast reorienting choline in 33mol% ChCl. Heterogeneities of species and charge alternation weakens the HBN significantly, liberating choline cations to more easily reorient within the HBN.

Figure 5.24b, higher concentration of ions dispersed throughout the matrix results in a more heterogeneous system allowing for faster rotational and translational dynamics of the ionic species. All of these factors cumulatively result in a decreased T_g of the solvent. This is consistent with the results of orientational and translational dynamics studied.

5.5 Discussion

Several different experimental and computational techniques were used to investigate how the microscopic interactions and local structure evolve in ChCl/glycerol mixtures as the HBA concentration is increased in the HBD. Neat glycerol has an extensive, branched HBN.[221] As ChCl is added, it is observed from ^{1}H NMR, that chloride donates electron density to glycerol as the two begin interacting. Additionally, WANS supported by CMD and AIMD simulations show that these interactions alter and weaken the HBN of glycerol. This can be attributed to the finding that Gly–Cl interactions are similar, if not weaker, in strength than Gly–Gly interactions (Table 5.15). However, choline still strongly interacts with chloride at the eutectic composition, but does not significantly interact with glycerol, shown by N_{coord}. Overall, this creates local, structural heterogeneity, which weakens the HBN of glycerol and drastically increases solvent dynamics.

The dynamic mechanical spectra in Figure 5.18b suggests that glycerol mostly preserves much of its HBN even with 33mol% ChCl present, since the shapes of the structural relaxation and the slow mechanical relaxation, originally attributed to the HBN of glycerol, remain unchanged. This indicates that though ions are dispersed throughout the system and decrease glycerol self-interactions, the majority of glycerol molecules remain interconnected in some form. CMD simulations of dipole moment rotational correlation relaxation times and diffusion coefficients, QENS, and PFG-NMR revealed that choline rotates and diffuses slower than glycerol at all concentrations and timescales examined. This is because the glycerol HBN acts as a cage to choline, which is weakened as ChCl concentration is increased. The simulated dipole moment rotational correlation relaxation times in Figure 5.21a show that choline becomes faster relative to a fixed dynamic timescale of glycerol as ChCl concentration is increased, which is the same trend observed for the sub-α and α-dielectric relaxations, respectively, shown in Figure 5.20b. This, along with the coupling of the sub-α relaxation to ion dynamics shown in Figure 5.20c, indicates the sub-α dielectric relaxation is a reflection of the slow, rotational ion dynamics of choline in the DES, which are able to increase in rate as the system becomes more mobile.

The addition of ChCl to glycerol creates microscopic heterogeneities that are dispersed throughout the mixture. As ChCl concentration is increased up to the eutectic composition, the network becomes more heterogeneous, which weakens the HBN of glycerol thereby increasing the molecular mobility as observed from QENS, PFG-NMR, CMD simulations, and BDS. This presumably results in the characteristic depression in the glass transition temperature of Glyceline. In addition, since the transport and dynamic properties are coupled to the glass transition, the structural relaxation rates, fluidity, and conductivity all increase with ChCl concentration accordingly. These are direct results of the weakening, though not complete disruption, of the HBN of glycerol as ChCl is added. Thus, the evolution of microscopic heterogeneities and dynamics with increasing ChCl concentration is shown to correlate with the macroscopic transport properties in the ranges studied.

Chapter 6

Conclusions

The main focus in this dissertation is to provide fundamental insight into a class of alternative solvents, deep eutectic solvents, to help elucidate any structure-property relationships. In Chapter 1, several questions were outlined, as their answers are crucial in closing the knowledge gap for these materials. Now, after presenting the work in this dissertation, we return to these questions to answer them as definitively as possible with work we completed:

1. *Is the eutectic composition the optimal point for the most advantageous physicochemical properties?*

   There is no direct answer to this question based off of our results. In Chapter 4, we showed that for Ethaline, operating at the eutectic composition enhances the solvent and orientational dynamics as well as the ionic conductivity. Under or above the eutectic composition impairs the dynamics and diminishes the ionic conductivity. A previous study showed that the viscosity of ChCl/EG mixtures increases with increasing ChCl composition, up to 33mol% ChCl. We proposed that this discrepancy between properties is related to mechanical relaxation phenomena at lower frequencies relative to the primary structural relaxation, which contributes to the overall viscosity of these mixtures. In Chapter 5, we showed that all properties measured for Glyceline (T_g depression, solvent and orientational dynamics, fluidity, and ionic conductivity) are all enhanced up to the measured eutectic composition. It is unknown to what degree one should expect $\Delta T_g \propto \omega \propto \eta^{-1} \propto \sigma_0$ for DESs based on the current findings. Ideally, additional systems using HBDs that are aromatic based, amine based, etc. would be studied as well as more alcohols to determine the origin of this discrepancy between these two structurally similar DESs.

2. *Should the eutectic point be considered a single molar composition or a range of compositions?*

   Again, with Chapters 4 and 5 we have shown varying answers for this question. For Ethaline, we have shown that a small range from 15-20mol% ChCl in EG exists at the eutectic composition. For Glyceline, it appears that the eutectic point occurs at a single composition. However, both DESs exhibit a wide range of compositions for which a liquid exists at room temperature. Additionally, at higher temperatures, the properties are also comparable (between compositions of the same DES). We hypothesize that this answer varies depending on the chemical structure and therefore local structuring, dynamics, and interactions.

3. *How do the local structures and microscopic dynamics evolve with variation of composition of the mixtures approaching the eutectic concentration?*

   In both Glyceline and Ethaline, the dielectric spectra revealed a slow mode (relative to the structural relaxation) that, with CMD simulations, was linked to choline dynamics inhibited by the hydrogen bonded network of the HBD. While the orientational dynamics of choline remain slower than that of glycerol or EG at all compositions, the rate of the slow mode (choline dynamics) increases in rate relative to the structural relaxation (glycerol or EG) with increasing ChCl composition. Additionally, the rate of all components are increased with increasing ChCl composition up to the eutectic composition. Structurally, at low ChCl compositions, choline is trapped by the HBN of the HBD. As ChCl composition is increased, the system becomes more heterogeneous and dynamic, enhancing the rates of dynamics of all components, especially choline. In Glyceline, it was shown with PFG-NMR and CMD simulations that the the translational diffusion coefficient, D of glycerol is also faster than choline.

Furthermore, the CMD simulations classical molecular dynamics simulations revealed that chloride is the fastest component of all (D). In general, again, the motion of each component is enhanced with increasing ChCl up to the eutectic composition. These translational diffusion experiments were not completed with Ethaline, so it is unclear to what degree these conclusions could be universal.

4. *How do spatial and temporal heterogeneities influence the macroscopic properties?*

   The addition of ChCl was shown to create these spatial and temporal heterogeneities in the pre-existing hydrogen bonded network of the HBD. The preserved spectral shapes in the mechanical data of Glyceline revealed that glycerol largely maintains its hydrogen bonded network, but the introduced ChCl loosens or weaken the hydrogen bonded network, enhancing the rate of dynamics. Therefore, the $\mathrm{T_m}$ and/or $\mathrm{T_g}$ is also lowered, and the overall physicochemical properties including ionic conductivity an fluidity are enhanced. So, generally, the dynamic heterogeneities prove to be beneficial in improving the macroscopic properties and may even be a key parameter in formation of DESs.

6.1 Outlook

The DESs studied in this dissertation, while somewhat structurally similar, showed very different properties. Unfortunately, we know the relations described in Section 2.1 are not always valid, meaning that due the the complexities in the nature of DESs and the assumptions made to derive these relations, it cannot always be expected that $\eta^{-1} \propto \sigma_0 \propto \omega_\alpha$. Especially for electrolytes for electrochemical technologies, it is desirable for the fluidity and ionic conductivity to be highest at the same composition. The physical meaning of these discrepancies between properties has not been specifically answered within this dissertation, and should be a focus of future work after this. A proposed next line of work would be to obtain phase behavior, dielectric, and mechanical data at a wide range of compositions for a variety of DESs. There should be an emphasis on developing series with slight chemical structure variations so that changes observed can be quickly attributed to the specific modifications made. It should be pinpointed, if possible, what specific interactions, local structuring, or dynamic modes give rise to favored changes in the macroscopic properties. This will aid in the development of predictive knowledge for designing or tailoring DESs for specific applications.

Bibliography

[1] Liliana P. Silva, Luis Fernandez, Joao H.F. Conceiçao, Mónia A.R. Martins, Adriel Sosa, Juan Ortega, Simao P. Pinho, and Joao A.P. Coutinho. Design and Characterization of Sugar-Based Deep Eutectic Solvents Using Conductor-like Screening Model for Real Solvents. *ACS Sustainable Chemistry and Engineering*, 6(8):10724–10734, 8 2018. xii, 10, 19

[2] Benworth B Hansen, Stephanie Spittle, Brian Chen, Derrick Poe, Yong Zhang, Jeffrey M Klein, Alexandre Horton, Laxmi Adhikari, Tamar Zelovich, Brian W Doherty, Burcu Gurkan, Edward J Maginn, Arthur Ragauskas, Mark Dadmun, Thomas A Zawodzinski, Gary A Baker, Mark E Tuckerman, Robert F Savinell, and Joshua R Sangoro. Deep Eutectic Solvents: A Review of Fundamentals and Applications. *Chemical Reviews*, 121(3):1232–1285, 2021. xii, 12, 15, 17, 50

[3] Luiz S. Longo and Marcus V. Craveiro. Deep eutectic solvents as unconventional media for multicomponent reactions. *Journal of the Brazilian Chemical Society*, 29(10):1999–2025, 2018. xii, 14

[4] Liliana P Silva, Catarina F Araújo, Dinis O Abranches, Manuel Melle-Franco, Mónia A R Martins, Mariela M Nolasco, Paulo J A Ribeiro-Claro, Simão P Pinho, and João A P Coutinho. What a difference a methyl group makes-probing choline-urea molecular interactions through urea structure modification. *Physical Chemistry Chemical Physics*, 21(33):18278–18289, 2019. xii, 17, 19, 20

[5] Andrew P Abbott, Glen Capper, David L Davies, Raymond K Rasheed, and Vasuki Tambyrajah. Novel solvent properties of choline chloride/urea mixtures. *Chemical Communications*, (1):70–71, 2003. xii, 11, 20

[6] Supreet Kaur, Akshay Malik, and Hemant K. Kashyap. Anatomy of Microscopic Structure of Ethaline Deep Eutectic Solvent Decoded through Molecular Dynamics Simulations. *Journal of Physical Chemistry B*, 123(39):8291–8299, 10 2019. xii, 22, 23

[7] Carmine D'Agostino, Robert C Harris, Andrew P Abbott, Lynn F Gladden, and Mick D Mantle. Molecular motion and ion diffusion in choline chloride based deep eutectic solvents studied by 1H pulsed field gradient NMR spectroscopy. *Physical Chemistry Chemical Physics*, 13(48):21383, 2011. xiii, 23, 24, 71

[8] César Leyva-Porras, Pedro Cruz-Alcantar, Vicente Espinosa-Solís, Eduardo Martínez-Guerra, Claudia I. Piñón-Balderrama, Isaac Compean Martínez, and María Z. Saavedra-Leos. Application of Differential Scanning Calorimetry (DSC) and Modulated Differential Scanning Calorimetry (MDSC) in Food and Drug Industries. *Polymers 2020, Vol. 12, Page 5*, 12(1):5, 12 2019. xiii, 28

[9] Avraam I. Isayev. Encyclopedia of Polymer Blends, Volume 3: Structure. *Encyclopedia of Polymer Blends*, 7 2016. xiii, 28

[10] F Kremer and A Schönhals. *Broadband dielectric spectroscopy*. Springer, 2003. xiii, 6, 45, 103, 106

[11] Kwan Chi Kao. *Dielectric Phenomena in Solids*. Elsevier Inc., l edition, 2004. xiii, 47

[12] Coby J. Clarke, Wei Chien Tu, Oliver Levers, Andreas Bröhl, and Jason P. Hallett. Green and Sustainable Solvents in Chemical Processes. *Chemical Reviews*, 118(2):747–800, 1 2018. 1, 9

[13] Jack C. Griffis. Design. *Shape-Memory Polymer Device Design*, pages 23–75, 1 2017. 6

[14] S. S. Schoenholz, E. D. Cubuk, D. M. Sussman, E. Kaxiras, and A. J. Liu. A structural approach to relaxation in glassy liquids. *Nature Physics 2016 12:5*, 12(5):469–471, 2 2016. 6

[15] Xiang Zhang and Mark Cresswell. Materials Fundamentals of Drug Controlled Release. *Inorganic Controlled Release Technology*, pages 17–55, 1 2016. 6

[16] Friedrich Kremer and Alois Loidl. *The Scaling of Relaxation Processes*. Springer, 2018. 6, 103

[17] H Vogel. The temperature dependence law of the viscosity of fluids. *Physikalische Zeitschrift*, 22:645–646, 1921. 7

[18] Gordon S Fulcher. Analysis of Recent Measurements of the Viscosity of Glasses. *Journal of the American Ceramic Society*, 8(6):339–355, 1925. 7

[19] G. Tammann and W. Hesse. Die Abhängigkeit der Viscosität von der Temperatur bie unterkühlten Flüssigkeiten. *Zeitschrift für anorganische und allgemeine Chemie*, 156(1):245–257, 10 1926. 7

[20] Maciej Galiński, Andrzej Lewandowski, and Izabela Stepniak. Ionic liquids as electrolytes. *Electrochimica Acta*, 51(26):5567–5580, 8 2006. 7

[21] Rita Craveiro, Ivo Aroso, V Flammia, Tânia Carvalho, Maria Teresa Viciosa, Madalena Dionísio, Susana Barreiros, Rui L Reis, Ana Rita C Duarte, and Alexandre Paiva. Properties and thermal behavior of natural deep eutectic solvents. *J. Molec. Liq.*, 215:534–540, 2016. 7, 13

[22] Joshua R. Sangoro and Friedrich Kremer. Charge transport and glassy dynamics in ionic liquids. *Accounts of Chemical Research*, 45(4):525–532, 4 2012. 7

[23] F. Lindemann. The calculation of molecular natural frequencies. *Physikalische Zeitschrift*, 11:609–612, 1910. 7, 67, 116

[24] Rob Zondervan, Florian Kulzer, Gregorius C.G. Berkhout, and Michel Orrit. Local viscosity of supercooled glycerol near Tg probed by rotational diffusion of ensembles and single dye molecules. *Proceedings of the National Academy of Sciences of the United States of America*, 104(31):12628–12633, 7 2007. 7

[25] James Clerk Maxwell. IV. On the dynamical theory of gases. *Philosophical Transactions of the Royal Society of London*, 157:49–88, 12 1867. 7

[26] D M Heyes, E R Smith, and D Dini. Shear stress relaxation and diffusion in simple liquids by molecular dynamics simulations: Analytic expressions and paths to viscosity. *Journal of Chemical Physics*, 150(17):174504, 2019. 7, 116

[27] J. R. Sangoro, C. Iacob, A. Serghei, C. Friedrich, and F. Kremer. Universal scaling of charge transport in glass-forming ionic liquids. *Physical Chemistry Chemical Physics*, 11(6):913–916, 1 2009. 7

[28] J R Sangoro, A Serghei, S Naumov, P Galvosas, J Kärger, C Wespe, F Bordusa, and F Kremer. Charge transport and mass transport in imidazolium-based ionic liquids. *Physical Review E - Statistical, Nonlinear, and Soft Matter Physics*, 77(5), 2008. 8, 116

[29] M A Islam. Einstein-Smoluchowski Diffusion Equation: A Discussion. Technical report, 2004. 8, 112

[30] Shiladitya Sengupta and Smarajit Karmakar. Distribution of diffusion constants and Stokes-Einstein violation in supercooled liquids. *The Journal of Chemical Physics*, 140(22):224505, 6 2014. 8

[31] Jennifer A. Hodgdon and Frank H. Stillinger. Stokes-Einstein violation in glass-forming liquids. *Physical Review E*, 48(1):207, 7 1993. 8

[32] Takeshi Kawasaki and Hajime Tanaka. Apparent violation of the fluctuation-dissipation theorem due to dynamic heterogeneity in a model glass-forming liquid. *Physical Review Letters*, 102(18):185701, 5 2009. 8

[33] Anu Hardenia, Neha Maheshwari, Shiv Shankar Hardenia, Sunil Kumar Dwivedi, Rahul Maheshwari, and Rakesh K. Tekade. Scientific Rationale for Designing Controlled Drug Delivery Systems. *Basic Fundamentals of Drug Delivery*, pages 1–28, 1 2019. 8

[34] S. S. Devi and H. M. Mehendale. Academy of Toxicological Sciences. *Encyclopedia of Toxicology: Third Edition*, page 7, 1 2014. 8

[35] Mohammed Harun Chakrabarti, Farouq Sabri Mjalli, Inas Muen Alnashef, Mohd Ali Hashim, Mohd Azlan Hussain, Laleh Bahadori, and Chee Tong John Low. Prospects of applying ionic liquids and deep eutectic solvents for renewable energy storage by means of redox flow batteries. *Renewable and Sustainable Energy Reviews*, 30:254–270, 2014. 8

[36] James H. Clark, Thomas J. Farmer, Andrew J. Hunt, and James Sherwood. Opportunities for bio-based solvents created as petrochemical and fuel products transition towards renewable resources. *International Journal of Molecular Sciences*, 16(8):17101–17159, 7 2015. 8

[37] Ketan T. Savjani, Anuradha K. Gajjar, and Jignasa K. Savjani. Drug Solubility: Importance and Enhancement Techniques. *ISRN Pharmaceutics*, 2012:1–10, 7 2012. 8

[38] Muhammad Shahzad Kamal, Shaikh A. Razzak, and Mohammad M. Hossain. Catalytic oxidation of volatile organic compounds (VOCs) - A review. *Atmospheric Environment*, 140:117–134, 2016. 9

[39] Neil Winterton. The green solvent: a critical perspective. *Clean Technologies and Environmental Policy 2021 23:9*, 23(9):2499–2522, 9 2021. 9

[40] Christian Capello, Ulrich Fischer, and Konrad Hungerbühler. What is a green solvent? A comprehensive framework for the environmental assessment of solvents. *Green Chemistry*, 9(9):927–93, 2007. 9

[41] Tyler Cosby, Zachariah Vicars, Yangyang Wang, and Joshua Sangoro. Dynamic-Mechanical and Dielectric Evidence of Long-Lived Mesoscale Organization in Ionic Liquids. *Journal of Physical Chemistry Letters*, 8(15):3544–3548, 2017. 9, 11

[42] Di Wei and Ari Ivaska. Applications of ionic liquids in electrochemical sensors. *Analytica Chimica Acta*, 607(2):126–135, 1 2008. 9

[43] Paul Walden. Über die Molekulargrösse und elektrische Leitfähigkeit einiger geschmolzener Salze. *Bulletin de l'Académie impériale des sciences de St.-Pétersbourg*, 8(405-422), 1914. 9

[44] Tom Welton. Ionic liquids: a brief history. *Biophysical Reviews*, 10(3):691–706, 2018. 9

[45] Leslie Glasser. Lattice and phase transition thermodynamics of ionic liquids. *Thermochimica Acta*, 421(1-2):87–93, 2004. 9

[46] John Bright Ferguson. The melting and freezing point of sodium chloride. *Journal of Physical Chemistry*, 26(7):626–630, 1922. 9

[47] John S. Wilkes. A short history of ionic liquids - From molten salts to neoteric solvents. *Green Chemistry*, 4(2):73–80, 2002. 9

[48] A. Berthod, M. J. Ruiz-Ángel, and S. Carda-Broch. Recent advances on ionic liquid uses in separation techniques. *Journal of Chromatography A*, 1559:2–16, 7 2018. 9

[49] C. Austen Angell, Younes Ansari, and Zuofeng Zhao. Ionic Liquids: Past, present and future. *Faraday Discussions*, 154(0):9–27, 11 2012. 9

[50] Robert Hayes, Gregory G. Warr, and Rob Atkin. Structure and Nanostructure in Ionic Liquids. *Chemical Reviews*, 115(13):6357–6426, 7 2015. 9

[51] Natalia V Plechkova and Kenneth R Seddon. Applications of ionic liquids in the chemical industry. *Chemical Society Reviews*, 37(1):123–150, 2008. 9

[52] Seema Singh, Blake A. Simmons, and Kenneth P. Vogel. Visualization of biomass solubilization and cellulose regeneration during ionic liquid pretreatment of switchgrass. *Biotechnology and Bioengineering*, 104(1):68–75, 9 2009. 9

[53] Nawshad Muhammad, Zakaria Man, Mohamad Azmi Bustam, M. I.Abdul Mutalib, Cecilia D. Wilfred, and Sikander Rafiq. Dissolution and delignification of bamboo biomass using amino acid-based ionic liquid. *Applied Biochemistry and Biotechnology*, 165(3-4):998–1009, 10 2011. 9

[54] Piyarat Weerachanchai, Susanna Su Jan Leong, Matthew Wook Chang, Chi Bun Ching, and Jong Min Lee. Improvement of biomass properties by pretreatment with ionic liquids for bioconversion process. *Bioresource Technology*, 111:453–459, 5 2012. 9

[55] Luísa A. Neves, Carlos Afonso, Isabel M. Coelhoso, and João G. Crespo. Integrated CO 2 capture and enzymatic bioconversion in supported ionic liquid membranes. *Separation and Purification Technology*, 97:34–41, 9 2012. 11

[56] Darinel Valencia-Marquez, Antonio Flores-Tlacuahuac, and Ruben Vasquez-Medrano. An optimization approach for CO2 capture using ionic liquids. *Journal of Cleaner Production*, 168:1652–1667, 12 2017. 11

[57] Jian Gang Lu, Xiang Li, Yun Xia Zhao, Hong Lu Ma, Li Fan Wang, Xin Yi Wang, Yu Fan Yu, Ting Yu Shen, Hao Xu, and Yu Ting Zhang. CO2 capture by ionic liquid membrane absorption for reduction of emissions of greenhouse gas. *Environmental Chemistry Letters*, 17(2):1031–1038, 6 2019. 11

[58] Bencai Lin, Hui Shang, Fuqiang Chu, Yurong Ren, Ningyi Yuan, Baoping Jia, Shuai Zhang, Xiaomin Yu, Yingqiang Wei, and Jianning Ding. Ionic liquid-tethered Graphene Oxide/Ionic Liquid Electrolytes for Highly Efficient Dye Sensitized Solar Cells. *Electrochimica Acta*, 134:209–214, 7 2014. 11

[59] Lei Guo, Xu Pan, Changneng Zhang, Weiqing Liu, Meng Wang, Xiaqin Fang, and Songyuan Dai. Ionic liquid electrolyte based on S-propyltetrahydrothiophenium iodide for dye-sensitized solar cells. *Solar Energy*, 84(3):373–378, 3 2010. 11

[60] Yanyan Fang, Wanchun Xiang, Xiaowen Zhou, Yuan Lin, and Shibi Fang. High-performance novel acidic ionic liquid polymer/ionic liquid composite polymer electrolyte for dye-sensitized solar cells. *Electrochemistry Communications*, 13(1):60–63, 1 2011. 11

[61] Serpil Denizalti, Abdulrahman Khalaf Ali, Çağatay Ela, Mesut Ekmekci, and Sule Erten-Ela. Dye-sensitized solar cells using ionic liquids as redox mediator. *Chemical Physics Letters*, 691:373–378, 1 2018. 11

[62] Ali Karout and Alain C. Pierre. Silica gelation catalysis by ionic liquids. *Catalysis Communications*, 10(4):359–361, 1 2009. 11

[63] Christian P. Mehnert, Raymond A. Cook, Nicholas C. Dispenziere, and Edmund J. Mozeleski. Biphasic hydroformylation catalysis in ionic liquid media. *Polyhedron*, 23(17 SPEC.ISS.):2679–2688, 11 2004. 11

[64] Charles M. Gordon. New developments in catalysis using ionic liquids. *Applied Catalysis A: General*, 222(1-2):101–117, 12 2001. 11

[65] Iwona Cichowska-Kopczyńska, Monika Joskowska, Bartosz Debski, Robert Aranowski, and Jan Hupka. Separation of toluene from gas phase using supported imidazolium ionic liquid membrane. *Journal of Membrane Science*, 566:367–373, 11 2018. 11

[66] Pablo Navarro, Antonio Ovejero-Pérez, Miguel Ayuso, Noemí Delgado-Mellado, Marcos Larriba, Julián García, and Francisco Rodríguez. Cyclohexane/cyclohexene separation by extractive distillation with cyano-based ionic liquids. *Journal of Molecular Liquids*, 289:111120, 9 2019. 11

[67] Fan Yang, Fukiko Kubota, Yuzo Baba, Noriho Kamiya, and Masahiro Goto. Selective extraction and recovery of rare earth metals from phosphor powders in waste

fluorescent lamps using an ionic liquid system. *Journal of Hazardous Materials*, 254-255(1):79–88, 6 2013. 11

[68] Zihao Wang, Zhen Song, and Teng Zhou. Machine Learning for Ionic Liquid Toxicity Prediction. *Processes 2021, Vol. 9, Page 65*, 9(1):65, 12 2020. 11

[69] Maria V.S. Oliveira, Bruna T. Vidal, Claudia M. Melo, Rita de C.M. de Miranda, Cleide M.F. Soares, João A.P. Coutinho, Sónia P.M. Ventura, Silvana Mattedi, and Álvaro S. Lima. (Eco)toxicity and biodegradability of protic ionic liquids. *Chemosphere*, 147:460–466, 3 2016. 11

[70] Dongbin Zhao, Yongcheng Liao, and Ziding D Zhang. Toxicity of ionic liquids. *Clean - Soil, Air, Water*, 35(1):42–48, 2007. 11

[71] Sebastian Werner, Marco Haumann, and Peter Wasserscheid. Ionic Liquids in Chemical Engineering. *Annual Review of Chemical and Biomolecular Engineering*, 1:203–230, 2010. 11

[72] Dzmitry H. Zaitsau, Andrei V. Yermalayeu, Sergey P. Verevkin, Jason E. Bara, and Alexander D. Stanton. Structure-property relationships in ionic liquids: A study of the influence of N(1) Ether and C(2) methyl substituents on the vaporization enthalpies of imidazolium-based ionic liquids. *Industrial and Engineering Chemistry Research*, 52(47):16615–16621, 2013. 11

[73] Tamar L. Greaves and Calum J. Drummond. Protic Ionic Liquids: Evolving Structure-Property Relationships and Expanding Applications. *Chemical Reviews*, 115(20):11379–11448, 2015. 11

[74] Vishwesh Venkatraman, Sigvart Evjen, Hanna K. Knuutila, Anne Fiksdahl, and Bjørn Kåre Alsberg. Predicting ionic liquid melting points using machine learning. *Journal of Molecular Liquids*, 264:318–326, 8 2018. 11

[75] Henni Vanda, Yuntao Dai, Erica G. Wilson, Robert Verpoorte, and Young Hae Choi. Green solvents from ionic liquids and deep eutectic solvents to natural deep eutectic solvents. *Comptes Rendus Chimie*, 21(6):628–638, 6 2018. 11

[76] Emma L Smith, Andrew P Abbott, and Karl S Ryder. Deep Eutectic Solvents (DESs) and Their Applications. *Chemical Reviews*, 114(21):11060–11082, 2014. 13, 70

[77] Dinis O. Abranches and João A.P. Coutinho. Type V deep eutectic solvents: Design and applications. *Current Opinion in Green and Sustainable Chemistry*, 35, 6 2022. 13

[78] Tracy El Achkar, Hélène Greige-Gerges, and Sophie Fourmentin. Basics and properties of deep eutectic solvents: a review. *Environmental Chemistry Letters*, 19(4):3397–3408, 8 2021. 13

[79] Pei Xu, Gao-Wei Zheng, Min-Hua Zong, Ning Li, and Wen-Yong Lou. Recent progress on deep eutectic solvents in biocatalysis. *Bioresources and Bioprocessing*, 4(1):34, 12 2017. 13, 70

[80] Alexandre Paiva, Rita Craveiro, Ivo Aroso, Marta Martins, Rui L Reis, and Ana Rita C Duarte. Natural deep eutectic solvents - Solvents for the 21st century. *ACS Sustainable Chemistry and Engineering*, 2(5):1063–1071, 2014. 13, 70

[81] Madhur Babu Singh, Vaishnu S. Kumar, Mansi Chaudhary, and Prashant Singh. A mini review on synthesis, properties and applications of deep eutectic solvents. *Journal of the Indian Chemical Society*, 98(11):100210, 11 2021. 13

[82] Baokun Tang and Kyung Ho Row. Recent developments in deep eutectic solvents in chemical sciences. *Monatshefte fur Chemie*, 144(10):1427–1454, 2013. 13

[83] Adeeb Hayyan, Farouq S. Mjalli, Inas M. Alnashef, Yahya M. Al-Wahaibi, Talal Al-Wahaibi, and Mohd Ali Hashim. Glucose-based deep eutectic solvents: Physical properties. *Journal of Molecular Liquids*, 178:137–141, 2 2013. 13, 17

[84] Irfan Wazeer, Maan Hayyan, and Mohamed K Hadj-Kali. Deep eutectic solvents: designer fluids for chemical processes. *Journal of Chemical Technology and Biotechnology*, 93(4):945–958, 2018. 13, 50

[85] I V Zinov'eva, A Ya Fedorov, N A Milevskii, Yu A Zakhodyaeva, and A A Voshkin. A Deep Eutectic Solvent Based on Choline Chloride and Sulfosalicylic Acid: Properties and Applications. *Theoretical Foundations of Chemical Engineering*, 55(3):371–379, 2021. 13, 18

[86] Mónia A R Martins, Simão P Pinho, and João A P Coutinho. Insights into the Nature of Eutectic and Deep Eutectic Mixtures. *Journal of Solution Chemistry*, 48(7):962–982, 2019. 13

[87] Chandrakant Mukesh, Rajeev Gupta, Divesh N Srivastava, Sanna Kotrappanavar Nataraj, and Kamalesh Prasad. Preparation of a natural deep eutectic solvent mediated self polymerized highly flexible transparent gel having super capacitive behaviour. *RSC Advances*, 6(34):28586–28592, 2016. 13

[88] Nadia Guajardo, Christoph R Müller, Rodrigo Schrebler, Carlos Carlesi, and Pablo Domínguez De María. Deep Eutectic Solvents for Organocatalysis, Biotransformations, and Multistep Organocatalyst/Enzyme Combinations. *ChemCatChem*, 8(6):1020–1027, 2016. 13, 50

[89] Farouq S. Mjalli and Jamil Naser. Viscosity model for choline chloride-based deep eutectic solvents. *Asia-Pacific Journal of Chemical Engineering*, 10(2):273–281, 3 2015. 13, 115

[90] Laleh Bahadori, Ninie Suhana Abdul Manan, Mohammed Harun Chakrabarti, Mohd Ali Hashim, Farouq Sabri Mjalli, Inas Muen Alnashef, Mohd Azlan Hussain, and Chee Tong John Low. The electrochemical behaviour of ferrocene in deep eutectic solvents based on quaternary ammonium and phosphonium salts. *Physical Chemistry Chemical Physics*, 15(5):1707–1714, 2013. 13

[91] Ahmed El-Banbi, Ahmed Alzahabi, and Ahmed El-Maraghi. Dry Gases. *PVT Property Correlations*, pages 29–63, 1 2018. 17

[92] Zhendi Wang, Merv Fingas, Chun Yang, and Jan H. Christensen. Crude Oil and Refined Product Fingerprinting: Principles. *Environmental Forensics: Contaminant Specific Guide*, pages 339–407, 1 1964. 17

[93] Harry Dembicki, Jr. and Harry Dembicki, Jr. *Chapter 5 – Reservoir Geochemistry*. Elsevier, 2017. 17

[94] Kishant Kumar, Anand Bharti, and Rudra Kumar. Molecular insight into the structure and dynamics of LiTf2N/deep eutectic solvent: an electrolyte for Li-ion batteries. *Molecular Simulation*, 47(18):1477–1492, 2021. 17

[95] A. A. Kityk, F. I. Danilov, V. S. Protsenko, V. Pavlik, M. Boča, and Y. Halahovets. Electropolishing of two kinds of bronze in a deep eutectic solvent (Ethaline). *Surface and Coatings Technology*, 397:126060, 9 2020. 17

[96] F. I. Danilov, A. A. Kityk, D. A. Shaiderov, D. A. Bogdanov, S. A. Korniy, and V. S. Protsenko. Electrodeposition of Ni–TiO2 Composite Coatings Using Electrolyte Based on a Deep Eutectic Solvent. *Surface Engineering and Applied Electrochemistry 2019 55:2*, 55(2):138–149, 5 2019. 17

[97] Yong Zhang, Derrick Poe, Luke Heroux, Henry Squire, Brian W Doherty, Zhuoran Long, Mark Dadmun, Burcu Gurkan, Mark E Tuckerman, and Edward J Maginn. Liquid Structure and Transport Properties of the Deep Eutectic Solvent Ethaline. *Journal of Physical Chemistry B*, 124(25):5251–5264, 2020. 17, 65, 74, 95, 115

[98] H. M.N.H. Irving and R. B. Simpson. The viscosity of mixtures of benzene and methanol. *Journal of Inorganic and Nuclear Chemistry*, 34(7):2241–2247, 7 1972. 17

[99] Carolin Ruß and Burkhard König. Low melting mixtures in organic synthesis - An alternative to ionic liquids? *Green Chemistry*, 14(11):2969–2982, 2012. 18

[100] Q Xu, L Y Qin, Y N Ji, P K Leung, H N Su, F Qiao, W W Yang, A A Shah, and H M Li. A deep eutectic solvent (DES) electrolyte-based vanadium-iron redox flow battery enabling higher specific capacity and improved thermal stability. *Electrochimica Acta*, 293:426–431, 2019. 18, 50

[101] David Lloyd, Tuomas Vainikka, and Kyösti Kontturi. The development of an all copper hybrid redox flow battery using deep eutectic solvents. *Electrochimica Acta*, 100:18–23, 2013. 18, 50, 70

[102] Qinghua Zhang, Karine De Oliveira Vigier, Sébastien Royer, and François Jérôme. Deep eutectic solvents: Syntheses, properties and applications. *Chemical Society Reviews*, 41(21):7108–7146, 2012. 18, 51, 70

[103] Andrew P. Abbott. Model for the conductivity of ionic liquids based on an infinite dilution of holes. *ChemPhysChem*, 6(12):2502–2505, 12 2005. 18

[104] Dinis O Abranches, Liliana P Silva, Mónia A R Martins, Simão P Pinho, and João A P Coutinho. Understanding the Formation of Deep Eutectic Solvents: Betaine as a Universal Hydrogen Bond Acceptor. *ChemSusChem*, 13(18):4916–4921, 2020. 18

[105] Dinis O. Abranches, Marcos Larriba, Liliana P. Silva, Manuel Melle-Franco, José F. Palomar, Simão P. Pinho, and João A.P. Coutinho. Using COSMO-RS to design choline chloride pharmaceutical eutectic solvents. *Fluid Phase Equilibria*, 497:71–78, 10 2019. 19

[106] Simone Di Muzio, Olga Russina, Dario Mastrippolito, Paola Benassi, Leucio Rossi, Annalisa Paolone, and Fabio Ramondo. Mixtures of choline chloride and tetrabutylammonium bromide with imidazole as examples of deep eutectic solvents: their structure by theoretical and experimental investigation. *Journal of Molecular Liquids*, 352:118427, 4 2022. 21

[107] Yong Zhang, Henry Squire, Burcu Gurkan, and Edward J Maginn. Refined Classical Force Field for Choline Chloride and Ethylene Glycol Mixtures over Wide Composition Range. *Journal of Chemical {\&} Engineering Data*, 2022(20):16, 2022. 21, 65, 67

[108] Caroline Velez and Orlando Acevedo. Simulation of deep eutectic solvents: Progress to promises. *Wiley Interdisciplinary Reviews: Computational Molecular Science*, 12(4):e1598, 7 2022. 21

[109] Oliver S Hammond, Daniel T Bowron, and Karen J Edler. Liquid structure of the choline chloride-urea deep eutectic solvent (reline) from neutron diffraction and atomistic modelling. *Green Chemistry*, 18(9):2736–2744, 2016. 21, 70, 106

[110] Supreet Kaur, Aditya Gupta, and Hemant K Kashyap. Nanoscale Spatial Heterogeneity in Deep Eutectic Solvents. *Journal of Physical Chemistry B*, 120(27):6712–6720, 2016. 21, 71

[111] Biswajit Guchhait, Suman Das, Snehasis Daschakraborty, and Ranjit Biswas. Interaction and dynamics of (alkylamide + electrolyte) deep eutectics: Dependence on alkyl chain-length, temperature, and anion identity. *The Journal of Chemical Physics*, 140(10):104514, 3 2014. 21

[112] Ryan Stefanovic, Michael Ludwig, Grant B Webber, Rob Atkin, and Alister J Page. Nanostructure, hydrogen bonding and rheology in choline chloride deep eutectic solvents as a function of the hydrogen bond donor. *Physical Chemistry Chemical Physics*, 19(4):3297–3306, 2017. 21, 106

[113] A Faraone, D V Wagle, G A Baker, E C Novak, M Ohl, D Reuter, P Lunkenheimer, A Loidl, and E Mamontov. Glycerol Hydrogen-Bonding Network Dominates Structure and Collective Dynamics in a Deep Eutectic Solvent. *Journal of Physical Chemistry B*, 122(3):1261–1267, 2018. 21, 23, 103, 106, 109

[114] Alasdair W. Taylor, Peter Licence, and Andrew P. Abbott. Non-classical diffusion in ionic liquids. *Physical Chemistry Chemical Physics*, 13(21):10147–10154, 5 2011. 23

[115] Daniel Reuter, Catharina Binder, Peter Lunkenheimer, and Alois Loidl. Ionic conductivity of deep eutectic solvents: the role of orientational dynamics and glassy freezing. *Physical Chemistry Chemical Physics*, 21(13):6801–6809, 2019. 25, 109

[116] Kallol Mukherjee, Anuradha Das, Samiran Choudhury, Anjan Barman, and Ranjit Biswas. Dielectric Relaxations of (Acetamide + Electrolyte) Deep Eutectic Solvents in the Frequency Window, $0.2 \leq \text{v/GHz} \leq 50$: Anion and Cation Dependence. *Journal of Physical Chemistry B*, 119(25):8063–8071, 2015. 25

[117] Durgesh V Wagle, Hua Zhao, and Gary A Baker. Deep eutectic solvents: Sustainable media for nanoscale and functional materials. *Accounts of Chemical Research*, 47(8):2299–2308, 2014. 25, 50, 70

[118] Satya N Tripathy, Zaneta Wojnarowska, Justyna Knapik, Hideaki Shirota, Ranjit Biswas, and Marian Paluch. Glass transition dynamics and conductivity scaling in ionic deep eutectic solvents: The case of (acetamide + lithium nitrate/sodium thiocyanate) melts. *Journal of Chemical Physics*, 142(18):184504, 2015. 25

[119] Juriti Rajbangshi, Kallol Mukherjee, and Ranjit Biswas. Heterogeneous Orientational Relaxations and Translation-Rotation Decoupling in (Choline Chloride + Urea) Deep Eutectic Solvents: Investigation through Molecular Dynamics Simulations and Dielectric Relaxation Measurements. *Journal of Physical Chemistry B*, 125(22):5920–5936, 6 2021. 25

[120] Carmine D'Agostino, Lynn F Gladden, Mick D Mantle, Andrew P Abbott, B Essa, I Ahmed, Azhar Y M Al-Murshedi, and Robert C Harris. Molecular and ionic diffusion in aqueous-deep eutectic solvent mixtures: probing inter-molecular interactions using PFG NMR. *Phys. Chem. Chem. Phys*, 17:15297, 2015. 25, 84

[121] Emmett S. Watson and Michael J. O'neill. Differential microcalorimeter, 4 1962. 27

[122] Pooria Gill, Tahereh Tohidi Moghadam, and Bijan Ranjbar. Differential Scanning Calorimetry Techniques: Applications in Biology and Nanoscience. *Journal of Biomolecular Techniques : JBT*, 21(4):167, 12 2010. 29

[123] A Franck. Viscoelasticity and dynamic mechanical testing A. Franck, TA Instruments Germany. Technical report. 30

[124] Danton Gutierrez-Lemini. *Engineering viscoelasticity*. PhD thesis, 2014. 35

[125] Pouria Hajikarimi and Fereidoon Moghadas Nejad. Mechanical models of viscoelasticity. *Applications of Viscoelasticity*, pages 27–61, 2021. 35

[126] C Gainaru, M Wikarek, S Pawlus, M Paluch, R Figuli, M Wilhelm, T Hecksher, B Jakobsen, J C Dyre, and R Böhmer. Oscillatory shear and high-pressure dielectric study of 5-methyl-3-heptanol. 35, 82

[127] P. Debye. *Polar Molecules*. Chemical Catalog Co., Inc., New York, 1929. 42, 60

[128] P. Debye. Zur Theorie der spezifischen Wärmen. *Annalen der Physik*, 344(14):789–839, 1 1912. 42

[129] Pierre Van Rysselberghe. Remarks concerning the clausius-mossotti law. *Journal of Physical Chemistry*, 36(4):1152–1155, 1932. 42

[130] Lars Onsager. Electric Moments of Molecules in Liquids. *Journal of the American Chemical Society*, 58(8):1486–1493, 8 1936. 42

[131] John G. Kirkwood. The Dielectric Polarization of Polar Liquids. *The Journal of Chemical Physics*, 7:911, 12 1939. 42

[132] H. Fröhlich. General theory of the static dielectric constant. *Transactions of the Faraday Society*, 44:238–243, 1 1948. 42

[133] Alexander Lukichev. Physical meaning of the stretched exponential Kohlrausch function. *Physics Letters A*, 383(24):2983–2987, 8 2019. 44

[134] Wei Wang and Duu Jong Lee. Lignocellulosic biomass pretreatment by deep eutectic solvents on lignin extraction and saccharification enhancement: A review. *Bioresource Technology*, 339:960–8524, 2021. 50

[135] Payam Kalhor and Khashayar Ghandi. Deep eutectic solvents as catalysts for upgrading biomass. *Catalysts*, 11(2):1–32, 2021. 50

[136] Yu-Loong Loow, Eng Kein New, Ge Hoa Yang, Lin Yang Ang, Luther Yang Wei Foo, and Ta Yeong Wu. Potential use of deep eutectic solvents to facilitate lignocellulosic biomass utilization and conversion. *Cellulose*, 24(9):3591–3618, 2017. 50

[137] Henrik Palmelund, Martin P Andersson, Camilla J Asgreen, Ben J Boyd, Jukka Rantanen, and Korbinian Löbmann. Tailor-made solvents for pharmaceutical use? Experimental and computational approach for determining solubility in deep eutectic solvents (DES). *International Journal of Pharmaceutics: X*, 1:100034, 2019. 50

[138] Shahram Emami and Ali Shayanfar. Deep eutectic solvents for pharmaceutical formulation and drug delivery applications. *Pharmaceutical Development and Technology*, 25(7):779–796, 2020. 50

[139] Ivo M Aroso, João C Silva, Francisca Mano, Ana S D Ferreira, Madalena Dionísio, Isabel Sá-Nogueira, Susana Barreiros, Rui L Reis, Alexandre Paiva, and Ana Rita C Duarte. Dissolution enhancement of active pharmaceutical ingredients by therapeutic deep eutectic systems. *European Journal of Pharmaceutics and Biopharmaceutics*, 98:57–66, 2016. 50, 70

[140] Emad Ali, Mohamed K Hadj-Kali, Sarwono Mulyono, and Inas Alnashef. Analysis of operating conditions for CO2 capturing process using deep eutectic solvents. *International Journal of Greenhouse Gas Control*, 47:342–350, 2016. 50

[141] Fei Luo, Xinglong Liu, Shuo Chen, Yunfei Song, Xiaoyan Yi, Changyong Xue, Lanyi Sun, and Jun Li. Comprehensive Evaluation of a Deep Eutectic Solvent Based CO2

Capture Process through Experiment and Simulation. *ACS Sustainable Chemistry and Engineering*, 9(30):10250–10265, 2021. 50

[142] Changkun Zhang, Yu Ding, Leyuan Zhang, Xuelan Wang, Yu Zhao, Xiaohong Zhang, and Guihua Yu. A Sustainable Redox-Flow Battery with an Aluminum-Based, Deep-Eutectic-Solvent Anolyte. *Angewandte Chemie*, 129(26):7562–7567, 2017. 50, 70

[143] C Florindo, F S Oliveira, L P N Rebelo, Ana M Fernandes, and I M Marrucho. Insights into the synthesis and properties of deep eutectic solvents based on cholinium chloride and carboxylic acids. *ACS Sustainable Chemistry and Engineering*, 2(10):2416–2425, 2014. 50

[144] Andrew P Abbott, David Boothby, Glen Capper, David L Davies, and Raymond K Rasheed. Deep Eutectic Solvents formed between choline chloride and carboxylic acids: Versatile alternatives to ionic liquids. *Journal of the American Chemical Society*, 126(29):9142–9147, 2004. 50, 70

[145] Burcu Gurkan, Henry Squire, and Emily Pentzer. Metal-Free Deep Eutectic Solvents: Preparation, Physical Properties, and Significance. *Journal of Physical Chemistry Letters*, 10(24):7956–7964, 2019. 50, 52, 73

[146] Zhen Song, Xutao Hu, Hongyi Wu, Mingcan Mei, Steffen Linke, Teng Zhou, Zhiwen Qi, and Kai Sundmacher. Systematic Screening of Deep Eutectic Solvents as Sustainable Separation Media Exemplified by the CO2Capture Process. *ACS Sustainable Chemistry and Engineering*, 8(23):8741–8751, 2020. 51

[147] Vahideh Alizadeh, Friedrich Malberg, Agílio A H Pádua, and Barbara Kirchner. Are There Magic Compositions in Deep Eutectic Solvents? Effects of Composition and Water Content in Choline Chloride/Ethylene Glycol from Ab Initio Molecular Dynamics. *Journal of Physical Chemistry B*, 124(34):7433–7443, 2020. 51

[148] A P Abbott, G Capper, B G Swain, and D A Wheeler. Electropolishing of stainless steel in an ionic liquid. *Transactions of the Institute of Metal Finishing*, 83(1):51–53, 2005. 51, 67

[149] Rusul Khaleel Ibrahim, Maan Hayyan, Mohammed Abdulhakim AlSaadi, Shaliza Ibrahim, Adeeb Hayyan, and Mohd Ali Hashim. Physical properties of ethylene glycol-based deep eutectic solvents. *Journal of Molecular Liquids*, 276:794–800, 2019. 51

[150] Gregorio García, Santiago Aparicio, Ruh Ullah, and Mert Atilhan. Deep eutectic solvents: Physicochemical properties and gas separation applications. *Energy and Fuels*, 29(4):2616–2644, 2015. 51, 70

[151] Vira Agieienko and Richard Buchner. Is ethaline a deep eutectic solvent? *Physical Chemistry Chemical Physics*, 24(9):5265–5268, 2022. 51, 65

[152] Stephanie Spittle, Derrick Poe, Brian Doherty, Charles Kolodziej, Luke Heroux, Md Ashraful Haque, Henry Squire, Tyler Cosby, Yong Zhang, Carla Fraenza, Sahana Bhattacharyya, Madhusudan Tyagi, Jing Peng, Ramez A Elgammal, Thomas Zawodzinski, Mark Tuckerman, Steve Greenbaum, Burcu Gurkan, Mark Dadmun, Edward J Maginn, and Joshua Sangoro. Evolution of microscopic heterogeneity and dynamics in choline chloride-based deep eutectic solvents. *Nature Communications*, 13(1), 2022. 53, 60, 67

[153] William F. Smith and Javad Hashemi. *Foundation of Materials Science and Engineering*. McGraw-Hill, 4th edition, 2006. 54

[154] Xiangqian Meng, Karine Ballerat-Busserolles, Pascale Husson, and Jean Michel Andanson. Impact of water on the melting temperature of urea + choline chloride deep eutectic solvent. *New Journal of Chemistry*, 40(5):4492–4499, 2016. 54

[155] Lina Yuan, Simon Clevers, Nicolas Couvrat, Yohann Cartigny, Valérie Dupray, and Gérard Coquerel. Precise Urea/Water Eutectic Composition by Temperature-Resolved

Second Harmonic Generation. *Chemical Engineering and Technology*, 39(7):1326–1332, 2016. 54

[156] Donald R. Askeland and Wendelin J. Wright. *Essentials of Materials Science and Engineering*. Cengage Learning, 4th edition, 2018. 57

[157] Philip J Reid and Paul F Barbara. Dynamic solvent effect on betaine-30 electron-transfer kinetics in alcohols. *Journal of Physical Chemistry*, 99(11):3554–3565, 1995. 57

[158] S.R. Mente and M. Maroncelli. Computer simulations of the solvatochromism of betaine-30. *Journal of Physical Chemistry B*, 103(36):7704–7719, 1999. 57

[159] Ibrahim Alfurayj, Carla Cecilia Fraenza, Yong Zhang, Rathiesh Pandian, Stephanie Spittle, Bryce Hansen, William Dean, Burcu Gurkan, Robert Savinell, Steve Greenbaum, Edward Maginn, Joshua Sangoro, and Clemens Burda. Solvation Dynamics of Wet Ethaline: Water is the Magic Component. *Journal of Physical Chemistry B*, 125(31):8888–8901, 2021. 57

[160] Nancy E Levinger, Alan E Johnson, Gilbert C Walker, and Paul F Barbara. Specific excitation of the solvent coordinate in the S3→S1 and S1→S0 radiationless decay of the betaines. *Chemical Physics Letters*, 196(1-2):159–165, 1992. 60

[161] Hyojoon Kim, Hyonseok Hwang, and Peter J Rossky. Quantum simulation of solution phase intramolecular electron transfer rates in betaine-30. *Journal of Physical Chemistry A*, 110(39):11223–11229, 2006. 60

[162] M L Horng, J A Gardecki, A Papazyan, and M Maroncelli. Subpicosecond measurements of polar solvation dynamics: Coumarin 153 revisited. *Journal of Physical Chemistry*, 99(48):17311–17337, 1995. 60

[163] Philip J Griffin, Tyler Cosby, Adam P Holt, Roberto S Benson, and Joshua R Sangoro. Charge transport and structural dynamics in carboxylic-acid-based deep eutectic mixtures. *Journal of Physical Chemistry B*, 118(31):9378–9385, 2014. 60, 71

[164] Emanuel A Crespo, Liliana P Silva, Joel O Lloret, Pedro J Carvalho, Lourdes F Vega, Fèlix Llovell, and João A P Coutinho. A methodology to parameterize SAFT-type equations of state for solid precursors of deep eutectic solvents: The example of cholinium chloride. *Physical Chemistry Chemical Physics*, 21(27):15046–15061, 2019. 65

[165] Chiara Liliana Boldrini, Norberto Manfredi, Filippo Maria Perna, Vanira Trifiletti, Vito Capriati, and Alessandro Abbotto. Dye-Sensitized Solar Cells that use an Aqueous Choline Chloride-Based Deep Eutectic Solvent as Effective Electrolyte Solution. *Energy Technology*, 5(2):345–353, 2 2017. 70

[166] L Bahadori, M A Hashim, N S A Manan, F S Mjalli, I M AlNashef, N P Brandon, and M H Chakrabarti. Investigation of Ammonium- and Phosphonium-Based Deep Eutectic Solvents as Electrolytes for a Non-Aqueous All-Vanadium Redox Cell. *Journal of The Electrochemical Society*, 163(5):A632–A638, 2016. 70

[167] Shahriar Mufid Rahman, Suhana Binti Mohd Said, Balamurugan Subramanian, Bui Duc Long, Mukhtar A Kareem, and Norhayati Soin. Synthesis and Characterization of Polymer Electrolyte Using Deep Eutectic Solvents and Electrospun Poly(vinyl alcohol) Membrane. *Industrial and Engineering Chemistry Research*, 55(30):8341–8348, 2016. 70

[168] Daniel Carriazo, María C Gutiérrez, Fernando Picó, José M Rojo, José L G Fierro, M Luisa Ferrer, and Francisco Del Monte. Phosphate-functionalized carbon monoliths from deep eutectic solvents and their use as monolithic electrodes in supercapacitors. *ChemSusChem*, 5(8):1405–1409, 2012. 70

[169] Rosanna Toniolo, Nicolò Dossi, Rossella Svigelj, Laura Pigani, Fabio Terzi, Ornella Abollino, and Gino Bontempelli. A Deep Eutectic Solvent-based Amperometric Sensor for the Detection of Low Oxygen Contents in Gaseous Atmospheres. *Electroanalysis*, 28(4):757–763, 2016. 70

[170] M.H. Zainal-Abidin, M. Hayyan, A. Hayyan, and N.S. Jayakumar. New horizons in the extraction of bioactive compounds using deep eutectic solvents: A review. *Analytica Chimica Acta*, 979, 2017. 70

[171] Josué D Mota-Morales, Regina J Sánchez-Leija, Arturo Carranza, John A Pojman, Francisco del Monte, and Gabriel Luna-Bárcenas. Free-radical polymerizations of and in deep eutectic solvents: Green synthesis of functional materials. *Progress in Polymer Science*, 78:139–153, 2017. 70

[172] Luciana I N Tomé, Vanessa Baião, Wanderson da Silva, and Christopher M A Brett. Deep eutectic solvents for the production and application of new materials. *Applied Materials Today*, 10:30–50, 2018. 70

[173] Qingbo Li, Jingyun Jiang, Guofeng Li, Wancheng Zhao, Xinhui Zhao, and Tiancheng Mu. The electrochemical stability of ionic liquids and deep eutectic solvents. *Science China Chemistry*, 59(5):571–577, 2016. 70

[174] Tyler Cosby, Zachariah Vicars, Maximilian Heres, and Joshua Sangoro. Associating Imidazoles: Elucidating the Correlation between the Static Dielectric Permittivity and Proton Conductivity. *Physical Review Letters*, 120(13):136001, 2018. 71

[175] Tyler Cosby, Adam Holt, Philip J Griffin, Yangyang Wang, and Joshua Sangoro. Proton Transport in Imidazoles: Unraveling the Role of Supramolecular Structure. *Journal of Physical Chemistry Letters*, 6(19):3961–3965, 2015. 71

[176] Navin Subba, Ejaj Tarif, Pratik Sen, and Ranjit Biswas. Subpicosecond Solvation Response and Partial Viscosity Decoupling of Solute Diffusion in Ionic Acetamide Deep Eutectic Solvents: Fluorescence Up-Conversion and Fluorescence Correlation Spectroscopic Measurements. *Journal of Physical Chemistry B*, 124(10):1995–2005, 2020. 71

[177] Durgesh V Wagle, Gary A Baker, and Eugene Mamontov. Differential Microscopic Mobility of Components within a Deep Eutectic Solvent. *J. Phys. Chem. Lett*, 6, 2015. 71, 112

[178] Paul T. Callaghan. *Translational Dynamics and Magnetic Resonance: Principles of Pulsed Gradient Spin Echo NMR*. Oxford University Press, 2011. 73

[179] Steve Plimpton. Fast Parallel Algorithms for Short-Range Molecular Dynamics, 1995. 73

[180] Junmei Wang, Romain M Wolf, James W Caldwell, Peter A Kollman, and David A Case. Development and testing of a general Amber force field. *Journal of Computational Chemistry*, 25(9):1157–1174, 2004. 74

[181] M. J. Frisch, G. W. Trucks, H. B. Schlegel, G. E. Scuseria, M. A. Robb, J. R. Cheeseman, G. Scalmani, V. Barone, B. Mennucci, G. A. Petersson, H. Nakatsuji, M. Caricato, X. Li, H. P. Hratchian, A. F. Izmaylov, J. Bloino, G. Zheng, J. L. Sonnenberg, M. Hada, M. Ehara, K. Toyota, R. Fukuda, J. Hasegawa, M. Ishida, T. Nakajima, Y. Honda, O. Kitao, H. Nakai, T. Vreven, J. A. Montgomery, Jr., J. E. Peralta, F. Ogliaro, M. Bearpark, J. J. Heyd, E. Brothers, K. N. Kudin, V. N. Staroverov, R. Kobayashi, J. Normand, K. Raghavachari, A. Rendell, J. C. Burant, S. S. Iyengar, J. Tomasi, M. Cossi, N. Rega, J. M. Millam, M. Klene, J. E. Knox, J. B. Cross, V. Bakken, C. Adamo, J. Jaramillo, R. Gomperts, R. E. Stratmann, O. Yazyev, A. J. Austin, R. Cammi, C. Pomelli, J. W. Ochterski, R. L. Martin, K. Morokuma, V. G. Zakrzewski, G. A. Voth, P. Salvador, J. J. Dannenberg, S. Dapprich, A. D. Daniels, Ö. Farkas, J. B. Foresman, J. V. Ortiz, J. Cioslowski, and D. J. Fox. Gaussian 09 Revision A.1. Gaussian Inc. Wallingford CT 2009. 74

[182] Sasha L Perkins, Paul Painter, and Coray M Colina. Experimental and Computational Studies of Choline Chloride-Based Deep Eutectic Solvents. *Journal of Chemical* {*&*} *Engineering Data*, 59(11):3652–3662, 2014. 74, 87

[183] José Mario Martínez and Leandro Martínez. Packing optimization for automated generation of complex system's initial configurations for molecular dynamics and docking. *Journal of Computational Chemistry*, 24(7):819–825, 2003. 74

[184] L. Martínez, R. Andrade, E. G. Birgin, and J. M. Martínez. PACKMOL: A package for building initial configurations for molecular dynamics simulations. *Journal of Computational Chemistry*, 30(13):2157–2164, oct 2009. 74, 79

[185] Yong Zhang, Akihito Otani, and Edward J. Maginn. Reliable Viscosity Calculation from Equilibrium Molecular Dynamics Simulations: A Time Decomposition Method. *Journal of Chemical Theory and Computation*, 11(8):3537–3546, 2015. 76

[186] Michael T. Humbert, Yong Zhang, and Edward J. Maginn. PyLAT: Python LAMMPS Analysis Tools. *Journal of Chemical Information and Modeling*, 2019. 76

[187] Martin Brehm and Barbara Kirchner. Travis - a free analyzer and visualizer for monte carlo and molecular dynamics trajectories. *Journal of Chemical Information and Modeling*, 51:2007–2023, 7 2011. 76, 80

[188] Rudolf Gorenflo, Joulia Loutchko, and Yuri Luchko. Computation of the mittag-leffler function $e_{\alpha,\beta}(z)$ and its derivative. *Fract. Calc. Appl. Anal*, 5:491–518, 2002. 78

[189] A. K. Shukla and J. C. Prajapati. On a generalization of Mittag-Leffler function and its properties. *Journal of Mathematical Analysis and Applications*, 336(2):797–811, 2007. 78

[190] Varley F. Sears. Neutron scattering lengths and cross sections. *Neutron News*, 3:26–37, 1992. 78

[191] Mark E. Tuckerman, D.A. Yarne, Shane O. Samuelson, Adam L. Hughes, and Glenn J. Martyna. Exploiting multiple levels of parallelism in molecular dynamics based calculations via modern techniques and software paradigms on distributed memory computers. *Computer Physics Communications*, 128:333–376, 6 2000. 79

[192] Brian Doherty and Orlando Acevedo. Opls force field for choline chloride-based deep eutectic solvents. *Journal of Physical Chemistry B*, 122:9982–9993, 8 2018. 79

[193] K. Shahbaz, S. Baroutian, F.S. Mjalli, M.A. Hashim, and I.M. AlNashef. Densities of ammonium and phosphonium based deep eutectic solvents: Prediction using artificial intelligence and group contribution techniques. *Thermochimica Acta*, 527:59–66, 1 2012. 79

[194] Nathan Luehr, Thomas E Markland, and Todd J Martínez. Multiple time step integrators in ab initio molecular dynamics. *The Journal of Chemical Physics*, 140(8):84116, 2014. 79

[195] Mark E Tuckerman and Michele Parrinello. Integrating the Car–Parrinello equations. II. Multiple time scale techniques. *The Journal of Chemical Physics*, 101(2):1316–1329, 1994. 79

[196] M Tuckerman, B J Berne, and G J Martyna. Reversible multiple time scale molecular dynamics. *The Journal of Chemical Physics*, 97(3):1990–2001, aug 1992. 79

[197] G Seifert, D Porezag, and Th. Frauenheim. Calculations of molecules, clusters, and solids with a simplified LCAO-DFT-LDA scheme. *International Journal of Quantum Chemistry*, 58(2):185–192, 1996. 79

[198] D Porezag, Th Frauenheim, Th Köhler, G Seifert, and R Kaschner. Construction of tight-binding-like potentials on the basis of density-functional theory: Application to carbon. *Physical Review B*, 51(19):12947–12957, 1995. 79

[199] P Hohenberg and W Kohn. Inhomogeneous Electron Gas. *Physical Review*, 136(3B):B864–B871, 1964. 79

[200] Zhuoran Long, Austin O Atsango, Joseph A Napoli, Thomas E Markland, and Mark E Tuckerman. Elucidating the Proton Transport Pathways in Liquid Imidazole with First-Principles Molecular Dynamics. *The Journal of Physical Chemistry Letters*, 11(15):6156–6163, 2020. 79

[201] Joost VandeVondele, Matthias Krack, Fawzi Mohamed, Michele Parrinello, Thomas Chassaing, and Jürg Hutter. Quickstep: Fast and accurate density functional calculations using a mixed gaussian and plane waves approach. *Computer Physics Communications*, 167:103–128, 4 2005. 79

[202] Joost VandeVondele and Jürg Hutter. Gaussian basis sets for accurate calculations on molecular systems in gas and condensed phases. *Journal of Chemical Physics*, 127:114105, 2007. 79

[203] John P Perdew, Kieron Burke, and Matthias Ernzerhof. Generalized gradient approximation made simple. *Physical Review Letters*, 77:3865–3868, 10 1996. 79

[204] Stefan Grimme, Stephan Ehrlich, and Lars Goerigk. Effect of the damping function in dispersion corrected density functional theory. *Journal of Computational Chemistry*, 32:1456–1465, 2011. 79

[205] Maximilian Kubillus, Tomáš Kubař, Michael Gaus, Jan Řezáč, and Marcus Elstner. Parameterization of the DFTB3 Method for Br, Ca, Cl, F, I, K, and Na in Organic and Biological Systems. *Journal of Chemical Theory and Computation*, 11(1):332–342, jan 2015. 80

[206] Michael Gaus, Albrecht Goez, and Marcus Elstner. Parametrization and Benchmark of DFTB3 for Organic Molecules. *Journal of Chemical Theory and Computation*, 9(1):338–354, jan 2013. 80

[207] Glenn J Martyna, Michael L Klein, and Mark Tuckerman. Nosé–hoover chains: The canonical ensemble via continuous dynamics. *Journal of Chemical Physics*, 97:2635–2643, 1992. 80

[208] Shuichi Nosé. A unified formulation of the constant temperature molecular dynamics methods. *Journal of Chemical Physics*, 81:511–519, 1984. 80

[209] M. T. McDonnell, D. P. Olds, K. L. Page, J. C. Neufeind, M. G. Tucker, J. C. Bilheux, W. Zhou, and P. F. Peterson. ADDIE: ADvanced DIffraction Environment – a software

environment for analyzing neutron diffraction data. *Acta Crystallographica Section A*, 73(a1):a377, May 2017. 80

[210] A Meyer, R M Dimeo, P M Gehring, and D A Neumann. The high-flux backscattering spectrometer at the NIST Center for Neutron Research. *Review of Scientific Instruments*, 74(5):2759–2777, 2003. 80

[211] Richard Tumanjong Azuah, Larry R Kneller, Yiming Qiu, Philip L W Tregenna-Piggott, Craig M Brown, John R D Copley, and Robert M Dimeo. DAVE: A comprehensive software suite for the reduction, visualization, and analysis of low energy neutron spectroscopic data. *Journal of Research of the National Institute of Standards and Technology*, 114(6):341–358, 2009. 81

[212] Pallavi Singh and Siddharth Pandey. Solute–solvent interactions within aqueous poly(ethylene glycol): Solvatochromic probes for empirical determination and preferential solvation. *Green Chemistry*, 9(3):254–261, 2007. 82

[213] Ying Guang Wu, Masaaki Tabata, and Toshiyuki Takamuku. Preferential solvation in aqueous-organic mixed solvents using solvatochromic indicators. *Journal of Solution Chemistry*, 31(5):381–395, 2002. 82

[214] Narayan Ray, Ramkrishna Pramanik, Parimal Kumar Das, and Sanjib Bagchi. UV visible spectroscopic study of solvation of 2,6-diphenyl-4(2,4,6-triphenyl-1-pyridino)phenolate in ternary solvent mixtures. Technical Report 3-4, 2001. 82

[215] Tejwant Singh and Arvind Kumar. Aggregation behavior of ionic liquids in aqueous solutions: Effect of alkyl chain length, cations, and anions. *Journal of Physical Chemistry B*, 111(27):7843–7851, 2007. 84

[216] Carmine D'Agostino, Mick D Mantle, Claire L Mullan, Christopher Hardacre, and Lynn F Gladden. Diffusion, Ion Pairing and Aggregation in 1-Ethyl-3-Methylimidazolium-Based Ionic Liquids Studied by 1H and 19F PFG NMR: Effect

of Temperature, Anion and Glucose Dissolution. *ChemPhysChem*, 19(9):1081–1088, 2018. 84

[217] Alexander Korotkevich, Dzmitry S. Firaha, Agilio A.H. Padua, and Barbara Kirchner. Ab initio molecular dynamics simulations of SO2 solvation in choline chloride/glycerol deep eutectic solvent. *Fluid Phase Equilibria*, 448:59–68, 2017. 87

[218] Gregorio García, Mert Atilhan, and Santiago Aparicio. The impact of charges in force field parameterization for molecular dynamics simulations of deep eutectic solvents. *Journal of Molecular Liquids*, 211:506–514, 11 2015. 87

[219] Juan C Araque, Jeevapani J Hettige, and Claudio J Margulis. Modern Room Temperature Ionic Liquids, a Simple Guide to Understanding Their Structure and How It May Relate to Dynamics. *Journal of Physical Chemistry B*, 119(40):12727–12740, 2015. 95

[220] Hemant K Kashyap, Jeevapani J Hettige, Harsha V R Annapureddy, and Claudio J Margulis. SAXS anti-peaks reveal the length-scales of dual positive–negative and polar–apolar ordering in room-temperature ionic liquids. *Chemical Communications*, 48(42):5103–5105, 2012. 95

[221] M H Jensen, C Gainaru, C Alba-Simionesco, T Hecksher, and K Niss. Slow rheological mode in glycerol and glycerol-water mixtures. *Physical Chemistry Chemical Physics*, 20(3):1716–1723, 2018. 103, 119

[222] Adam H Turner and John D Holbrey. Investigation of glycerol hydrogen-bonding networks in choline chloride/glycerol eutectic-forming liquids using neutron diffraction. *Physical Chemistry Chemical Physics*, 21(39):21782–21789, 2019. 106

[223] Sascha Gehrke, Michael Von Domaros, Ryan Clark, Oldamur Hollóczki, Martin Brehm, Tom Welton, Alenka Luzar, and Barbara Kirchner. Structure and lifetimes in ionic liquids and their mixtures. *Faraday Discussions*, 206:219–245, 2018. 115

[224] David R. Lide. *CRC handbook of chemistry and physics, Internet Version 2005, http://www.hbcpnetbase.com.* CRC Press, Boca Raton, FL, 2005. 115

Vita

Stephanie is originally from Denver, North Carolina. She graduated from Appalachian State University with a B.S. in Chemistry and a minor in Mathematics in 2017. Her undergraduate research project under Dr. Michael Hambourger focused on exploring metal-crosslinked polydimethylsiloxane networks as recyclable, environmentally friendly rubber materials. In fall of 2017, she moved to Knoxville, Tennessee to begin her PhD at University of Tennessee (UT). While at UT, she was a Tennessee Fellow for Graduate Excellence, which is a 4-year fellowship. After graduating, she plans to pursue a career in industry studying sustainable energy storage technologies.